

LAPPEENRANTA UNIVERSITY OF TECHNOLOGY
Faculty of Technology
Degree Programme in Energy Technology

Jonna Tiainen

MODELING OF LIQUID-SOLID FLOW IN INDUSTRIAL SCALE

Examiners: Docent Teemu Turunen-Saaresti, D.Sc. (Tech.)
Docent Keijo Jaanu, D.Sc. (Tech.)

TIIVISTELMÄ

Lappeenrannan teknillinen yliopisto
Teknillinen tiedekunta
Energiatekniikan koulutusohjelma

Jonna Tiainen

Neste-kiintoainevirtauksen mallinnus teollisuusmittakaavassa

Diplomityö

2014

129 sivua, 49 kuvaa, 18 taulukkoa ja 1 liite

Tarkastajat: Dosentti Teemu Turunen-Saaresti, TkT
Dosentti Keijo Jaanu, TkT

Hakusanat: kaksifaasivirtaus, neste-kiintoainevirtaus, laskennallinen virtausmekaniikka

Tässä työssä käytetään kaupallista laskennallisen virtausmekaniikan (CFD) ohjelmaa ANSYS Fluent 14.5 neste-kiintoainevirtauksen mallintamiseen teollisuusmittakaavassa. Kirjallisuudessa on muutamia tutkimuksia neste-kiintoainevirtauksesta teollisuusmittakaavassa, mutta tietoa kyseessä olevasta tapauksesta modifioidulla geometrialla ei löydy. Tämän diplomityön tavoitteena on kuvata monifaasimallien vahvuudet ja heikkoudet, kun tarkastellaan suuren mittakaavan sovellusta neste-kiintoainevirtauksen yhteydessä, sisältäen rajakerrostarkastelun.

Tulokset osoittavat, että tarkoituksenmukaisimman monifaasimallin valintaan vaikuttaa virtausalue. Siksi ennen mallintamista suositellaan virtausalueen huolellista arvioimista. Työn aikana on tähän tarkoitukseen kehitetty laskentatyökalu. Homogeeninen monifaasimalli pätee vain homogeeniselle suspensiolle, erillisten faasien mallia (DPM) suositellaan homogeeniselle ja heterogeeniselle virtaukselle, joissa putken Froude luku on suurempi kuin 1.0, kun taas seos ja Eulerian -malleilla voidaan ennustaa myös virtauksia, joissa putken Froude luku on pienempi kuin 1.0 ja partikkelit sedimentoituvat. Tiheyssuhteen kasvaessa ja putken Froude luvun pienentyessä Eulerian -malli antaa tarkimmat tulokset, koska se ei sisällä yksinkertaisuuksia Navier–Stokes -yhtälöissä, kuten muut mallit.

Laskentatulokset osoittavat lisäksi putkessa potentiaalisen eroosioalueen sijainnin, joka on riippuvainen muun muassa tiheyssuhteesta. Mahdollisesti sedimentoituneet partikkelit voivat aiheuttaa eroosiota sekä lisätä painehäviötä. Putkimutkassa eroosioalueen sijaintiin vaikuttavat erityisesti päävirtausta kohtisuoraan olevat sekundaarivirtaukset.

ABSTRACT

Lappeenranta University of Technology
Faculty of Technology
Degree Programme in Energy Technology

Jonna Tiainen

Modeling of Liquid-Solid Flow in Industrial Scale

Master's thesis

2014

129 pages, 49 figures, 18 tables, and 1 appendix

Examiners: Docent Teemu Turunen-Saaresti, D.Sc. (Tech.)
Docent Keijo Jaanu, D.Sc. (Tech.)

Keywords: two-phase flow, liquid-solid flow, computational fluid dynamics

In the present work, liquid-solid flow in industrial scale is modeled using the commercial software of Computational Fluid Dynamics (CFD) ANSYS Fluent 14.5. In literature, there are few studies on liquid-solid flow in industrial scale, but any information about the particular case with modified geometry cannot be found. The aim of this thesis is to describe the strengths and weaknesses of the multiphase models, when a large-scale application is studied within liquid-solid flow, including the boundary-layer characteristics.

The results indicate that the selection of the most appropriate multiphase model depends on the flow regime. Thus, careful estimations of the flow regime are recommended to be done before modeling. The computational tool is developed for this purpose during this thesis. The homogeneous multiphase model is valid only for homogeneous suspension, the discrete phase model (DPM) is recommended for homogeneous and heterogeneous suspension where pipe Froude number is greater than 1.0, while the mixture and Eulerian models are able to predict also flow regimes, where pipe Froude number is smaller than 1.0 and particles tend to settle. With increasing material density ratio and decreasing pipe Froude number, the Eulerian model gives the most accurate results, because it does not include simplifications in Navier–Stokes equations like the other models.

In addition, the results indicate that the potential location of erosion in the pipe depends on material density ratio. Possible sedimentation of particles can cause erosion and increase pressure drop as well. In the pipe bend, especially secondary flows, perpendicular to the main flow, affect the location of erosion.

АННОТАЦИЯ

Лаппеенрантский технологический университет
Технологический факультет
Программа по соисканию степени в области энергетических технологий

Йонна Тиайнен

Моделирование потока жидкости и твердых частиц в промышленных масштабах

Работа на соискание степени магистра

2014

129 страниц, 49 рисунков и чертежей, 18 таблиц и 1 приложение

Экзаменующие: Доцент Теэму Турунен-Саарести, д.т.н.
Доцент Кеййо Яану, д.т.н.

Ключевые слова: двухфазный поток, поток жидкости и твердых частиц, вычислительная гидродинамика

В данной работе поток жидкости и твердых частиц в промышленных масштабах моделируется коммерческим программным обеспечением по вычислительной гидродинамике (ВГД) ANSYS Fluent 14.5. В литературе представлены некоторые исследования потока жидкости и твердых частиц в промышленных масштабах, но никакой информации нельзя найти о частном случае потока с модифицированной геометрией. Целью данной работы является описать сильные и слабые стороны многофазных моделей, когда исследуется крупномасштабное применение геометрии в потоке, включая характеристики пограничного слоя.

Результаты показывают, что выбор наиболее подходящей многофазной модели зависит от режима потока. Таким образом, перед моделированием рекомендуется выполнить тщательные оценки режима потока. Для этой цели во время выполнения данной работы разработан вычислительный инструментарий. Гомогенная многофазная модель действует только для гомогенной суспензии, модель дискретных фаз (DPM) рекомендуется для гомогенной и гетерогенной суспензии, где число труб Фруда больше, чем 1.0, а модели смешения и Эйлера могут также предсказывать режимы потока, где число труб Фруда меньше, чем 1.0 и частицы имеют тенденцию оседать. С увеличением отношения плотности материала и уменьшением числа труб Фруда, модель Эйлера дает самые точные результаты, потому что она не содержит упрощения в уравнениях Навье—Стокса подобно другим моделям.

Кроме того, результаты показывают, что возможные места возникновения эрозии в трубе зависят от отношения плотности материала. Возможная седиментация частиц может вызывать эрозию и также увеличивать перепад давления. В колене трубы, особенно вторичные потоки, перпендикулярные к основному потоку, влияют на место образования эрозии.

ACKNOWLEDGEMENTS

I would like to express my sincerest gratitude to Docent Teemu Turunen-Saaresti and Docent Keijo Jaanu for their supervision and guidance during this project. I am particularly grateful to Docent Keijo Jaanu for pushing me patiently forward. It has been a great pleasure learning from him.

I would like to thank Fennotecon Oy for giving me the opportunity to participate in this challenging project and for financing it. I hope that this thesis will be valuable in the future.

My special thanks are given to the staff of the Laboratory of Fluid Dynamics at Lappeenranta University of Technology for offering me all that knowledge during my studies and employments. That knowledge has been very valuable during this project.

I would also like to acknowledge the support provided by my family and friends during my studies.

Finally, I wish to thank Aleksi for his loving support.

Jyväskylä, February 15, 2014

Jonna Tiainen

TABLE OF CONTENTS

1	INTRODUCTION	12
2	MULTIPHASE FLOWS	15
2.1	Volume Fraction	18
2.2	Density	18
2.3	Concentration and Loading	19
2.4	Conservation Equations	19
3	APPROACHES FOR THE NUMERICAL SIMULATION	20
3.1	Eulerian-Lagrangian Approach	21
3.2	Eulerian-Eulerian Approach	23
3.2.1	Volume of Fluid Model	23
3.2.2	Mixture Model	25
3.2.3	Eulerian Model	26
3.3	Turbulence Models	29
3.3.1	Two-Equation Models	30
3.3.2	Reynolds Stress Model	35
3.3.3	Direct Numerical Simulation	35
3.3.4	Large Eddy Simulation	36
3.3.5	Near Wall Treatment	36
4	PHASE INTERACTION	39
4.1	Dimensionless Groups	40
4.2	Drag Force	43
4.3	Buoyancy Force	44
4.4	Lift Force	45
4.5	Virtual Mass and Basset Forces	45
4.6	Body Force	46
4.7	Wall Lift Force	46
4.8	Turbulence Modulation	47
4.9	Turbulent Dispersion Force	49
4.10	Surface Tension Force	51
5	TWO-PHASE FLOW SIMULATION METHODS	51
5.1	Details of the Studied Mixing Tank	52
5.1.1	Estimation of the Pipe Entrance Lengths	52
5.1.2	Modified Shape of the Mixing Tank	54
5.2	Computational Mesh	55
5.2.1	How to Create High Quality Mesh in Complex Industrial Scale Geometry?	55
5.2.2	Numerical Uncertainty	59
5.2.3	Mesh Independence Test	61
5.3	Selected Boundary Conditions and Initial Values	62
5.3.1	Boundary Conditions in the Eulerian-Lagrangian Approach	64
5.3.2	Typical Values for Particle Density and Concentration in Wastewater Treatment Process	65

5.4	Ways to Couple Pressure and Velocity in Two-Phase Flows	67
5.5	Convergence Criteria	68
5.6	Computational Time	68
6	RESULTS AND DISCUSSION	71
6.1	Difference Between Turbulence Models	72
6.1.1	Secondary Flows	72
6.1.2	Boundary Layer Separation	75
6.2	Effect of Boundary Conditions	80
6.3	Effect of Particle Density	82
6.3.1	How Do Secondary Flows Affect Dispersed Phase?	86
6.3.2	How Do Particles Affect Continuous Phase?	89
6.3.3	How Does the Change in Particle Density Affect Erosion?	93
6.4	Effect of Particle Size	93
6.5	Difference Between Multiphase Models	96
6.6	Modeling of Turbulent Dispersion	107
6.7	Pressure Losses in Two-Phase Flow	113
6.8	Development of the Computational Tool	114
7	CONCLUSIONS AND RECOMMENDATIONS	116
	REFERENCES	119
	APPENDICES	

APPENDIX I: Figure 49. The contours of volume fraction in the by-pass pipe.

Nomenclature

Roman symbols

a	acceleration	m/s^2
A	area	m^2
A_0	constant in the realizable $k - \varepsilon$ turbulence model	
B	constant in Eq. (85)	
C	concentration	
$C_{1\varepsilon}$	constant in the $k - \varepsilon$ turbulence model	
$C_{2\varepsilon}$	constant in the $k - \varepsilon$ turbulence model	
C_μ	constant in the $k - \varepsilon$ turbulence model	
d	diameter	m
D_{pq}	fluid-particulate dispersion tensor in Eq. (123)	s
e	error	$\%$
e	restitution coefficient for particle collisions in Eq. (47)	
f	drag function	
f	frequency	Hz
f	friction coefficient	
F	force	N
F_L	Durand factor	
g	gravitational acceleration	m/s^2
g_0	radial distribution function in Eq. (47)	
GCI_{fine}	fine-grid convergence index	
h	representative cell size	m
k	turbulence kinetic energy	m^2/s^2
k_s	surface roughness	m
k_s^+	dimensionless surface roughness	
K_{dc}	interfacial momentum exchange coefficient	
K_{fs}	fluid-solid exchange coefficient	
K_{kj}	solid-solid exchange coefficient	
K_{pq}	fluid-fluid exchange coefficient	
l	length	m
m	mass	kg
n	number density	$1/\text{m}^3$
N	number of computational cells	
p	pressure	Pa
P	perimeter	m
q_m	mass flow rate	kg/s
q_v	volume flow rate	m^3/s
r	mesh refinement factor in Eq. (131)	
r	uniform random number in Eq. (120)	
R_0	curvature ratio	
S	source term	
S_{ij}	mean strain rate tensor	$1/\text{s}$
t	time	s
t_p	particle response time	s
T_L	fluid Lagrangian integral time	s

u	velocity of the continuous phase	m/s
u'	fluctuating velocity	m/s
u_τ	friction velocity	m/s
u^+	dimensionless velocity	
v	velocity of the dispersed phase	m/s
v_{dc}	interfacial velocity	m/s
V	volume	m ³
x	x direction in Cartesian coordinates	
y	y direction in Cartesian coordinates	
y^+	dimensionless normal distance	
z	z direction in Cartesian coordinates	
Z	loading	

Greek symbols

α	constant in the $k - \omega$ turbulence model	
α	volume fraction	%
α_1	constant in Eq. (21)	
α_2	constant in Eq. (21)	
α_3	constant in Eq. (21)	
β	constant in the $k - \omega$ turbulence model	
β	constant in the RNG $k - \varepsilon$ turbulence model	
β^*	constant in the $k - \omega$ turbulence model	
δ	boundary layer thickness	m
δ_{ij}	Kronecker's delta	
ε	turbulence dissipation rate	m ² /s ³
η	dimensionless variable in the RNG $k - \varepsilon$ turbulence model	
η_0	constant in the RNG $k - \varepsilon$ turbulence model	
γ	material density ratio	
κ	von Kármán constant	
λ	bulk viscosity	kg/ms
μ	dynamic viscosity	kg/ms
ν	kinematic viscosity	m ² /s
ω	specific dissipation rate	1/s
ρ	density	kg/m ³
$\bar{\rho}$	bulk density	kg/m ³
σ	constant in the $k - \omega$ turbulence model	
σ	surface tension	kg/m
σ^*	constant in the $k - \omega$ turbulence model	
σ_ε	constant in the $k - \varepsilon$ turbulence model	
σ_k	constant in the $k - \varepsilon$ turbulence model	
σ_{pq}	dispersion Prandtl number in Eq. (123)	s
τ	shear stress	N/m ²
τ_{ij}	viscous stress tensor	N
ζ	Gaussian distributed random number	

Abbreviations

CFD	Computational Fluid Dynamics
CSO	Combined Sewer Overflow tank
DEM	Discrete Element Method
DNS	Direct Numerical Simulation
DPM	Discrete Phase Model
FSM	Fractional Step Method
GCI	Grid Convergence Method
HRN	High Reynolds Number approach
LES	Large Eddy Simulation
LRN	Low Reynolds Number approach
NITA	Non-Iterative Time Advancement scheme
PC-SIMPLE	Phase Coupled SIMPLE
PISO	Pressure Implicit with Splitting of Operators
RAM	Random Access Memory
RANS	Reynolds Averaged Navier-Stokes
RNG	Re-Normalization Group $k - \epsilon$ model
RSM	Reynolds Stress Model
SIMPLE	Semi-Implicit Method for Pressure-Linked Equations
SIMPLEC	SIMPLE-Consistent
SST	Shear-Stress Transport $k - \omega$ model
VOF	Volume of Fluid model

Dimensionless numbers

C_D	drag coefficient
Ca	capillary number
De	Dean number
Fr	Froude number
Re	Reynolds number
Sc	Schmidt number
St	Stokes number
We	Weber number

Superscripts

-	(overbar) average
'	(prime) fluctuating component

Subscripts

a	approximate
B	Basset
c	collision, continuous phase
d	dispersed phase
D	diffusion, drag
ext	extrapolated
f	fluid
fr	frictional
H	hydraulic

I	local instant value
j	fine particles
k	coarse particles, phase index
kin	kinetic
K	Kolmogorov scale
lam	laminar
m	mean, mixture
p	secondary phase, particle
P	pressure
q	primary phase
r	relative
s	settling, solid, system
t	terminal
T	turbulent
V	virtual mass
w	wall

1 INTRODUCTION

Multiphase flows are important in many industrial applications, for example in fluidized beds, food manufacturing, process industry, steam turbines, and wastewater treatment. At a wastewater treatment plant, wastewater undergoes the following processes: preliminary, primary, secondary, and tertiary treatment. In addition, the sludge needs to be treated. The layout of the general wastewater treatment process is shown in Figure 1.

Preliminary treatment includes screening and grit removing [1]. The screens remove large articles from the influent, which could otherwise harm the wastewater pumps [2]. Screens can be coarse, fine or extra fine. Typical aperture sizes for coarse screens are > 6 mm, for fine screens the values range from 1.5 to 6 mm, and for extra fine screens from 0.2 to 1.5 mm [3]. The inert grit is removed by a settlement process, because it cannot be treated in the next stages of treatment. In the settlement process, the lighter organic material remains in suspension while the heavier inert material settles to the bottom of the settling tank [4].

After preliminary treatment, wastewater flows to the primary settling tanks, where the heavier organic material settles to the bottom of the settling tank [2]. In the primary settling tanks, approximately 50–70 % of suspended solids are removed [5]. The settled organic material is called as primary sludge, which is pumped to the sludge handling facilities for sludge treatment [1, 4].

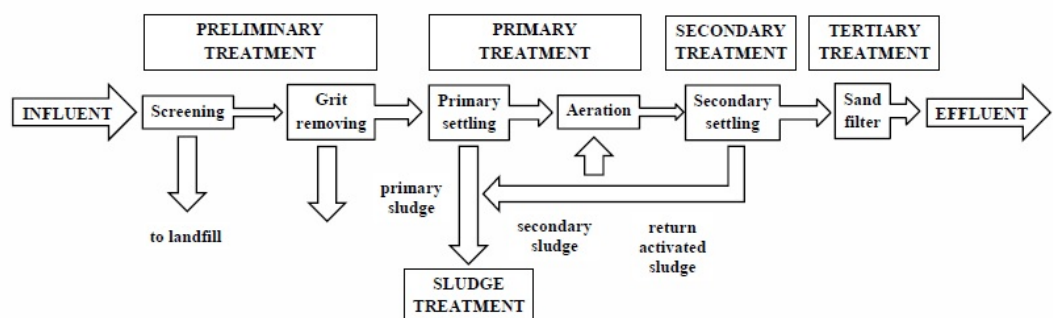


Figure 1. The layout of the general wastewater treatment plant.

Secondary treatment is called as the activated sludge process [4]. Wastewater flows to the aeration tanks, which are aerated by compressors. The new wastewater entering the aeration tank is reseeded with return activated sludge from the secondary settling tank. In the aeration tanks, micro-organisms consume most of the remaining organic material. Micro-organisms grow and settle to the bottom of the secondary settling tank. Some of this secondary sludge is returned back to the aeration tanks and remaining secondary sludge is added to primary sludge for sludge treatment in the sludge handling facilities. [1, 2]

Tertiary treatment is an additional process in the cases, where very high quality of treated wastewater is required. Tertiary treatment includes sand filters, fine filter membranes or ultraviolet light processes. [2]

In this thesis, only one part of the wastewater treatment process is considered. The studied part of the wastewater treatment process is the so-called "mixing tank", where wastewater from the primary settling tanks is mixed with overflow wastewater before the mixture flows to the aeration tanks. Overflow wastewater has passed by the primary settling tanks and thus it has higher concentration of solid suspension than wastewater from the primary settling tanks. Although the application of Computational Fluid Dynamics (CFD) within water treatment has expanded significantly since 1995 [6], in literature there are only few studies on liquid-solid flows in industrial scale. Because any information about this particular case cannot be found, in the present work the large-scale mixing tank is modeled using the commercial software ANSYS Fluent 14.5 and the computational mesh is created using GAMBIT 2.4.6 software. Three multiphase models available in ANSYS Fluent 14.5 software are compared with each other.

Within the modeling of multiphase flows, the problem is not the derivation of the conservation equations, but the closure of the equations [7]. When there is a large number of particles in the dispersed phase, averaging procedures are necessary to make the conservation equations solvable [8, 9]. The most important averaging procedures are the Lagrangian, Eulerian and Boltzmann statistical averaging, when

the multiphase flows are considered [10].

The averaging of the conservation equations introduces more unknowns than the number of equations. Thus, the additional expressions are necessary to close the set of equations. The additional expressions to close the set of equations are referred to as the closure laws. In multiphase modeling, adding the interfacial forces to the momentum equations of each phase requires more closure relations. As a result of complexity of the problem and limited knowledge of the physics in the phase interaction, many empirical correlations are added to the equations of motion [11]. Thus, it is important to know assumptions and limitations of the multiphase models. [8]

This thesis is done for Fennotecon Oy and the targets of the thesis are

- to create high quality mesh in complex industrial scale geometry.
- to study mixing phenomenon and spreading of the solid particles in wastewater treatment process.
- to study the effect of secondary flows on particles, including the boundary-layer characteristics. How is the effect changed when the particle density is varied and what is the influence on erosion?
- to analyze the effect of changes in dispersed phase on flow regime. How does the change in flow regime affect modeling?
- to represent the strengths and weaknesses of different multiphase models.
- to produce unequivocal computational tool, which helps to analyze the problem before CFD modeling, set correct initial values, choose the most suitable multiphase model, and compare the CFD results with theory.

The results represented in this thesis will help to understand difficulties in slurry transport and in modeling two-phase flows, and help to find out ways for efficient mixing.

This thesis is structured as follows. In Chapter 2, the categories of multiphase flows are represented. In Chapter 3, different approaches for the numerical simulation of multiphase flows are studied. Chapter 4 introduces the interfacial surface forces, which take the interaction between phases into account. The studied geometry constructed in GAMBIT 2.4.6 software, and the studied cases simulated with ANSYS Fluent 14.5 software are introduced in Chapter 5. Chapter 6 shows the results of the studied cases. Finally, the conclusions of this thesis are represented in Chapter 7.

2 MULTIPHASE FLOWS

Multiphase flows can be subdivided into three categories, which are dispersed, separated, and transitional flows. In dispersed flows, one phase consists of discrete elements, which are not connected and another phase is continuous. In separated flows, two phases are separated by a line of contact. Transitional flows are combinations of other two categories. The classification of two-phase flows is shown in Figure 2. This thesis considers particulate flow, which belongs to the class of dispersed flows. [8,9]

According to Crowe et al. [9], multiphase flows can also be subdivided into four categories; gas-liquid, gas-solid, liquid-solid and three-phase flows. This thesis considers liquid-solid flows. Liquid-solid flows consist of flows in which solid particles are carried by the liquid. Examples of the liquid-solid flows are slurry flows, hydraulic transport and sediment transport.

The flow regimes of slurries can be referred to as homogeneous suspension, heterogeneous suspension, saltation, moving bed, and stationary bed. Slurry is homogeneous if the variation in the particle concentration from the top to the bottom of the pipe is less than 20 %. Homogeneous slurries normally consist of fine particles which are kept in suspension by the turbulence of the carrier fluid. When the turbulence level is not high enough to maintain homogeneous suspension but is still sufficiently high to prevent any deposition of particles on the bottom of the pipe, the

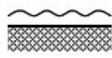
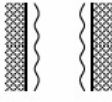
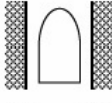
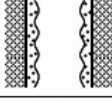
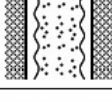
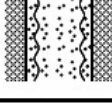
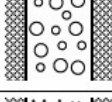
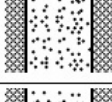
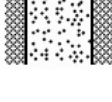
Class	Typical regimes	Geometry	Configuration	Examples
Separated flows	Film flow		Liquid film in gas Gas film in liquid	Film condensation Film boiling
	Annular flow		Liquid core and gas film Gas core and liquid film	Film boiling Boilers
	Jet flow		Liquid jet in gas Gas jet in liquid	Atomization Jet condenser
Mixed or Transitional flows	Cap, Slug or Churn-turbulent flow		Gas pocket in liquid	Sodium boiling in forced convection
	Bubbly annular flow		Gas bubbles in liquid film with gas core	Evaporators with wall nucleation
	Droplet annular flow		Gas core with droplets and liquid film	Steam generator
	Bubbly droplet annular flow		Gas core with droplets and liquid film with gas bubbles	Boiling nuclear reactor channel
Dispersed flows	Bubbly flow		Gas bubbles in liquid	Chemical reactors
	Droplet flow		Liquid droplets in gas	Spray cooling
	Particulate flow		Solid particles in gas or liquid	Transportation of powder

Figure 2. Classification of two-phase flows [10].

flow is heterogeneous. In the saltation regime, particles are settled on the bottom of the pipe and they are being continually picked up by turbulent eddies and dropped to the bottom of the pipe further down the pipeline. [9, 12]

The velocity at which the particles start to settle on the bottom of the pipe is the deposition (or settling) velocity

$$u_s = F_L \sqrt{2gd \left(\frac{\rho_d}{\rho_c} - 1 \right)}, \quad (1)$$

where g is the gravitational acceleration, d is the pipe diameter, and ρ_d and ρ_c are

densities of the dispersed and continuous phases, respectively. The term F_L is the Durand factor, which can be expressed as

$$F_L = \left(1.3\alpha_d^{0.125}\right) \left(1 - e^{-6900d_d}\right), \quad (2)$$

where α_d is the volume fraction of the dispersed phase, and d_d is the particle diameter. [13]

The moving bed regime occurs when the particles settle on the bottom of the pipe and move along as a bed. Finally, when the particles fill the pipe and no further motion is possible define the stationary bed. Then the flow is analogous to the flow through a porous medium. [9, 14]

Bearing in mind that the slurry flow is also dependent on particle density and concentration of the particles, Table 1 represents the characterization of fine and coarse particles and typical flow regime of each particle size.

Table 1. The characterization of fine and coarse particles [13].

	d_d [mm]	
Ultrafine	< 0.01	Gravitational forces are negligible.
Fine	0.01 – 0.1	Usually carried fully suspended, but subject to concentration and gravitational forces.
Medium sized	0.1 – 1	Will move with a deposit at a bottom of the pipe and with concentration gradient.
Coarse	1 – 10	Seldom fully suspended and form deposits on the bottom of the pipe.
Ultracoarse	> 10	Transported as a moving bed on the bottom of the pipe.

According to Doron and Barnea [14], the prediction of the flow regime is very important, because the formation of a stationary bed causes partial blockage of the pipe, increases pressure drop and reduces efficiency. The energy losses can be minimized by avoiding particle settlement, but at the same time flow velocity should be

kept low enough to minimize pressure drop [15]. In the following, important definitions of dispersed phase flows are introduced. The definitions are used to predict flow regime later in this thesis.

2.1 Volume Fraction

The volume fraction of the dispersed phase is defined as

$$\alpha_d = \lim_{\delta V \rightarrow \delta V^o} \frac{\delta V_d}{\delta V}, \quad (3)$$

where δV^o is the limiting volume that ensures a stationary average and δV_d is the volume of the dispersed phase in the volume. The volume fraction of the continuous phase, α_c , is defined equivalently. By definition, the sum of the volume fractions must be unity. [9]

$$\alpha_d + \alpha_c = 1 \quad (4)$$

2.2 Density

The bulk density of the dispersed phase is defined as

$$\bar{\rho}_d = \lim_{\delta V \rightarrow \delta V^o} \frac{\delta m_d}{\delta V}, \quad (5)$$

where δm_d denotes the mass of the dispersed phase. The corresponding definition for the bulk density of the continuous phase is equivalent. The sum of the bulk densities for the dispersed and continuous phases is the mixture density

$$\bar{\rho}_d + \bar{\rho}_c = \rho_m. \quad (6)$$

The bulk density can be related to the volume fraction introduced above and to material (or actual) density. Thus, the bulk density of the dispersed phase can be written as

$$\bar{\rho}_d = \rho_d \alpha_d \quad (7)$$

and the definition for the bulk density of the continuous phase is equivalent. [9]

2.3 Concentration and Loading

According to Crowe et al. [9], the important parameters to the definition of the dispersed phase flows are the dispersed phase mass concentration

$$C = \frac{\bar{\rho}_d}{\bar{\rho}_c} \quad (8)$$

and the ratio of the dispersed phase mass flow rate to the continuous phase mass flow rate, which is referred to as loading

$$Z = \frac{q_{m,d}}{q_{m,c}} = \frac{\bar{\rho}_d v}{\bar{\rho}_c u}, \quad (9)$$

where v and u are the velocities of the dispersed and continuous phases, respectively.

The concentration and material density ratio

$$\gamma = \frac{\rho_d}{\rho_c} \quad (10)$$

can be used to estimate the particle spacing. The distance between particles in the dispersed phase flow can be expressed as

$$\frac{l}{d_d} = \left(\frac{\pi}{6} \frac{1 + \kappa}{\kappa} \right)^{\frac{1}{3}}, \quad (11)$$

where

$$\kappa = \frac{C}{\gamma} = \frac{\alpha_d}{\alpha_c}. \quad (12)$$

If $\frac{l}{d_d} \gg 1$, then the particles can be treated as isolated (the neighboring particles have no influence on the drag). [9]

2.4 Conservation Equations

For a Newtonian incompressible fluid the equation for conservation of mass according to Wilcox [16] is

$$\frac{\partial u_i}{\partial x_i} = 0. \quad (13)$$

The subscript i is a free index, which gets values of 1, 2, and 3. The value of 1 denotes the x direction in Cartesian coordinates, and the values of 2 and 3 denote the y and z directions, respectively. The equation for conservation of momentum is

$$\rho \frac{\partial u_i}{\partial t} + \rho u_j \frac{\partial u_i}{\partial x_j} = -\frac{\partial p}{\partial x_i} + \frac{\partial \tau_{ij}}{\partial x_j}, \quad (14)$$

where τ_{ij} is the viscous stress tensor. The convective term in the momentum equation can be written as

$$u_j \frac{\partial u_i}{\partial x_j} = \frac{\partial}{\partial x_j} (u_i u_j) - u_i \frac{\partial u_j}{\partial x_j} \quad (15)$$

according to the product rule. If we consider the continuity equation, the convective term can be written as

$$u_j \frac{\partial u_i}{\partial x_j} = \frac{\partial}{\partial x_j} (u_i u_j). \quad (16)$$

Now, the Navier-Stokes momentum equation in conservation form is defined as

$$\rho \frac{\partial u_i}{\partial t} + \rho \frac{\partial}{\partial x_j} (u_i u_j) = -\frac{\partial p}{\partial x_i} + \frac{\partial \tau_{ij}}{\partial x_j}, \quad (17)$$

The Navier-Stokes equations in the case of two-phase flow are introduced in the following chapters.

3 APPROACHES FOR THE NUMERICAL SIMULATION

In order to derive the conservation equations for two-phase flow, it is necessary to describe the local characteristics of the flow. From that flow, the macroscopic properties should be obtained by means of an appropriate averaging procedure. By proper averaging, the mean values of the macroscopic properties that effectively eliminate local instant fluctuations, can be obtained. The averaging procedures can be classified into three groups: the Lagrangian averaging, the Eulerian averaging, and the Boltzmann statistical averaging. The Lagrangian averaging is used in the cases where the behavior of an individual particle is more important than the behavior of a group of particles. Both the Eulerian spatial and time averaging are the most

widely used averaging procedures. The Boltzmann statistical averaging approach with a concept of the particle number density is used when the behavior of a large number of particles is studied. [9, 10]

In the following chapters, the approaches to simulate multiphase flow are introduced. In the Eulerian-Lagrangian approach, the trajectory of each particle in the dispersed phase is calculated. In the Eulerian-Eulerian approach, the particles are considered to be a second fluid which behaves like a continuum, and equations are developed for the average properties of the particles.

3.1 Eulerian-Lagrangian Approach

The Eulerian-Lagrangian approach is often referred to as a discrete phase or particle transport model. In the approach, the trajectories of particles are predicted and particles may vary in both size and density [6]. The approach is applicable to both dilute and dense flows [9]. If the flow is steady and dilute a form of the Eulerian-Lagrangian approach is known as the trajectory method like the Discrete Phase Model (DPM) in ANSYS Fluent software. If the flow is unsteady and/or dense, the more general Discrete Element Method (DEM) is required [9].

In the trajectory method, the Navier-Stokes equations are solved for the continuous phase, while the dispersed phase is solved by tracking a large number of particles through the calculated flow field. The trajectory of the particle is obtained by equating particle inertia with the forces acting on the particle:

$$\frac{dv}{dt} = F_D(u - v) + g + F_x, \quad (18)$$

where u is the fluid velocity, v the particle velocity, $F_D(u - v)$ the drag force per unit particle mass, g the gravitational acceleration, and the term F_x represents the additional forces, which are introduced in Chapter 4. [6, 17]

In the equation above, F_D is defined as

$$F_D = \frac{18\mu_c C_D Re_r}{\rho_d d_d^2 24}, \quad (19)$$

where μ_c is the dynamic viscosity of the continuous phase, d_d the particle diameter, C_D the drag coefficient, and Re_r the relative Reynolds number. The relative Reynolds number is defined as

$$Re_r = \frac{\rho_c d_d |v - u|}{\mu_c} \quad (20)$$

and the drag coefficient as

$$C_D = \alpha_1 + \frac{\alpha_2}{Re_r} + \frac{\alpha_3}{Re_r^2}, \quad (21)$$

where α_1 , α_2 , and α_3 are constants which apply to smooth spherical particles over several ranges of the relative Reynolds number given by Morsi and Alexander [18]. [6, 7]

The particle-particle interactions and the effects of the particle volume fraction on the continuous phase are negligible in the trajectory method, but they are considered in the Discrete Element Method. [6, 19].

While the continuous phase always has an influence on the particle trajectories, particles also can have an influence on the continuous phase. These effects are referred to as turbulent dispersion and turbulence modulation and they are introduced in detail in Chapters 4.9 and 4.8, respectively. The momentum exchange between the phases is solved from the equation

$$F = \sum [F_D (v - u) + F_x] q_{m,d} \Delta t, \quad (22)$$

where $q_{m,d}$ is the mass flow rate of the particles and Δt is time step. This momentum exchange term appears as a momentum source term in the momentum equation of the continuous phase. [19]

The Eulerian-Lagrangian approach is simple and robust, but the major problem is the number of trajectories needed to represent the particle field and the correspond-

ing computational time. Like mesh resolution and time step, the number of trajectories also affects statistical error. When the mesh is refined, fewer and fewer particles are available in each mesh element to form the mesh-based mean field estimate. Therefore the statistical error is increased. The increase in statistical error eventually overwhelms the reduction in spatial discretization error which is achieved by mesh refinement. [9, 20]

In literature, the Eulerian-Lagrangian approach is preferred in the cases, where the volume fraction of the dispersed phase is lower than 1 % and where particle transportation is modeled under unsteady state conditions, because under unsteady state conditions the computational time is not significantly increased compared to that under steady state conditions. [21–28]

3.2 Eulerian-Eulerian Approach

In the Eulerian-Eulerian approach, particles are treated as a continuum with properties analogous to those of a fluid and thus particle-particle friction is not taken into account [9]. The Navier-Stokes equations are solved for each phase and mass, momentum, and energy transfer between phases is computed using empirical closure relations. In ANSYS Fluent, three types of multiphase model follow the Eulerian-Eulerian approach. They are referred to as Volume of Fluid, Mixture, and Eulerian models. [19]

3.2.1 Volume of Fluid Model

In the Volume of Fluid (VOF) model, the fluids on both sides of the interface are marked by an indicator function (volume fraction, α) which gets values between zero and one. The value of one indicates that the computational cell is full of fluid, while the value of zero indicates that the cell is empty of fluid. Computational cells with values between zero and one contain a free surface. In each cell the values of

volume fraction sum to unity. [29,30]

The volume of fluid model is applicable for stratified or free-surface flows [22, 23, 31]. However, Gopala and van Wachem [30] say that the one drawback of the volume of fluid model is that the exact position of the interface is not known explicitly and thus special techniques are needed to reconstruct the well-defined interface. Those techniques are beyond the scope of this thesis and thus they are not introduced here.

It is assumed that the velocity of the phases is continuous across the interface, but there is a pressure jump at the interface due to the presence of the surface tension [32]. Let's consider only two phases, which are not interpenetrating. The continuity equation is defined as

$$\frac{\partial \rho}{\partial t} + \frac{\partial}{\partial x_i}(\rho u_i) = S + (q_{m,pq} - q_{m,qp}), \quad (23)$$

where S is the source term and the second term on the right hand side is the mass exchange between the phases. The source term is usually assumed to have a value of zero. The subscript q denotes the primary phase and p the secondary phase, respectively. The averaged value of density is defined as

$$\rho = \alpha_p \rho_p + (1 - \alpha_p) \rho_q. \quad (24)$$

The momentum equation is defined as

$$\frac{\partial}{\partial t}(\rho u_i) + \frac{\partial}{\partial x_j}(\rho u_i u_j) = -\frac{\partial p}{\partial x_i} + \rho g + F, \quad (25)$$

where the averaged value of pressure is written as

$$p = \alpha_p p_p + (1 - \alpha_p) p_q \quad (26)$$

and the term F represents the surface tension force. The volume fraction is solved for the secondary phase, p , from the continuity equation (23). For the primary phase, q , it is computed from the following equation. [30]

$$\alpha_q + \alpha_p = 1 \quad (27)$$

In this thesis, no stratified flows are considered and thus the volume of fluid model is not used.

3.2.2 Mixture Model

The mixture model is a simplified formulation of the multiphase flow equations, because the continuity and momentum equations are written for the mixture of the continuous and dispersed phases. The momentum equation contains an additional term representing the effect of velocity differences between the phases. Depending on the exact formulation of the equations used to determine the velocity differences, the mixture model is referred to as a drift-flux, algebraic-slip, suspension, diffusion or local-equilibrium model [33]. If the velocity difference between the phases is neglected, then the mixture model is reduced to the homogeneous multiphase model.

Let's consider the mixture, which consists of n phases. According to Manninen et al. [33], the continuity equation of the mixture is defined as

$$\frac{\partial}{\partial t}(\rho_m) + \frac{\partial}{\partial x_i}(\rho_m u_m) = 0, \quad (28)$$

where the mixture density is written as

$$\rho_m = \sum_{k=1}^n (\alpha_k \rho_k) \quad (29)$$

and the mixture velocity is a mass-averaged velocity

$$u_m = \frac{1}{\rho_m} \sum_{k=1}^n (\alpha_k \rho_k u_k). \quad (30)$$

The subscript k denotes the phase and u_k denotes the phase velocity.

The momentum equation of the mixture is defined as

$$\frac{\partial}{\partial t}(\rho_m u_m) + \frac{\partial}{\partial x_j}(\rho_m u_m u_m) = -\frac{\partial p_m}{\partial x_i} + \frac{\partial}{\partial x_j}(\tau_m + \tau_{Tm}) + \frac{\partial \tau_{Dm}}{\partial x_j} + \rho_m g + F_m, \quad (31)$$

where F_m represents the influence of the surface tension force on the mixture [33].

The pressure of the mixture is written as

$$\frac{\partial p_m}{\partial x_i} = \sum_{k=1}^n (\alpha_k \frac{\partial p_k}{\partial x_i}). \quad (32)$$

However, in practice the phase pressures are often taken to be equal:

$$p_k = p_m. \quad (33)$$

In the momentum equation (31), the three stress tensors are the average viscous stress tensor

$$\tau_m = \sum_{k=1}^n (\alpha_k \tau_k), \quad (34)$$

the turbulent stress tensor

$$\tau_{Tm} = - \sum_{k=1}^n (\alpha_k \overline{\rho_k u'_k u'_k}) \quad (35)$$

and the diffusion stress tensor due to the slip velocity between the phases

$$\tau_{Dm} = - \sum_{k=1}^n (\alpha_k \rho_k u_{Dk} u_{Dk}). \quad (36)$$

The fluctuating component of the velocity of phase k , u'_k , is defined as

$$u'_k = u_{Ik} - u_k, \quad (37)$$

where u_{Ik} represents the local instant velocity of phase k . The diffusion velocity, u_{Dk} , is the velocity of phase k relative to the mixture velocity

$$u_{Dk} = u_k - u_m. \quad (38)$$

According to Ishii and Hibiki [10], the mixture model is appropriate in the cases where the dynamics of two phases are closely coupled. In literature, the mixture model is used, when the volume fraction of secondary phase is in the range from 10 to 20 % [34,35].

3.2.3 Eulerian Model

In the Eulerian model, the continuity and momentum equations are written for each phase. The continuity equation for the continuous phase is defined as

$$\frac{\partial}{\partial t} (\alpha_c \rho_c) + \frac{\partial}{\partial x_i} (\alpha_c \rho_c u_i) = S_c + \sum_{d=1}^n (q_{m,dc} - q_{m,cd}), \quad (39)$$

where S_c is a source term, $q_{m,cd}$ is the mass transfer from the continuous phase to the dispersed phase, and $q_{m,dc}$ is the mass transfer from the dispersed phase to the continuous phase. The sum considers all the dispersed secondary phases if there

is more than one dispersed phase in the system. The momentum equation of the continuous phase is defined as

$$\begin{aligned} \frac{\partial}{\partial t}(\alpha_c \rho_c u_i) + \frac{\partial}{\partial x_j}(\alpha_c \rho_c u_i u_j) = & -\alpha_c \frac{\partial p}{\partial x_i} + \frac{\partial t_{ij}}{\partial x_j} + \alpha_c \rho_c g \\ & + \sum_{d=1}^n (K_{dc}(v-u) + q_{m,dc}v_{dc} - q_{m,cd}v_{cd}) + F, \end{aligned} \quad (40)$$

where F represents all the interfacial forces except pressure [36]. The interfacial forces are presented in Chapter 4.

In Equation (40), the viscous stress tensor, τ_{ij} , is in ANSYS Fluent [19] defined as

$$\tau_{ij} = \alpha_c \mu_c \left(\frac{\partial u_i}{\partial x_j} + \frac{\partial u_j}{\partial x_i} \right) + \alpha_c \left(\lambda_c - \frac{2}{3} \mu_c \right) \frac{\partial u_i}{\partial x_j} \delta_{ij} \quad (41)$$

for the continuous phase. The terms λ and δ_{ij} represent the bulk viscosity and Kronecker's delta, respectively.

The term

$$\sum_{d=1}^n (K_{dc}(v-u) + q_{m,dc}v_{dc} - q_{m,cd}v_{cd}) \quad (42)$$

takes the momentum transfer between phases into account in Equation (40). The first term is interaction force between phases and $K_{dc} = K_{cd}$ represents the momentum exchange coefficient. If mass is transferred from the continuous phase to the dispersed phase, then velocity between phases is defined as follows.

$$\text{If } q_{m,cd} > 0, \text{ then } v_{cd} = v_c.$$

$$\text{If } q_{m,dc} < 0, \text{ then } v_{dc} = v_c.$$

On the other hand, if mass is transferred from the dispersed phase to the continuous phase, then velocity between phases is defined as follows. [19]

$$\text{If } q_{m,dc} > 0, \text{ then } v_{dc} = v_d.$$

$$\text{If } q_{m,cd} < 0, \text{ then } v_{cd} = v_d.$$

As Equation (42) shows, the momentum exchange between the phases is based on the value of the momentum exchange coefficient. Depending on the phases,

which are in the interaction, the coefficient is called as the fluid-fluid exchange coefficient, K_{pq} , and for granular flows, the fluid-solid, K_{fs} , and solid-solid exchange coefficients, K_{kj} . [19]

The fluid-fluid exchange coefficient is defined as

$$K_{pq} = \frac{\alpha_q \alpha_p \rho_p f}{t_p}, \quad (43)$$

where q refers to the primary phase, and p to the secondary phase, respectively. The drag function, f , is defined differently depending on which one of the exchange-coefficient models is used. The particle response time, t_p , is defined as

$$t_p = \frac{\rho_p d_p^2}{18\mu_q}. \quad (44)$$

The fluid-solid exchange coefficient is defined as

$$K_{fs} = \frac{\alpha_s \rho_s f}{t_p}, \quad (45)$$

where subscripts f and s refer to fluid and solid, respectively. Now, the particle response time is defined as

$$t_p = \frac{\rho_s d_s^2}{18\mu_f}. \quad (46)$$

The solid-solid exchange coefficient is defined as

$$K_{kj} = \frac{3g_0(1+e)(\frac{\pi}{2} + C_{fr,kj}\frac{\pi^2}{8})\alpha_k\rho_k\alpha_j\rho_j(d_k+d_j)^2}{2\pi(\rho_k d_k^3 + \rho_j d_j^3)}|v_{kj}|, \quad (47)$$

where j refers to fine particles and k to coarse particles, e is the restitution coefficient, $C_{fr,kj}$ is the friction coefficient between particles of solid-phases j and k , and g_0 is the radial distribution function. The value of the restitution coefficient depends on the particle type, and it characterizes the change in kinetic energy during particle interactions. The value of 1 denotes that kinetic energy is conserved and the collision between particles is perfectly elastic, while the value of 0 denotes that kinetic energy is lost and the collision is perfectly inelastic. The values between 0 and 1 denote that kinetic energy is not totally conserved and the collision is partially elastic. The radial distribution function is defined differently depending on how many solid phases there are in the system. [19, 37]

The equations presented above are for the continuous phase. Similarly as for the continuous phase, the continuity and momentum equations are written for the dispersed phase, too. Thus, the Eulerian model needs more computational effort than the mixture model. Also the complexity of the Eulerian model can make it less stable than the mixture model. Coupling of the two phases is achieved through the pressure and interfacial exchange coefficients. The dispersed phase volume fraction, α_d , is solved from the continuity equation of the dispersed phase, whereas the continuous phase volume fraction is solved from the condition that the volume fractions sum to unity [19]. In literature, the Eulerian model is used over a wide range of the secondary phase volume fraction (3.8 - 50 %). [38–42]

3.3 Turbulence Models

The standard way of modeling turbulent single-phase flow is to derive a Reynolds decomposed and time-averaged form of the Navier-Stokes equations. The velocity field can be decomposed into mean u_m and fluctuating u' components. The Reynolds Averaged Navier-Stokes (RANS) equations differ from the laminar form by the Reynolds stress tensor, τ_{ij} . [8]

In multiphase flows, on the one hand particles can affect the turbulence of the continuous phase, and on the other hand turbulent fluctuations can affect the particle trajectories. The effect of particles on the turbulence of the continuous phase is referred to as turbulence modulation, whereas the effect of continuous phase turbulence on the particle trajectories is referred to as turbulent dispersion. Turbulence modulation and turbulent dispersion are studied in Chapters 4.8 and 4.9, respectively. In the following, the turbulence models used in this thesis are introduced. [9]

3.3.1 Two-Equation Models

Two-equation models like $k - \varepsilon$ and $k - \omega$ models are complete, which means that they can be used to predict properties of a given turbulent flow with no prior knowledge of the structure of the turbulence. There are three different versions of the $k - \varepsilon$ model: the standard $k - \varepsilon$ model, the Re-Normalization Group (RNG) $k - \varepsilon$ model, and the realizable $k - \varepsilon$ model. The equations for the turbulence kinetic energy, k , and the dissipation rate, ε , are developed starting with the Reynolds Averaged Navier-Stokes equations.

The transport equation for the turbulence kinetic energy in the standard $k - \varepsilon$ model is defined as

$$\rho \frac{\partial k}{\partial t} + \rho u_j \frac{\partial k}{\partial x_j} = \tau_{ij} \frac{\partial u_i}{\partial x_j} - \rho \varepsilon + \frac{\partial}{\partial x_j} \left[\left(\mu + \frac{\mu_T}{\sigma_k} \right) \frac{\partial k}{\partial x_j} \right] \quad (48)$$

and for the turbulence dissipation rate as

$$\rho \frac{\partial \varepsilon}{\partial t} + \rho u_j \frac{\partial \varepsilon}{\partial x_j} = C_{1\varepsilon} \frac{\varepsilon}{k} \tau_{ij} \frac{\partial u_i}{\partial x_j} - C_{2\varepsilon} \rho \frac{\varepsilon^2}{k} + \frac{\partial}{\partial x_j} \left[\left(\mu + \frac{\mu_T}{\sigma_\varepsilon} \right) \frac{\partial \varepsilon}{\partial x_j} \right]. \quad (49)$$

In the $k - \varepsilon$ model, the eddy viscosity is defined as

$$\mu_T = \frac{\rho C_\mu k^2}{\varepsilon} \quad (50)$$

and the constants are $C_{1\varepsilon} = 1.44$, $C_{2\varepsilon} = 1.92$, $C_\mu = 0.09$, $\sigma_k = 1.0$, and $\sigma_\varepsilon = 1.3$. [16]

The standard $k - \varepsilon$ model is inaccurate for flows with adverse pressure gradient and it is difficult to integrate through the viscous sublayer, because it is based on fully-turbulent flows. [16, 43]

The basic form of the re-normalization group (RNG) $k - \varepsilon$ model is similar to the standard $k - \varepsilon$ model, but it includes refinements. The RNG $k - \varepsilon$ model is more appropriate for swirling flows, rapidly strained flows, and it also takes into account low Reynolds number effects. In the RNG $k - \varepsilon$ model, the transport equations have the same form as in the standard $k - \varepsilon$ model, but the constants have different

values: $C_{1\varepsilon} = 1.42$, $C_\mu = 0.0845$, $\sigma_k = 0.7194$, and $\sigma_\varepsilon = 0.7194$. In addition, the constant $C_{2\varepsilon}$ is replaced with the function $C_{2\varepsilon}^*$, which is defined as

$$C_{2\varepsilon}^* = 1.68 + \frac{C_\mu \eta^3 (1 - \frac{\eta}{\eta_0})}{1 + \beta \eta^3}, \quad (51)$$

where the dimensionless variable, η is written as

$$\eta = \frac{Sk}{\varepsilon} \quad (52)$$

$$S = \sqrt{2S_{ij}S_{ij}} \quad (53)$$

and the mean strain rate tensor is defined as

$$S_{ij} = \frac{1}{2} \left(\frac{\partial u_i}{\partial x_j} + \frac{\partial u_j}{\partial x_i} \right). \quad (54)$$

The constants η_0 and β have the values of 4.38 and 0.012, respectively. [25, 44]

According to developers of the realizable $k - \varepsilon$ model [45], the model enhances numerical stability in turbulent flow calculations, and it captures the flow phenomena better than the standard $k - \varepsilon$ model in the case of rotating, boundary shear, channel, and backward facing step flows. In the realizable $k - \varepsilon$ model, the transport equation of turbulence kinetic energy has the same form as in the standard $k - \varepsilon$ model, but the transport equation of dissipation rate is defined as

$$\rho \frac{\partial \varepsilon}{\partial t} + \rho u_j \frac{\partial \varepsilon}{\partial x_j} = C_1 \rho \varepsilon S - C_{2\varepsilon} \rho \frac{\varepsilon^2}{k + \sqrt{\nu \varepsilon}} + \frac{\partial}{\partial x_j} \left[\left(\mu + \frac{\mu_T}{\sigma_\varepsilon} \right) \frac{\partial \varepsilon}{\partial x_j} \right], \quad (55)$$

where

$$C_1 = \max \left(0.43, \frac{\eta}{\eta + 5} \right) \quad (56)$$

and the dimensionless variable η is defined similarly as in the RNG model. In addition, the constant C_μ , which is used to calculate the eddy viscosity in Equation (50) is replaced by a function

$$C_\mu = \frac{1}{A_0 + A_s U^* \frac{k}{\varepsilon}}, \quad (57)$$

where

$$U^* = \sqrt{S_{ij}S_{ij} + \Omega_{ij}\Omega_{ij}} \quad (58)$$

$$\Omega_{ij} = \frac{1}{2} \left(\frac{\partial u_i}{\partial x_j} - \frac{\partial u_j}{\partial x_i} \right) \quad (59)$$

$$A_s = \sqrt{6} \cos \phi \quad (60)$$

$$\phi = \frac{1}{3} \arccos(\sqrt{6}W) \quad (61)$$

$$W = \frac{S_{ij}S_{jk}S_{ki}}{\tilde{S}^3} \quad (62)$$

$$\tilde{S} = \sqrt{S_{ij}S_{ij}} \quad (63)$$

and the constants are: $C_{2\varepsilon} = 1.9$, $\sigma_k = 1.0$, $\sigma_\varepsilon = 1.2$, and $A_0 = 4.0$. [45]

The $k - \omega$ model is more accurate for flows with favorable or adverse pressure gradients than the $k - \varepsilon$ model, and it can be easily integrated through the viscous sublayer. With viscous corrections included, the $k - \omega$ model is accurate near a solid boundary and even describes boundary layer transition reasonably well according to Wilcox [16]. The transport equation of the turbulence kinetic energy is defined as

$$\rho \frac{\partial k}{\partial t} + \rho u_j \frac{\partial k}{\partial x_j} = \tau_{ij} \frac{\partial u_i}{\partial x_j} - \beta^* \rho k \omega + \frac{\partial}{\partial x_j} [(\mu + \mu_T \sigma^*) \frac{\partial k}{\partial x_j}], \quad (64)$$

the transport equation of the specific dissipation rate as

$$\rho \frac{\partial \omega}{\partial t} + \rho u_j \frac{\partial \omega}{\partial x_j} = \alpha \frac{\omega}{k} \tau_{ij} \frac{\partial u_i}{\partial x_j} - \beta \rho \omega^2 + \frac{\partial}{\partial x_j} [(\mu + \mu_T \sigma) \frac{\partial \omega}{\partial x_j}], \quad (65)$$

and the eddy viscosity as

$$\mu_T = \frac{\rho k}{\omega}. \quad (66)$$

The constants of the $k - \omega$ model are: $\alpha = \frac{5}{9}$, $\beta = \frac{3}{40}$, $\beta^* = 0.09$, $\sigma = \frac{1}{2}$, and $\sigma^* = \frac{1}{2}$. [16]

The shear-stress transport (SST) $k - \omega$ model uses a blending function to combine the standard $k - \omega$ model in the inner region (1) of the boundary layer and the standard $k - \varepsilon$ model in the outer region (2) and in free shear flows. Also the definition of the eddy viscosity is modified. The SST model avoids the free stream sensitivity of the standard $k - \omega$ model, takes into account the effect of the transport of the principal turbulent shear stress, and improves the prediction of adverse pressure gradient flows. [46,47]

The transport equation of the turbulence kinetic energy is defined as

$$\rho \frac{\partial k}{\partial t} + \rho u_j \frac{\partial k}{\partial x_j} = \tilde{P}_k - \beta^* \rho k \omega + \frac{\partial}{\partial x_j} [(\mu + \mu_T \sigma_k) \frac{\partial k}{\partial x_j}]. \quad (67)$$

The term \tilde{P}_k is the production limiter, which prevents the build-up of turbulence in stagnation regions.

$$\tilde{P}_k = \min(P_k, 10 \beta^* \rho k \omega) \quad (68)$$

$$P_k = \mu_T \frac{\partial u_i}{\partial x_j} \left(\frac{\partial u_i}{\partial x_j} + \frac{\partial u_j}{\partial x_i} \right) \quad (69)$$

The transport equation of the specific dissipation rate is defined as

$$\begin{aligned} \rho \frac{\partial \omega}{\partial t} + \rho u_j \frac{\partial \omega}{\partial x_j} &= \alpha \rho S^2 - \beta \rho \omega^2 + \frac{\partial}{\partial x_j} [(\mu + \mu_T \sigma_\omega) \frac{\partial \omega}{\partial x_j}] \\ &+ 2(1 - F_1) \rho \sigma_{\omega 2} \frac{1}{\omega} \frac{\partial k}{\partial x_j} \frac{\partial \omega}{\partial x_j}, \end{aligned} \quad (70)$$

and the eddy viscosity as

$$\mu_T = \frac{\rho a_1 k}{\max(a_1 \omega, S F_2)}, \quad (71)$$

where S is the strain rate magnitude. The blending functions are defined as

$$F_1 = \tanh \left\{ \left\{ \min \left[\max \left(\frac{\sqrt{k}}{\beta^* \omega y}, \frac{500\nu}{y^2 \omega} \right), \frac{4\rho \sigma_{\omega 2} k}{CD_{k\omega} y^2} \right] \right\}^4 \right\} \quad (72)$$

$$F_2 = \tanh \left\{ \left[\max \left(\frac{2\sqrt{k}}{\beta^* \omega y}, \frac{500\nu}{y^2 \omega} \right) \right]^2 \right\}, \quad (73)$$

where the term y is the distance to the nearest wall and

$$CD_{k\omega} = \max \left(2\rho \sigma_{\omega 2} \frac{1}{\omega} \frac{\partial k}{\partial x_j} \frac{\partial \omega}{\partial x_j}, 10^{-10} \right). \quad (74)$$

The first blending function F_1 is equal to zero away from the surface ($k - \varepsilon$ model), and switches over to one inside the boundary layer ($k - \omega$ model). Each of the constants is a blend of the corresponding constants of the $k - \varepsilon$ and $k - \omega$ models:

$$\alpha = F_1 \alpha_1 + (1 - F_1) \alpha_2. \quad (75)$$

The constants of the SST $k - \omega$ model are: $a_1 = 0.31$, $\alpha_1 = \frac{5}{9}$, $\alpha_2 = 0.44$, $\beta_1 = \frac{3}{40}$, $\beta_2 = 0.0828$, $\beta^* = 0.09$, $\sigma_{k1} = 0.85$, $\sigma_{k2} = 1.0$, $\sigma_{\omega 1} = 0.5$, and $\sigma_{\omega 2} = 0.856$. [47]

Two-equation models are inaccurate for recirculating flows, unreliable for boundary layer separation and they cannot predict secondary flows in noncircular duct flow. These difficulties are based on the Boussinesq approximation, which assumes that the eddy viscosity is an isotropic scalar quantity. This assumption can lead to inaccurate results. According to Dehbi [48], the turbulent velocity fluctuations are not isotropic near the wall, and the root mean square (rms) of the normal component of velocity, u'_j , can be orders of magnitudes smaller than the streamwise, u'_i , or spanwise, u'_k , components. Thus, in two-phase flow, particles are slowed considerably in the boundary layer compared to what would be expected if the flow field was wholly isotropic. However, two-equation models can save a lot of computational time and effort compared to Large Eddy Simulation (LES) and Direct Numerical Simulation (DNS), still providing reasonable results for the engineering applications. [16, 48, 49]

To solve the transport equations of turbulence quantities the dispersed, mixture, and per-phase models can be used in ANSYS Fluent software, when multiphase flow is modeled using the Eulerian model and turbulence is modeled using $k - \varepsilon$ or $k - \omega$ model. The mixture turbulence model uses mixture properties and velocities to estimate the values of turbulence quantities. The dispersed turbulence model derives the turbulence of dilute dispersed phase from the turbulence of the continuous phase. In the dispersed turbulence model, there are equations of k and ε or ω for the continuous phase, which contain terms to take the influence of the dispersed phase into account. The per-phase turbulence model solves a set of k and ε or ω transport equations for each phase. [50]

It seems that the most popular method to take the interaction between particles and turbulent fluctuations into account in literature is the standard $k - \varepsilon$ model with mixture properties. [24, 26, 38–40]

3.3.2 Reynolds Stress Model

To derive the differential equation for the Reynolds stress tensor, the Navier-Stokes equation is multiplied by a fluctuating property and the product is time averaged. This leads to 26 unknown correlations because of the non-linearity of Navier-Stokes equations. Thus, the approximations need to be devised for the unknown correlations to close the system of equations. The modeling of individual Reynolds stresses accounts for the anisotropy of Reynolds stresses. According to Wilcox [16], the Reynolds stress equation is written as

$$\frac{\partial \tau_{ij}}{\partial t} + u_k \frac{\partial \tau_{ij}}{\partial x_k} = -\tau_{ik} \frac{\partial u_j}{\partial x_k} - \tau_{jk} \frac{\partial u_i}{\partial x_k} + \varepsilon_{ij} - \Pi_{ij} + \frac{\partial}{\partial x_k} [v \frac{\partial \tau_{ij}}{\partial x_k} + C_{ijk}], \quad (76)$$

where

$$\varepsilon_{ij} = \overline{2\mu \frac{\partial u'_i}{\partial x_k} \frac{\partial u'_j}{\partial x_k}} \quad (77)$$

$$\Pi_{ij} = \overline{p' \left(\frac{\partial u'_i}{\partial x_j} \frac{\partial u'_j}{\partial x_i} \right)} \quad (78)$$

$$C_{ijk} = \overline{\rho u'_i u'_j u'_k} + \overline{p' u'_i} \delta_{jk} + \overline{p' u'_j} \delta_{ik} \quad (79)$$

In Equations (77) - (79), the prime denotes the fluctuating property and δ_{ij} is Kronecker's delta.

To solve the transport equations of turbulence quantities the dispersed and mixture models can be used in ANSYS Fluent software, when multiphase flow is modeled using the Eulerian model and turbulence is modeled using Reynolds stress model. [19]

3.3.3 Direct Numerical Simulation

Flow models based on Direct Numerical Simulation (DNS) are complete time-dependent solutions of the Navier-Stokes and continuity equations with no assumptions concerning Reynolds stress. In direct numerical simulation, the computational mesh must be dense enough to resolve the smallest scale of turbulence, the Kol-

mogorov length scale. If every particle were included in the calculation, the discrete element method would provide a direct numerical simulation. [9, 16]

3.3.4 Large Eddy Simulation

The Large Eddy Simulation (LES) is used to model turbulence in multiphase flows, too [21, 51]. It is appropriate for turbulent flows including separation, reattachment, and recirculation zones. The large eddy simulation computes large eddies and models small eddies. In order to separate the large scale and small scale eddies, the three-dimensional, time-dependent Navier-Stokes equations are filtered. Because the smallest eddies are modeled, the smallest computational cells can be much larger than the smallest (Kolmogorov) length scale and the time steps can be much larger than in the DNS. Thus, the LES needs less computational effort and time than the DNS. In this thesis, only two-equation models and Reynolds stress model are used to model turbulence because of the limited computational power and time. [16, 51]

3.3.5 Near Wall Treatment

If the Reynolds number is large enough, viscous effects are important only near the surface of the wall. In the boundary layer, the flow behaves as viscous flow and outside the boundary layer as inviscid flow, although the viscosity is the same within and outside the boundary layer. The boundary layer is a consequence of the no-slip boundary condition, which demands that the velocity component tangential to the wall is zero at the surface of the wall. By definition, the boundary layer is the region near the wall, where velocity is less than 99 percent of the free stream velocity. It consists of three regions: viscous sublayer, log layer and defect layer (Figure 3). [52]

Within the boundary layer, the velocity gradients are much larger than those in the

remainder of the flow field. Due to the definition of the viscous shear stress for laminar flow, τ_{lam} ,

$$\tau_{\text{lam}} = \mu \frac{du}{dy}, \quad (80)$$

viscous effects are confined to the boundary layer. For turbulent flows the shear stress is the sum of the laminar (viscous) shear stress and the turbulent shear stress, τ_T , which is called as Reynolds stress.

$$\tau = \tau_{\text{lam}} + \tau_T. \quad (81)$$

When the Boussinesq approximation is used, the Reynolds stress can be written in terms of the eddy viscosity, μ_T , which is defined differently depending on the used turbulence model. [52]

$$\tau_T = -\rho \overline{u'_i u'_j} = \mu_T \frac{d\bar{u}}{dy} \quad (82)$$

The viscous sublayer is the region between the surface of the wall and the log layer, where the velocity varies approximately linearly with the dimensionless normal dis-

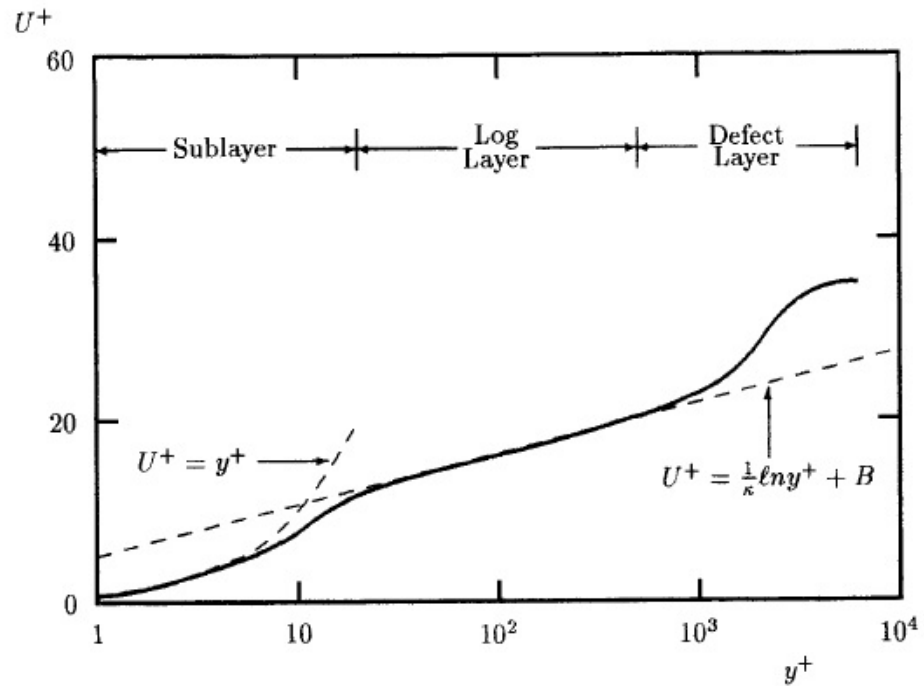


Figure 3. Three regions in the boundary layer [16].

tance, y^+ ,

$$y^+ = \frac{u_\tau y}{\nu}, \quad (83)$$

where u_τ is the friction velocity

$$u_\tau = \sqrt{\frac{\tau_w}{\rho}} \quad (84)$$

and τ_w is the wall shear stress. [16]

The log layer is the region sufficiently close to the wall surface between the viscous sublayer and defect layer. It typically lies between $y^+ = 30$ and $y = 0.1\delta$, where δ is the boundary layer thickness. Within the log layer, the law of the wall holds.

$$u^+ = \frac{1}{\kappa} \ln y^+ + B \quad (85)$$

In the law of the wall, the dimensionless velocity, u^+ , is defined as

$$u^+ = \frac{u}{u_\tau}, \quad (86)$$

the von Kármán constant $\kappa \approx 0.41$ and the constant $B \approx 5.0$ for smooth surfaces. For rough surfaces the constant B is a function of dimensionless surface roughness, k_s^+ . [16, 52]

$$k_s^+ = \frac{u_\tau k_s}{\nu} \quad (87)$$

$$B = 8.5 + \frac{1}{\kappa} \ln\left(\frac{1}{k_s^+}\right) \quad (88)$$

The term k_s denotes the surface roughness.

The defect layer lies between the log layer and the edge of the boundary layer. In the viscous sublayer, the laminar shear stress is greater than the turbulent one, while the turbulent shear stress is greater than the laminar one in the defect layer, as shown in Figure 4. [16, 52]

In order to apply a two-equation turbulence model to wall-bounded flows, the boundary conditions appropriate to a solid boundary for the velocity and two turbulence parameters must be specified according to Bredberg [53]. To take near wall treatment into account, there are two different approaches. The first approach is the

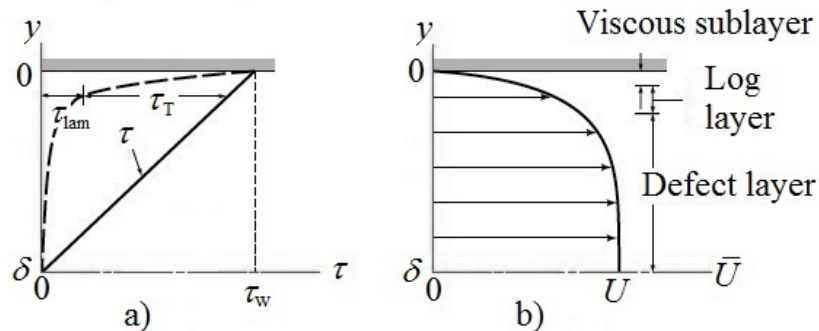


Figure 4. Structure of turbulent flow near the wall surface. a) Shear stress b) Average velocity. Modified from [52].

low Reynolds number (LRN) approach, which uses a refined mesh close to the wall in order to resolve the velocity and two turbulence parameters. The second one is the high Reynolds number (HRN) approach, which links the near-wall region using wall functions.

In the LRN approach, the first computational cell must have its centroid in $y^+ \sim 1$. The HRN approach, also called as wall function approach, uses the law of the wall to specify the boundary condition for velocity and two turbulence parameters by adopting a mesh, where the first computational cell is in the log layer (where the law of the wall is valid). Wilcox [16] reminds that the law of the wall does not always hold for flows near solid boundaries, for example for separated flows. However, to avoid extremely dense mesh, the wall function approach is used in the present work. [53]

4 PHASE INTERACTION

Interaction between the dispersed and continuous phases refers to the exchange of properties between phases and is responsible for coupling between phases in dispersed phase flows. Coupling can take place through mass, momentum and energy transfer between phases. Energy coupling can be effected in convection, radiation and internal heating. In a dilute dispersed phase flow the particle motion is con-

trolled by the generalized interfacial drag force. The generalized interfacial drag force acting on the dispersed phase is the linear combination of interfacial surface forces: the steady-state drag force, buoyancy (or pressure) force, lift force, virtual mass force, Basset (or history) force, body force, wall lift (or lubrication) force, and turbulent dispersion force. In a dense flow, the particle motion is also controlled by collisions between other particles, whereas in dilute flows particle-particle interaction is negligible. [9, 10]

4.1 Dimensionless Groups

The volume fraction of the dispersed phase has a major impact on phase interactions [19]. According to Hiltunen et al. [7], the delineation between dilute and dense particulate flows is mathematically established by the particle response time, t_p , and the mean time between successive collisions between particles, t_m . The particle response time for a rigid sphere in Stokes flow (a low Reynolds number flow, $Re_r < 1$) is defined as

$$t_p = \frac{\rho_d d_d^2}{18 \mu_c}, \quad (89)$$

where d_d is the diameter of the particle and μ_c is the dynamic viscosity of the continuous phase. The relative Reynolds number, Re_r , is defined in Equation (20).

For $Re_r > 1$, the particle response time, t_p , is defined as

$$t_p = \frac{4 \rho_d d_d}{3 \rho_c C_D u_{cd}}, \quad (90)$$

where C_D is the drag coefficient of the particle and u_{cd} is the relative velocity between the continuous and dispersed phases. [7]

In the Newton regime ($Re_r > 1000$) the drag coefficient is constant and the particle response time is defined as

$$t_p = \frac{4 \rho_d d_d}{3 \rho_c C_D u_t}, \quad (91)$$

where u_t denotes the terminal velocity. Terminal velocity is zero, when $\rho_c = \rho_d$. [9]

The time between collisions, t_m , can be estimated from the equation for collision frequency

$$f_c = n \pi d_d^2 v_r \quad (92)$$

where n is the number density of the particles, and v_r is a relative velocity of one particle with respect to the other particles [9]. Thus, the time between collisions is

$$t_m = \frac{1}{f_c} = \frac{1}{n \pi d_d^2 v_r}. \quad (93)$$

The ratio of the particle response time to the time between collisions in Stokes flow can be written as follows [9].

$$\frac{t_p}{t_m} = \frac{n \pi \rho_d d_d^4 v_r}{18 \mu_c} = \frac{\bar{\rho}_d d_d v_r}{3 \mu_c} \quad (94)$$

Depending on the dispersed phase volume fraction, the degree of interaction between the phases can be divided into three categories. In a dilute flow with very low dispersed phase volume fraction

$$\frac{t_p}{t_m} < 1 \quad (95)$$

$$\alpha_d < 10^{-6}, \quad (96)$$

in which case the particle has enough time to respond to the surrounding fluid field before the next collision, and the motion of the particle is primarily controlled by the fluid flow. The coupling between the phases is one-way, which means that the continuous phase influences the dispersed phase via drag and turbulence, but the dispersed phase has no influence on the continuous phase. [7, 9, 54]

For the dispersed phase volume fraction in the range of

$$10^{-6} \leq \alpha_d \leq 10^{-3} \quad (97)$$

the coupling is two-way, which means that the continuous phase influences the dispersed phase via drag and turbulence and the dispersed phase influences the continuous phase via reduction in mean momentum and turbulence. [9, 54]

In a dense flow with high dispersed phase volume fraction, the effect of particle-particle interaction becomes important.

$$\frac{t_p}{t_m} > 1 \quad (98)$$

$$\alpha_d > 10^{-3} \quad (99)$$

The motion of a particle is significantly affected by interactions with other particles. These flows represent the case of four-way coupling where information is transferred from the continuous phase to the dispersed phase and vice versa, and also between the particles. [7, 19, 54]

The resulting concentration profiles due to the phase interaction can be determined by two dimensionless numbers: the Stokes number, and the Froude number. The Stokes number is the measure of the influence of particle inertia on the dispersion of particles by fluid turbulence. It is used to specify how well the particle can respond to the mean flow. The Stokes number is defined as

$$St = \frac{t_p}{t_s}, \quad (100)$$

where t_p denotes the particle response time and t_s the system response time. [7, 55]

The system response time (or the time scale of the mean flow) is defined as

$$t_s = \frac{l_s}{u_s}, \quad (101)$$

where l_s is the characteristic length of the system and u_s is the characteristic velocity of the system. In wall bounded flows, $t_p > t_s$ corresponds to a decreasing response of particles on the fluid turbulence. For $St \ll 1$, particles will follow the flow closely and the deposition flux is low all around the pipe wall. For $St \approx 1$, particles follow the flow quite well, the effect of the boundary layer on the deposition is limited, and the deposition flux due to turbulence is high all around the pipe wall. Particles also tend to avoid regions of vorticity and concentrate in regions of high strain [56]. For $St \gg 1$ particles will move independently of the flow, the deposition is not affected by the boundary layer, and the deposition flux is large at the bottom of the pipe and small at the top, due to gravity. [55]

The Froude number based on the friction velocity is defined as

$$Fr_\tau = \frac{u_\tau^2}{gH}, \quad (102)$$

where H is the height of the duct. For small value of Fr_τ/St , the deposition flux is controlled by gravitational settling, whereas for large value of Fr_τ/St it is controlled by turbulence of the fluid. [55]

The pipe Froude number, Fr_d , indicates the inertial forces of the suspension relative to the gravitational forces. It is defined as

$$Fr_d = \frac{u_m^2}{gd \left(\frac{\rho_d}{\rho_c} - 1 \right)}, \quad (103)$$

where d is the pipe diameter and u_m average velocity of mixture in the pipe. [12]

In the following chapters, the interfacial forces on the particles are introduced. The forces which act on the particle are: the steady-state drag force, buoyancy (or pressure) force, lift force, virtual mass force, Basset (or history) force, body force, wall lift (lubrication) force, and turbulent dispersion force.

4.2 Drag Force

Under non-accelerating conditions, the interaction between the continuous phase and the dispersed phase is taken into account by drag force. The steady-state drag force acts on the particle in a uniform pressure field when there is no acceleration of the relative velocity between the continuous and dispersed phases. The steady-state drag force is defined as

$$F_D = -\frac{1}{2} C_D \rho_c A_d (u_c - u_d) |u_c - u_d|, \quad (104)$$

where A_d is the representative area of the particle. Typically the area is the projected area of the particle in the direction of the relative velocity [9, 17].

For the Eulerian-Lagrangian approach, there are eight laws for the drag coefficient, C_D , available in the ANSYS Fluent software [19].

1. Spherical drag law
2. Non-spherical drag law
3. Stokes-Cunningham drag law
4. High-Mach-number drag law
5. Dynamic drag model theory
6. The Wen and Yu drag model
7. The Gidaspow drag model
8. The Syamlal-O'Brien drag model

The spherical drag law is applicable for spherical particles and the non-spherical drag law for non-spherical particles, respectively. The Stokes-Cunningham drag law is applicable for sub-micron particles. The high-Mach-number drag law is applicable when a particle Mach number is greater than 0.4 at a particle Reynolds number greater than 20. Dynamic drag model theory determines the droplet drag coefficient dynamically, taking the variations in the droplet shape into account.

For the Eulerian-Eulerian approach in the case of liquid-solid two-phase flows, there are three available models for the drag coefficient. The models are the Wen and Yu, Gidaspow, and Syamlal-O'Brien models. The Wen and Yu model is recommended for dilute flows, while the Gidaspow and Syamlal-O'Brien models are recommended for dense fluidized beds.

4.3 Buoyancy Force

The effect of the local pressure gradient gives rise to a force in the direction of the pressure gradient. The pressure gradient produced by a hydrostatic pressure is

$$F_P = \rho_c g V_d, \quad (105)$$

where V_d is the particle volume. This is known as Archimedes principle, which states that the force is equal to the weight of the fluid displaced. In the Eulerian-Lagrangian approach, the equation of motion of a particle including buoyancy effect

is written as

$$\frac{dv}{dt} = F_D(u - v) + \frac{g(\rho_d - \rho_c)}{\rho_d} + F_x. \quad (106)$$

If the dispersed phase density is much larger than the continuous phase density

$$\frac{\rho_d}{\rho_c} \gg 1, \quad (107)$$

the buoyancy force can be neglected according to Crowe et al. [9]. When $\rho_c = \rho_d$, particles are neutrally buoyant and the terminal velocity, u_t , is zero, as in the case of Equation (91).

4.4 Lift Force

Lift forces on the particle due to particle rotation are the Saffman lift force and Magnus force. The Saffman lift force is due to the pressure distribution developed on a particle due to rotation induced by a velocity gradient. The Magnus force is due to rotation of the particle. Lift forces can be neglected in the case of closely packed particles and very small particles. It is more significant for larger particles and in cases where the phases separate quickly. [9, 10, 57]

4.5 Virtual Mass and Basset Forces

In an unsteady flow, there are additional effects due to the inertia of the fluid. The forces due to acceleration of the relative velocity can be divided into two parts: the virtual (or added) mass force and the Basset (or history) force. If the dispersed phase is accelerated relative to the continuous phase, the part of the continuous phase has to be accelerated as well. [9, 17, 58]

The virtual mass force is the force required to accelerate the apparent mass of the surrounding continuous phase when the relative velocity changes.

$$F_V = -\frac{1}{2}\rho_c V_d(a_c - a_d) \quad (108)$$

The Basset force is the effect of the acceleration on viscous drag and the boundary layer development.

$$F_B = -\frac{3}{2}d_d^2\sqrt{\pi\rho_c\mu_m}\int_0^t\frac{a_c-a_d}{\sqrt{t-t'}}dt' \quad (109)$$

The value of the Basset force depends on the acceleration history up to the present time. Due to its complicated time integral form, the Basset force is difficult to evaluate and it is often neglected, although it is important in many unsteady applications. [9, 10]

The terms have a negative sign, because they represent additional drag forces [10]. If the discrete phase density is much larger than the continuous phase density

$$\frac{\rho_d}{\rho_c} \gg 1, \quad (110)$$

the virtual mass and Basset forces can be neglected according to Hiltunen et al. [7] and Crowe et al. [9].

4.6 Body Force

The most common body force is gravity. According to Crowe et al. [9], other body forces are for example Coulomb forces and thermophoretic forces. Coulomb forces are responsible for the operation of an electrostatic precipitator. Thermophoretic forces may be important to the motion of small particles in flows with high temperature gradients such as plasmas.

4.7 Wall Lift Force

The wall lift (or lubrication) force is due to the velocity distribution change around a particle near a wall. The wall lift force is used to predict the observed void profiles for co-current laminar upward and downward liquid-gas flows. It acts on a bubble near a wall to prevent the bubble from touching the wall. This thesis considers liquid-solid flows only. Hence, the wall lubrication force is neglected in the

simulations. [10]

4.8 Turbulence Modulation

The effect of particles on the turbulence of the continuous phase is referred to as turbulence modulation. The presence of particles can both augment and attenuate turbulence. The wakes behind particles are responsible for the additional production of turbulence while the particle-eddy interaction is responsible for the additional dissipation of turbulence. Additional turbulence is produced due to the velocity gradient, which is generated as the instantaneous velocity of the continuous phase equals to the particle velocity at the surface of the particle. On the other hand, turbulent eddies accelerate particles due to the momentum transfer between phases, and thus turbulence is dissipated. In dense particulate flows, the flow field can be disturbed by collisions between particles. [9, 59]

Studies made by Crowe [60] show that small particles tend to dissipate turbulence of the continuous phase while large particles tend to produce turbulence. The augmentation in turbulence intensity is significant when the ratio of particle diameter to turbulence length scale is greater than 0.1. According to Elghobashi [54], particles produce turbulence when the ratio between particle response time and Kolmogorov time scale is

$$\frac{t_p}{t_K} > 100 \quad (111)$$

and on the other hand, particles dissipate turbulence when

$$\frac{t_p}{t_K} < 100. \quad (112)$$

The Kolmogorov time scale is defined as

$$t_K = \left(\frac{\nu}{\varepsilon} \right)^{\frac{1}{2}}. \quad (113)$$

According to Crowe [60], there is no generally accepted model for the effect of particles on the continuous phase turbulence. However, several models have been

proposed to take the effect of particles into account. These models are referred to as standard, consistent, and semi-empirical approach by Lain and Sommerfeld [61].

The standard approach derives the source term of turbulence due to particles using Reynolds averaging. Because the source term acts always as a sink for turbulence kinetic energy, the standard approach is only able to predict dissipation of turbulence. [59]

The consistent approach derives the turbulence equations for particulate flow by considering that the instantaneous continuous phase velocity at the surface of the particle must be equal to particle velocity. This results in a term which for dilute flows is always positive and thus only acts as a source for turbulence kinetic energy. In contrast to the standard approach, the consistent approach is only able to predict production of turbulence. [59]

In the semi-empirical approach, the source terms are defined as functional relationships of the particle related parameters. The semi-empirical approach is able to predict both attenuation and augmentation of turbulence, but it is not derived from the balance equations and thus it does not provide a theoretical base analogous to the standard and consistent approaches. [59]

In ANSYS Fluent, the effect of particles on the continuous phase turbulence can be taken into account enabling the two-way turbulence coupling when using the Eulerian-Lagrangian approach (the discrete phase model). When using the Eulerian-Eulerian approach (Eulerian model in ANSYS Fluent), turbulence modulation can be taken into account using source terms derived by Troshko-Hassan [62], Sato [63], or Simonin and Viollet [64]. However, these source terms are validated for bubbly flows, and thus they are not valid for particulate flow studied in this thesis.

4.9 Turbulent Dispersion Force

The effect of continuous phase velocity fluctuations on the particle trajectories is referred to as turbulent dispersion. Particles get caught up in turbulent eddies of continuous phase, and they are carried from regions of high concentration to regions of low concentration [65].

In the Eulerian-Lagrangian approach, dispersion of particles due to turbulent fluctuations can be modeled using either the stochastic tracking model (discrete random walk model) or the particle cloud model. The stochastic tracking model includes the effect of instantaneous turbulent velocity fluctuations on the particle trajectories by means of stochastic methods. To simulate the interaction of a particle and turbulent eddy, each eddy is characterized by a Gaussian distributed random velocity fluctuation and a time scale. For two-equation models, the isotropy of Reynolds stresses is assumed, and thus the Gaussian distributed velocity fluctuations are written as

$$u'_i = \zeta \sqrt{u_i'^2} \quad (114)$$

$$\sqrt{u_i'^2} = \sqrt{u_j'^2} = \sqrt{u_k'^2} = \sqrt{\frac{2}{3}k}, \quad (115)$$

where ζ is the Gaussian distributed random number and k is the turbulence kinetic energy. For Reynolds stress model the nonisotropy of Reynolds stresses is assumed, and thus the Gaussian distributed velocity fluctuations are written as

$$u'_i = \zeta \sqrt{u_i'^2} \quad (116)$$

$$u'_j = \zeta \sqrt{u_j'^2} \quad (117)$$

$$u'_k = \zeta \sqrt{u_k'^2}. \quad (118)$$

The time scale can be defined either as a constant value

$$\tau = 2T_L \quad (119)$$

or as a random value

$$\tau = -T_L \ln(r), \quad (120)$$

where T_L is the fluid Lagrangian integral time

$$T_L = C_L \frac{k}{\varepsilon}, \quad (121)$$

C_L is 0.15 for two-equation models and 0.30 for Reynolds stress model, and r is uniform random number between 0 and 1. [19, 25]

The particle cloud model tracks the statistical evolution of a cloud of particles about a mean trajectory. The concentration of particles within the cloud is represented by a Gaussian probability density function about the mean trajectory. [19]

In the Eulerian-Eulerian approach, the effect of turbulent fluctuations on the dispersed phase can be taken into account by source terms. ANSYS Fluent offers three different models for turbulent dispersion: the model of Lopez de Bertadano, the model of Simonin, and the model of Burns et al. In the model of Lopez de Bertadano, the turbulent dispersion force is defined as

$$F_T = -\frac{V_d}{\alpha_d} C_T \rho_c k_c \nabla \alpha_d, \quad (122)$$

where C_T is the coefficient and k_c is the turbulence kinetic energy of the continuous phase. The model of Simonin defines the turbulent dispersion force as

$$F_T = -C_T K_{pq} \frac{D_{pq}}{\sigma_{pq}} \left(\frac{\nabla \alpha_p}{\alpha_p} - \frac{\nabla \alpha_q}{\alpha_q} \right), \quad (123)$$

where K_{pq} is the fluid-fluid exchange coefficient, D_{pq} is the fluid-particulate dispersion tensor, and σ_{pq} is the dispersion Prandtl number. Burns et al. [65] derived the turbulent dispersion force based on the Favre averaging of the interfacial drag force:

$$F_T = -\frac{V_d}{\alpha_d} C_T K_{pq} \frac{\nu_T}{S_{C_T}} \left(\frac{\nabla \alpha_p}{\alpha_p} - \frac{\nabla \alpha_q}{\alpha_q} \right), \quad (124)$$

where ν_T is the eddy viscosity, and S_{C_T} is the turbulent Schmidt number (0.9). [10, 19, 66]

Because the study of Burns et al. [65] shows that the model of Burns et al. encompasses other models, it has a wide range of universality, and it is validated for both gas-liquid and liquid-solid flows in laboratory scale, the effect of the model of Burns et al. on the results is studied in this thesis.

4.10 Surface Tension Force

Surface tension is a force, which acts only at the surface. It balances the radially inward inter-molecular attractive force with the radially outward pressure gradient force across the surface. For $Re \ll 1$, surface tension effects depend on the capillary number, Ca , which expresses the ratio of viscous to capillary stresses

$$Ca = \frac{\mu u}{\sigma}, \quad (125)$$

where u is free stream velocity and σ surface tension. For $Re \gg 1$, the importance of surface effects is determined based on the value of the Weber number

$$We = \frac{\rho l u^2}{\sigma}. \quad (126)$$

Surface tension effects can be neglected if Ca or $We \gg 1$. Surface tension force is appropriate when using the volume of fluid model for stratified flows. [19]

5 TWO-PHASE FLOW SIMULATION METHODS

In the present work, the studied part of the wastewater treatment process is the mixing tank, where the wastewater from the primary settling tanks is mixed with the overflow wastewater before the mixture flows to the aeration tanks through the effluent pipes. The overflow wastewater has passed by the primary settling tanks and thus it has higher concentration of solid suspension than the wastewater from the primary settling tanks.

For high process performance in the aeration tanks, the organic material should be well mixed in the mixing tank and equally distributed to the effluent pipes, which transport wastewater from the mixing tank to the aeration tanks. In the following, the geometry of the mixing tank is represented in detail.

5.1 Details of the Studied Mixing Tank

The studied geometry is shown in Figure 5. Two-phase flow with low dispersed phase volume fraction flows from the primary settling tank into the mixing tank through the duct. The flow with higher dispersed phase volume fraction has passed by the primary settling tank and it flows through the by-pass pipe into the mixing tank. In the mixing tank, two flows are mixed and the effluent from the mixing tank is equally distributed to the effluent pipes 1 - 4.

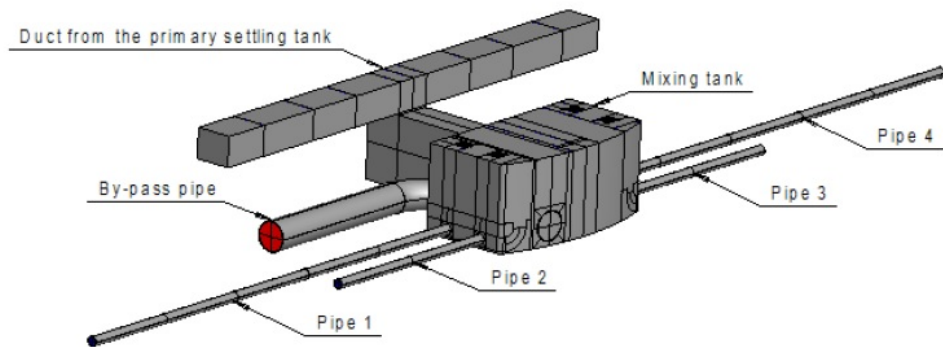


Figure 5. Geometry of the mixing tank.

5.1.1 Estimation of the Pipe Entrance Lengths

Before the geometry of the model can be constructed with the GAMBIT software, the entrance lengths, l_e , of the pipes need to be estimated. The estimation is done by the following equation, which is valid for turbulent flows [52].

$$\frac{l_e}{d_H} = 4.4Re^{\frac{1}{6}} \quad (127)$$

The hydraulic diameter, d_H , is calculated as

$$d_H = \frac{4A}{P}, \quad (128)$$

where P is the perimeter of the pipe or duct.

When the entrance length is considered, the model can be constructed so that the flow will be fully developed before it enters the mixing tank. Similarly, the flow will be fully developed at the studied outlets.

Because the estimated entrance lengths have so large values (Table 2), and the aim is to keep the meshed geometry as small as possible so that the simulations would not take too much time, the flow is not fully developed before the mixing tank (the flow is hardly fully developed in reality either because of pipe bends). Two of the effluent pipes (pipes 1 and 4 in Figure 5) are constructed to be 25 meters long and another two of the effluent pipes (pipes 2 and 3) are only 10 meters long, because the elbows at that point are left out of this study. Thus, the flow should be fully developed at the outlets of the effluent pipes 1 and 4.

Although in the present work the most interesting part of the geometry is the mixing tank, the effluent pipes are constructed to be quite long, because it is assumed that flow is heterogeneous and thus it would be interesting to study particle transport also in the long straight pipes. The dimensions of the studied geometry are shown in Table 3 and Figure 6.

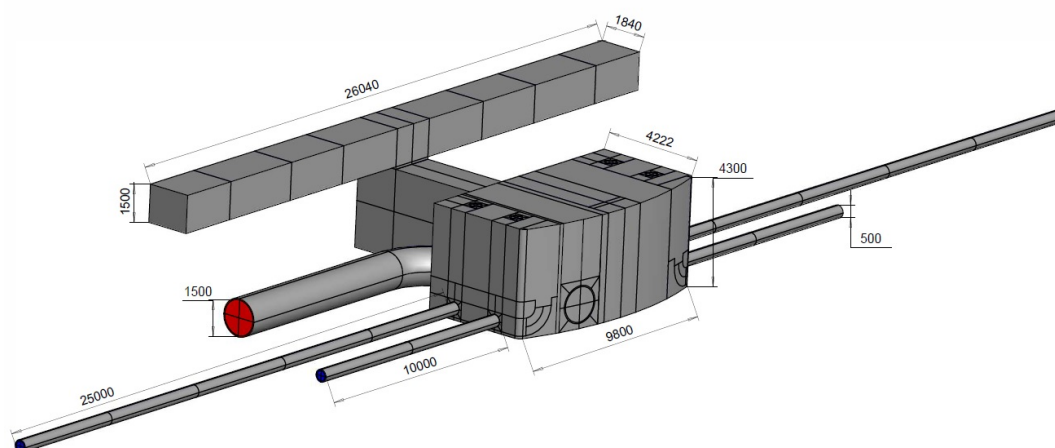
Table 2. The estimated entrance lengths.

	l_e [m]
Duct from the primary settling tank	60.4
By-pass pipe	56.6
Effluent pipes	22.0

As the literature review shows, there are few studies on liquid-solid flow in industrial scale, but any information about this particular case cannot be found. Slurry transport is studied in horizontal pipelines in laboratory scale but not in complex large-scale geometries with multiple inlets and outlets. In the present work, the total volume of the studied geometry is 363 m³, which is approximately 700 times larger than the laboratory scale ones studied in literature. He et al. [22] and Goula et al. [27] studied two-phase flow in industrial scale, but their research was concerned

Table 3. The dimensions of the studied geometry.

	d_H [m]	A [m ²]	l [m]
Inlet from the primary settling tank	1.88	3.75	
Duct from the primary settling tank	1.65	2.76	26.04
Duct to the mixing tank	2.41	6.44	5.20
Opening on the mixing tank wall	1.84	3.39	
By-pass pipe	1.50	1.77	15.00
Effluent pipes 1 and 4	0.50	0.20	25.00
Effluent pipes 2 and 3	0.50	0.20	10.00

**Figure 6.** The dimensions of the geometry.

with sedimentation — not mixing, and Goula et al. limited their study to 2D model. In addition, both studies were performed with the Eulerian-Lagrangian approach. In general, more research is done on sedimentation and mixing in stirred tanks than mixing in the tank described in this thesis.

5.1.2 Modified Shape of the Mixing Tank

The shape of the mixing tank in wastewater treatment plants is generally rectangular. A closer look on Figure 5 shows that in the present work the back wall of the mixing tank is curved. Two corners of the tank are rectangular while two of them

are rounded. For flow it is easier to follow curved path whereas in sharp-edged rectangular corners recirculating regions are generated. In two-phase flow, particles are gathered in these recirculating regions, which make the mixing process inefficient and can increase erosion.

5.2 Computational Mesh

The smaller and simpler the studied geometry, the easier the meshing and modeling. However, in the present work a complex large-scale mixing tank of the wastewater treatment process is studied. The complex geometry with multiple inlets and outlets makes the generation of the mesh difficult. In the following, the generation process of the mesh is described, the recommended procedure for the estimation of the discretization error is introduced, and the results of the mesh independence test are represented.

5.2.1 How to Create High Quality Mesh in Complex Industrial Scale Geometry?

In the present work, the mesh independence test consists of three meshes. The meshes are called as coarse, medium, and fine mesh, depending on the total number of computational cells the mesh includes. The mesh used in pipes is similar as the mesh described in literature by many authors, for example [38, 51, 67]. The mesh structure is called as O-type mesh by Zhang et al. [67]. Close to the wall the mesh is refined to capture the big gradients in the boundary layer and in the middle of the pipe hexahedral mesh is used as shown in Figure 7.

After the first test simulation, the boundary layer height was estimated, and it was observed that the mesh in the boundary layer does not need to be so dense. Thus, the boundary layer mesh was coarsened so that the observed values of the dimensionless normal distance, y^+ , show that the first computational cell is in the log layer. It is

important that the first computational cell is in the log layer ($y^+ > 30$ and $y < 0.1\delta$), because the law of the wall holds in the log layer, and the wall function approach can only be used if the law of the wall is valid. The results of the meshes used in the pipes and ducts are shown in Figures 7 and 8 below, and the analysis of the dimensionless normal distance, y^+ , for the coarse mesh is shown in Table 4. More information about the meshes is given later in this chapter. In the table, the values of y^+ are observed in the by-pass pipe before the 90-degree bend. The height of the first computational cell was increased from the value of 1 mm to 10 mm.

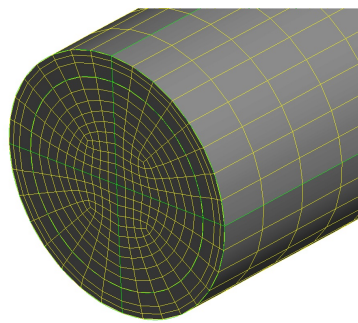


Figure 7. Mesh of the pipe.

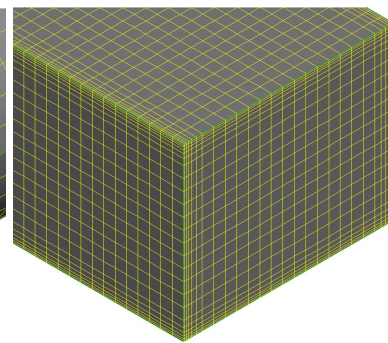


Figure 8. Mesh of the duct.

Table 4. The analysis of the dimensionless normal distance, y^+ .

		Eq.	
u	[m/s]		0.364
$0.99u$	[m/s]		0.360
τ_w	[N/m ²]		0.196
u_τ	[m/s]	(84)	0.014
δ	[m]		0.202
log layer	[mm]		$2.8 < y < 20.2$
log layer	[-]	(83)	$30 < y^+ < 216$

One problem arose while meshing the studied geometry. Where pipes and the mixing tank wall are connected, there is formed a region, which is difficult to be meshed with high quality hexahedral computational cells. This region and the first mesh are shown in Figure 9. In literature, the problem was solved using the multiblock-structured-unstructured hybrid mesh (Dufresne et al. [23] and Majid et al. [68]).

The structured hexahedral mesh was used wherever possible and the unstructured mesh with tetrahedral and prism elements was used at the pipe entrance regions. However, this kind of unstructured mesh has poor quality.

Because the high quality hexahedral mesh can be applied to the shapes of cube or cylinder easily, the geometry in the pipe entrance regions was modified by dividing the mixing tank into smaller parts. In the case of one inlet and outlet, the continuation of the pipe inside the tank would be simple way to avoid meshing problems in the pipe entrance region. In this thesis, there are multiple inlets and outlets, which makes the situation more complex. The solution is to take advantage of 90-degree pipe bends. The cylindrical pipe geometry is continued inside the tank so that the walls of the pipes are referred to as interior zones in GAMBIT software. After the modification, good quality hexahedral mesh can be applied. The modified pipe entrance region is shown in Figures 10 and 11.

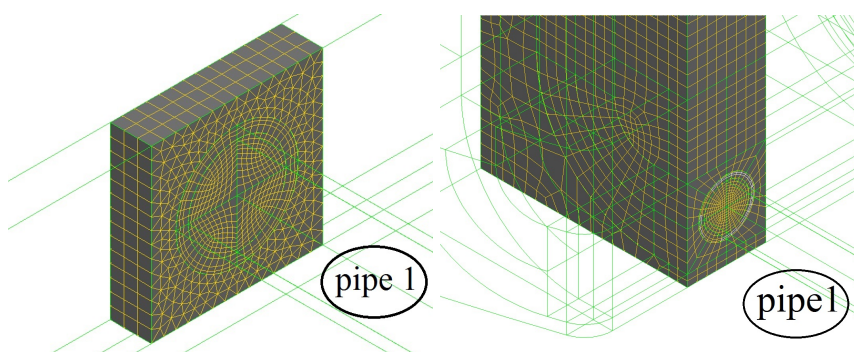


Figure 9. Mesh of the pipe entrance region.

Figure 10. Mesh of the modified pipe entrance region.

To evaluate the mesh, there are numerous quality metrics that can be computed. The following quality metrics are used to evaluate the meshes: minimum orthogonal quality, maximum aspect ratio, and maximum skewness. The optimum value is 1 for the orthogonal quality, 1 for the aspect ratio, and 0 for the skewness. The information about the studied meshes is shown in Table 5. The skewness of the meshes is studied more closely in Figure 12. Notice, that the most of the cells have excellent quality (skewness 0 - 0.1) and only a few cells have the maximum skewness.

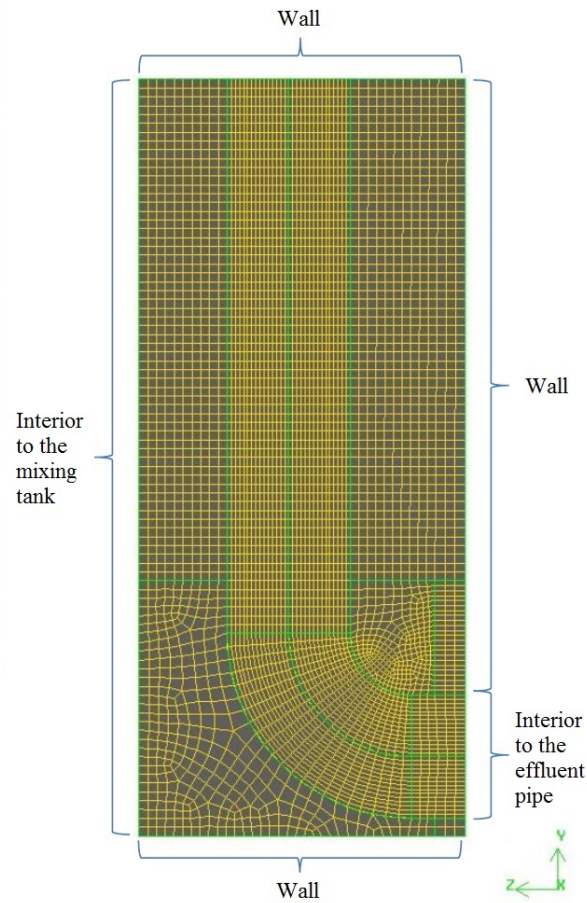


Figure 11. Mesh of the modified pipe entrance region and the boundary types.

However, in the evaluation of the mesh, the physics of the flow to be computed should also be taken into account, because the quality of the mesh does not depend only on the geometrical features of the flow, but on the flow conditions as well. The used mesh influences on the spatial discretization error. The error due to the discretization is studied in the following chapter. [69, 70]

Table 5. The information about the studied meshes.

	number of cells	minimum orthogonal quality	maximum aspect ratio	maximum skewness
Coarse	1 026 869	0.71	39.60	0.51
Medium	3 779 219	0.71	19.48	0.51
Fine	10 383 231	0.71	7.79	0.51

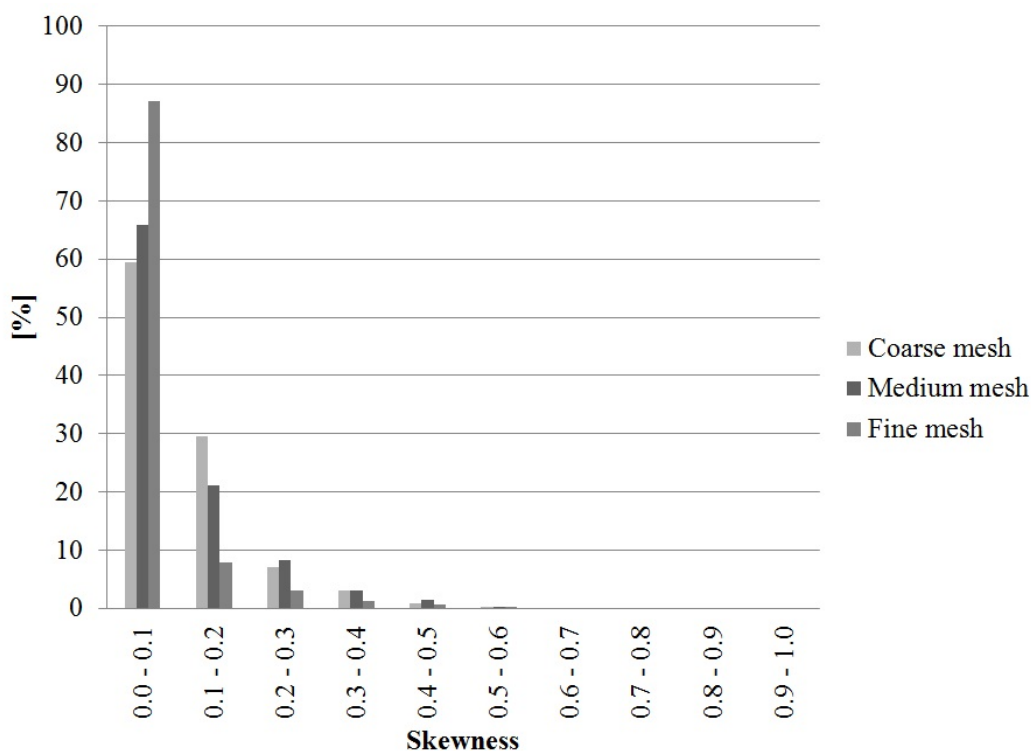


Figure 12. Skewness of the meshes.

5.2.2 Numerical Uncertainty

Numerical uncertainty results from the influence of discretization and iterative convergence errors. The spatial discretization error is due to the grid size and the time discretization error is due to the time step. Numerical uncertainty cannot be eliminated, but it can be minimized and the bounds of the numerical uncertainty can be estimated. [71]

Numerical uncertainty can be quantified by varying grid resolution, numerical schemes, models and model inputs [71]. According to Roache [72], the systematic grid-convergence studies are the most common, most straightforward, and most reliable technique for the quantification of numerical uncertainty. The quantification of uncertainty requires multiple grid generations. Roache says that it is not necessary to double the total number of computational cells, non-integer grid refinement and coarsening are economical alternatives.

Before any estimation of the discretization error is calculated, it must be shown that iterative convergence is achieved at least three (preferably four) orders of magnitude decrease in the normalized residuals for each equation solved. Currently the most reliable method available for the prediction of numerical uncertainty is the Richardson extrapolation method. The Grid Convergence Method (GCI), which is based on the Richardson extrapolation method, is an acceptable and recommended method that has been evaluated over several hundred CFD cases, according to the article in Journal of Fluids Engineering in 2008 [73].

Based on the same article mentioned above [73], the recommended procedure for the estimation of the discretization error is introduced in the following.

1. Select three significantly different sets of meshes, which have the total numbers of computational cells, N_1 , N_2 , and N_3 , respectively.
2. Define the representative mesh size, h , which is defined for three-dimensional case as

$$h = \left[\frac{1}{N} \sum_{i=1}^N (\Delta V_i) \right]^{\frac{1}{3}} \quad (129)$$

and for two-dimensional case as

$$h = \left[\frac{1}{N} \sum_{i=1}^N (\Delta A_i) \right]^{\frac{1}{2}}, \quad (130)$$

where ΔV_i represents the volume of the i^{th} cell, ΔA_i the area of the i^{th} cell, and N the total number of the cells, respectively.

3. Define the mesh refinement factor, r

$$r = \frac{h_{\text{coarse}}}{h_{\text{fine}}}. \quad (131)$$

For example, let's denote that $N_1 > N_2 > N_3$. Then $h_1 < h_2 < h_3$, and

$$r_{21} = \frac{h_2}{h_1} \quad (132)$$

$$r_{32} = \frac{h_3}{h_2}. \quad (133)$$

Based on experience, it is recommended that the refinement factor is greater than 1.3.

4. Calculate the value of p :

$$p = \frac{1}{\ln(r_{21})} \left| \ln \left| \frac{\varepsilon_{32}}{\varepsilon_{21}} \right| + \ln \left(\frac{r_{21}^p - s}{r_{32}^p - s} \right) \right| \quad (134)$$

$$s = 1 \operatorname{sgn} \left(\frac{\varepsilon_{32}}{\varepsilon_{21}} \right) \quad (135)$$

$$\varepsilon_{21} = \phi_2 - \phi_1 \quad (136)$$

$$\varepsilon_{32} = \phi_3 - \phi_2, \quad (137)$$

where ϕ_k is the solution of the studied variable of the k^{th} mesh. The equation of p can be solved using fixed-point iteration. Negative values of $\varepsilon_{32}/\varepsilon_{21}$ are an indication of oscillatory convergence.

5. Calculate the extrapolated values from

$$\phi_{\text{ext}}^{21} = \frac{r_{21}^p \phi_1 - \phi_2}{r_{21}^p - 1} \quad (138)$$

$$\phi_{\text{ext}}^{32} = \frac{r_{32}^p \phi_2 - \phi_3}{r_{32}^p - 1}. \quad (139)$$

6. Calculate and report the following error estimates.

$$e_a^{21} = \left| \frac{\phi_1 - \phi_2}{\phi_1} \right| \quad (140)$$

$$e_{\text{ext}}^{21} = \left| \frac{\phi_{\text{ext}}^{21} - \phi_1}{\phi_{\text{ext}}^{21}} \right| \quad (141)$$

$$GCI_{\text{fine}}^{21} = \frac{1.25 e_a^{21}}{r_{21}^p - 1} \quad (142)$$

When computed profiles of the studied variable are represented, it is recommended that the value of GCI_{fine} is used to indicate numerical uncertainty by error bars on the profile, analogous to the experimental uncertainty. [73]

In this thesis the experimental data is not available. Thus, the estimation of the numerical uncertainty is done using the procedure described above.

5.2.3 Mesh Independence Test

The mesh independence test consists of three meshes introduced in Chapter 5.2.1. In Figure 13, the values of velocity at the outlets of the effluent pipes are shown.

The error bars due to the numerical uncertainty are shown in Figure 13 for coarse and medium meshes. The error bars of the medium mesh are same size as the data points. They are calculated using the procedure described above in Chapter 5.2.2. Figure shows that there is no significant difference in the results between medium and fine meshes. The difference between the results calculated by coarse and medium meshes is 0.40 % and between the results calculated by medium and fine meshes only 0.01 %. As a conclusion, there is no mesh dependence in the results. Because the medium mesh needs less computational effort than the fine mesh, the medium mesh is chosen for the next simulations.

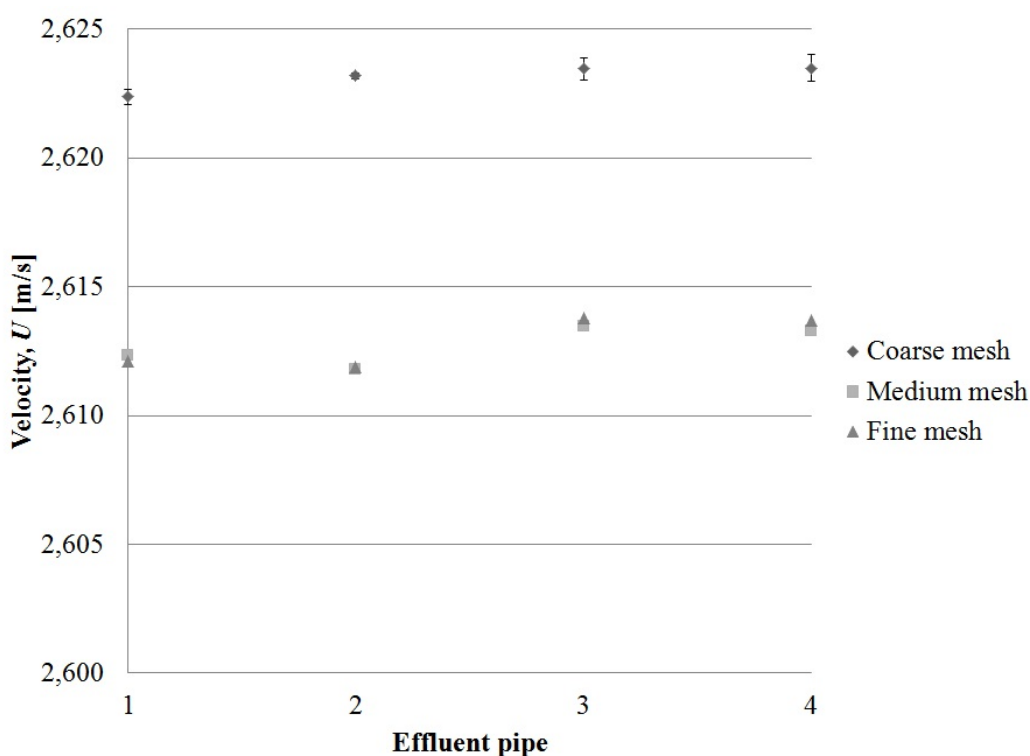


Figure 13. The effect of the mesh on the values of velocity.

5.3 Selected Boundary Conditions and Initial Values

The conservation equations must be solved together with appropriate boundary conditions [8]. In this thesis, the mass flow inlet boundary condition is used at the inlets because the mass flow rate is set to a constant value. The aim is that the flow is equally distributed between the effluent pipes. Because the value of pressure at the

outlets is not known, the pressure outlet boundary condition cannot be used. Instead of the pressure outlet, the outflow boundary condition is used. The boundary types of the studied geometry are shown in Figure 14.

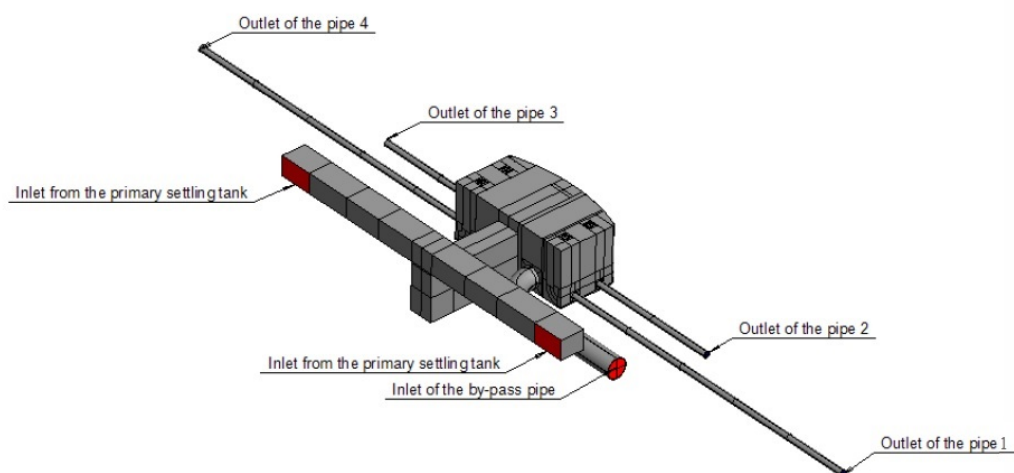


Figure 14. Boundary types.

During the simulations it was noticed that it is difficult to achieve a converged solution with the Eulerian model if the outflow boundary condition is used at the outlets. Thus, the boundary condition was changed from the outflow to pressure outlet in the case of the Eulerian model. The values of static pressure at the outlets were found from the converged solution calculated by the mixture model. The pressure outlet boundary condition sets the value of static pressure at the outlets to a constant value and the value of mass flow rate is modified to meet the specified static pressure. Because the difference in mass flow rate at the outlets was less than 0.5 % when the pressure outlet boundary condition was used instead of the outflow boundary condition, the results calculated by these two outlet boundary conditions are comparable.

The usage of the pressure outlet boundary condition instead of the outflow boundary condition does not only ease the convergence but it also speeds up the calculation. The computational time required by different models and boundary conditions is represented in Chapter 5.6.

5.3.1 Boundary Conditions in the Eulerian-Lagrangian Approach

For the particles tracked through the computational domain in the discrete phase model, there are four different boundary conditions: escape, reflect, trap, and bed shear stress. First three of the boundary conditions are available in the commercial software Fluent, but the last one can be used as a user defined function [74].

If the boundary condition of the particle is set to "escape", the particle is reported as having escaped when it encounters the boundary. This boundary condition is used at inlets and outlets. "Reflect" means that the particle rebounds off the boundary with a change in its momentum as defined by the coefficient of restitution. The reflect boundary condition is used at vertical walls, where particles do not settle to the wall. If the boundary condition called "trap" is used, the calculation is terminated when the particle reaches the boundary. This boundary condition takes the settlement of the particles into account. The "bed shear stress" boundary condition is often used when the combined sewer overflow (CSO) tanks are considered. When the value of the local shear stress is below the critical value, the particle reaching the boundary is trapped. When the value of the local shear stress is above the critical value, the particle is reflected. The difficulty in this boundary condition is that the selection of the critical value of the shear stress is crucial. [23, 25, 74]

In the present work, it is firstly assumed that no sedimentation occurs in the mixing tank corresponding to "reflect" boundary condition on every wall. However, the effect of the "trap" boundary condition on the results is also studied and the results are compared.

For the wall, the no-slip boundary condition can be specified. It demands that the velocity component tangential to the wall must be the tangential velocity of the wall. Hence, if the wall does not move, then the tangential velocity of the fluid is zero at the surface of the wall. For surface roughness, the typical value is used, which for commercial steel is 0.045 mm according to Munson et al. [52].

At the inlets, the turbulence intensity, I , is estimated according to Tarpagkou and Pantokratoras [25].

$$I = 0.16Re^{-\frac{1}{8}} \quad (143)$$

The boundary conditions for the inlets are shown in Table 6. The boundary conditions of the two inlets from the primary settling tank are equal.

Table 6. The boundary conditions at the inlets.

	q_m [kg/s]	α_d [-]	Re [-]	I [%]
Inlet from the primary settling tank	715	$1 \cdot 10^{-4}$	$2.7 \cdot 10^5$	3.3
Inlet of the by-pass pipe	611	$3 \cdot 10^{-4}$	$4.0 \cdot 10^5$	3.2

5.3.2 Typical Values for Particle Density and Concentration in Wastewater Treatment Process

According to literature, the density of suspended solids varies between the values of 950 and 1200 kg/m³ after the preliminary treatment of the influent [75]. The particle size varies from the value of 0.2 mm to 6 mm and above depending on the screen size used in the wastewater treatment plant [3]. The concentration of suspended solids after the primary settlement process ranges from 30 to 175 mg/l [5], while the concentration of wastewater, which has by-passed the primary settling tanks, ranges from 100 to 350 mg/l [76].

The material properties and initial values of the dispersed phase are chosen according to the values described above. The starting value for dispersed phase density used in the simulations is the average of the values 950 and 1200 kg/m³, that is 1075 kg/m³. Later, other values in the range of 950 - 1075 kg/m³ are studied, too. The value of particle diameter used in this thesis is 3.75 mm, which is the average of the values of 1.5 and 6 mm when the fine screen is used in the wastewater treatment plant. The value of concentration of suspended solids after the primary

settlement is chosen to be the average value of 102.5 mg/l. The value of concentration of wastewater, which has by-passed the primary settling tanks is chosen to be the average value of all wastewater treatment plants in Finland [77], 315 mg/l, which is in the range of the values described above. The properties of solids phase used in this thesis are shown in Table 7.

It is assumed that temperature of incoming water is 10°C (which is the average value of incoming wastewater temperature in Finland, [78]), thus the value of water density is 999.7 kg/m³ and the value of kinematic viscosity is $1.308 \cdot 10^{-6}$ m²/s.

Because for the studied values of volume fraction the Stokes number gets small values (< 1), particles will follow the continuous flow closely. Also, from Equation (9) the slip ratio (the ratio of the dispersed phase velocity to that of the continuous phase) can be calculated. For all studied cases the value is 1, thus the velocity of the dispersed phase equals to that of the continuous phase, and particles follow the continuous phase flow closely. When the velocity of the dispersed phase equals to that of the continuous phase, the relative (or slip) velocity is zero. In that case, the relative Reynolds number (Equation (20)) is also zero. If the relative velocity is neglected, the mixture model is reduced to homogeneous multiphase model. The differences of the mixture (or drift flux) and homogeneous multiphase model are studied in this thesis.

Table 7. The properties of the dispersed phase.

	Concentration [mg/l]		Density [kg/m ³]	Diameter [mm]
	After primary settlement	By-pass		
Case 1	102.5	315	1075.0	3.75
Case 2	102.5	315	1017.0	3.75
Case 3	102.5	315	1005.0	3.75
Case 4	102.5	315	999.7	3.75
Case 5	102.5	315	950.0	3.75

5.4 Ways to Couple Pressure and Velocity in Two-Phase Flows

Pressure-velocity coupling is required to enforce mass conservation and to obtain the pressure field. It can be done in either a segregated or coupled manner. The segregated algorithm solves the momentum equation and pressure correction equations separately. It is memory efficient, but the solution convergence is relatively slow. The coupled algorithm solves the momentum and continuity equations together. It requires more memory than the segregated algorithm, but it improves the rate of convergence.

ANSYS Fluent provides four segregated types of algorithms and three coupled types of algorithms to couple pressure and velocity. The segregated algorithms are SIMPLE (Semi-Implicit Method for Pressure-Linked Equations), SIMPLER (SIMPLE-Consistent), PISO (Pressure Implicit with Splitting of Operators) and FSM (Fractional Step Method). The FSM algorithm is available when using the Non-Iterative Time Advancement scheme (NITA) in the calculation of unsteady flows. The coupled algorithms which are applicable when using the Eulerian multiphase model in ANSYS Fluent are the Coupled algorithm, Coupled with volume fractions, and PC-SIMPLE (Phase Coupled SIMPLE). The Coupled algorithm works efficiently in steady calculations, the Coupled with volume fractions algorithm may have some drawbacks in robustness and computational time usage, and the PC-SIMPLE is an extension of the SIMPLE algorithm to multiphase flows. The algorithms are listed in Table 8. The table also shows for which multiphase models the algorithms are applicable. [19]

Because this thesis considers steady state problems and the NITA scheme is not applicable with the discrete phase model, the FSM algorithm is not used. The pressure and velocity are coupled using the Coupled algorithm, because it improves the rate of convergence and it is applicable for all models used in this thesis. Thus, there will be no difference in the results generated by the different pressure-velocity coupling algorithms.

Table 8. The algorithms for pressure-velocity coupling.

	VOF	Mixture		Eulerian
		Homogeneous	Drift-flux	
SIMPLE	✓	✓	✓	
SIMPLEC	✓	✓	✓	
PISO	✓	✓	✓	
Coupled	✓	✓	✓	✓
Coupled with volume fractions	✓	✓		✓
PC-SIMPLE				✓

5.5 Convergence Criteria

In the present work the converged solution is found by observing both the values of scaled residuals and the monitors of important parameters, which are the values of velocity, static pressure, and dispersed phase volume fraction at the outlets of effluent pipes, mass imbalance, and the contour plots of dispersed phase volume fraction in the duct and by-pass pipe. In the case of the discrete phase model, also the number on incomplete particle trajectories is observed.

The converged solution is achieved when there is at least three orders of magnitude decrease in the normalized residuals for each equation solved. In addition, there must not be change in neither the residuals nor the studied parameters.

5.6 Computational Time

The information about the computational time and memory requirement is crucial in the case of choosing the multiphase model for simulation purposes.

The calculations are performed using two computers, Dell T5600 and Camp. The former one contains 12 processor cores and 32 GB memory, and the latter one contains 4 cores and 16 GB memory. ANSYS Fluent software uses only one processor

core. The requirement of RAM (Random Access Memory) is proportional to both the mesh size and the computational model. One rule of thumb is that 1 million computational cells require 1 GB RAM memory. This is valid only for single-precision solver.

As a result of the mesh independence test, the medium mesh, which consists of 3.8 million computational cells, was chosen for the simulations. However, it was found that the computers did not have enough memory to calculate the Eulerian model with medium mesh. The error log of ANSYS Fluent "Failed to allocate memory" indicates that there is not enough memory available for the simulation. The limit is approximately 3.2 million computational cells for Dell T5600 and 1.6 million cells for Camp. As a conclusion, for double-precision solver and Eulerian multiphase model, another rule of thumb is that 1 million cells require 10 GB RAM memory. Thus, the new mesh consisting of 3.0 million computational cells, was created.

The share of total available memory (Dell T5600) used by the different models is shown in Table 9. Table shows that the Eulerian model requires more computational effort than the mixture model and the new medium mesh uses the most of the total available memory. The combination of the medium mesh and the Eulerian model exceeds the memory capacity available in the computer Dell T5600. The simulations are performed using the double-precision solver, except when the fine mesh is used.

Table 9. Memory usage of different models.

Mesh	Single-phase flow	Two-phase flow			Eulerian
		DPM	Mixture		
			Homogeneous	Drift-flux	
	[%]	[%]	[%]	[%]	[%]
Coarse	18	-	-	28	57
New medium	31	-	36	42	74
Medium	40	41	-	49	-
Fine	61	-	-	-	-

Table 10 shows how much more time the denser mesh requires per iteration compared to the coarse mesh, when the calculation is performed using the computer with 32 GB RAM memory. It should be noticed, that the double-precision option is used for coarse, new medium, and medium meshes, whereas the single-precision option is used for fine mesh because of the available memory capacity. The increase in computational time is directly proportional to the increase in the number of computational cells.

Table 10. Computational time required by different meshes compared to time required by coarse mesh.

Mesh	Relative time [-]
Coarse	1.00
New medium	2.95
Medium	3.82
Fine	8.99

Table 11 shows how much more time the more complicated model requires per iteration compared to the modeling of single-phase flow, when the calculation is performed using the computer with 32 GB RAM memory, double-precision option, and medium mesh. The computational time required by Eulerian model is estimated, when it is known that the medium mesh requires 3.82 times more time per iteration compared to the coarse mesh according to Table 10.

Table 11. Computational time required by different models compared to time required by single-phase case.

Model	Relative time [-]
Single-phase flow	1.00
Discrete phase	1.03
Homogeneous multiphase	1.07
Drift-flux	1.33
Eulerian	8.84

However, studies made by Zhang and Chen [28] show that when a sufficient number

of the particles is tracked, the Eulerian-Lagrangian approach requires more computational time than the Eulerian-Eulerian approach. In the present work, the sufficient number of the particles for the statistically stable solution is analyzed. This analysis shows that the increase in the number of tracked particles has no influence on results. The only difference is that the dispersed phase volume fraction field looks less scattered when the number of particles is increased. It was found that the increase in the number of particles increase the computational time. Zhang and Chen studied particle concentration distributions in ventilated enclosed spaces and according to them the number of particles should be larger than the number of mesh elements to ensure a statistical stability.

In the case of the Eulerian model, it was noticed that the outflow boundary condition causes divergence in the solution. Thus, the boundary condition at the outlets of the effluent pipes was changed from the outflow to the pressure outlet. Pressure outlet boundary condition enables to find a converged solution and the computational time required by iteration is 12 times less than when outflow boundary condition is used.

6 RESULTS AND DISCUSSION

Firstly, this chapter represents the effects of turbulence models on the results. Secondly, the influences of boundary conditions, particle density, and particle size on the results are studied. The analysis of the particle density includes the study of the effect of secondary flows on particles. Then, the differences between multiphase models and turbulent dispersion models are represented. Also the strengths and weaknesses of different multiphase models are discussed. Then, the pressure losses in two-phase flow are calculated and finally the developed computational tool is introduced.

6.1 Difference Between Turbulence Models

Because all turbulence models offer advantages and disadvantages over others in certain applications, no single turbulence model can be judged to be the optimum model in all circumstances [6]. Thus, the difference between turbulence models is studied in this chapter. The observed turbulence models are the standard $k - \varepsilon$, Renormalization Group (RNG) $k - \varepsilon$, realizable $k - \varepsilon$, standard $k - \omega$, Shear-Stress Transition (SST) $k - \omega$, and Reynolds Stress Model (RSM). The choosing of the turbulence model is important, especially when the Eulerian-Lagrangian approach is used, because the direction of the velocity vectors has an influence on the particle trajectories.

When the fluid changes its direction for example in the pipe bend, it experiences an adverse pressure gradient. Because of the viscous effects, the fluid does not have enough momentum to overcome the adverse pressure gradient and separation occurs. In addition to adverse pressure gradient in the streamwise direction, there is a pressure gradient acting radially because of the centripetal forces. In curved ducts and pipes, secondary flows are mainly generated by these centripetal forces, but they can also be generated by the anisotropy in the Reynolds stresses. [52]

Because secondary flows and boundary layer separation affect the particle trajectories, they are studied in the following in conjunction with the turbulence models.

6.1.1 Secondary Flows

According to Speziale et al. [79], the turbulence structure of flows in the ducts and pipes can be altered significantly by secondary flows. To balance the centrifugal force on the fluid due to its curved trajectory, there must be a pressure gradient across the pipe. This pressure gradient generates the centripetal force, which is equal and opposite to centrifugal force. Due to viscosity, the fluid near the top and bottom walls of the pipe moves more slowly than that in the middle of the pipe

and therefore requires a smaller pressure gradient to balance its centrifugal force. Consequently, a secondary flow occurs in which the fluid near the top and bottom walls of the pipe moves from the outer side towards the center of the curvature and the fluid in the middle of the pipe moves from the inner side outwards. Due to the secondary flow, the position of the maximum axial flow velocity is shifted towards the outer wall of the pipe from the pipe centerline. [80,81]

In straight ducts and pipes, secondary flows are not generated by centripetal forces but by the anisotropy in the Reynolds stresses. Also in the curved pipes with weak curvature ratios (the ratio of the radius of the curvature to the pipe radius, R_0), the Reynolds stress differences play a crucial role in generating secondary flows. Consequently, two-equation models based on the Boussinesq approximation are incapable of predicting secondary flows in straight ducts and pipes and in the ducts and pipes with weak curvature ratios. However, two-equation models have yielded reasonably acceptable predictions for fully-developed secondary flows in curved ducts and pipes with moderate to strong curvature ratios. [79]

Also the forcing on the flow by particles distributed non-uniformly in the cross-section can generate secondary flows. In a turbulent flow, particles can generate changes in turbulence, which in the case of non-uniformly distributed particles, results in an anisotropy in the Reynolds stresses in the cross-section, which generates secondary flows. [82]

The strength of the secondary flow is characterized by the Dean number, De ,

$$De = \frac{Re}{R_0}, \quad (144)$$

where Re is the Reynolds number and R_0 the curvature ratio [83]. With increasing Dean number the maximum axial flow velocity moves towards the outer wall of the pipe bend from the pipe centerline [84].

When the velocity fields in the by-pass pipe before (position a in Figure 15) and after (position b in Figure 15) the bend are observed, it can be concluded that there are no significant secondary flows generated by anisotropy in Reynolds stresses

because the results of realizable $k - \varepsilon$ and Reynolds stress model are equal and we are observing the pipe with strong curvature ratio ($R_0 = 3$). In Figure 15, the flow direction in the by-pass pipe is shown by red arrow, the positions where the secondary flows are observed are shown by green circles, and the effluent pipes are numbered from 1 to 4. The velocity fields before the bend are shown in Figure 16, and after the bend in Figure 17. The only difference between the realizable $k - \varepsilon$ and Reynolds stress models occurs after the pipe bend where the recirculating region is located. In straight effluent pipes, there is no significant difference between the turbulence models either.

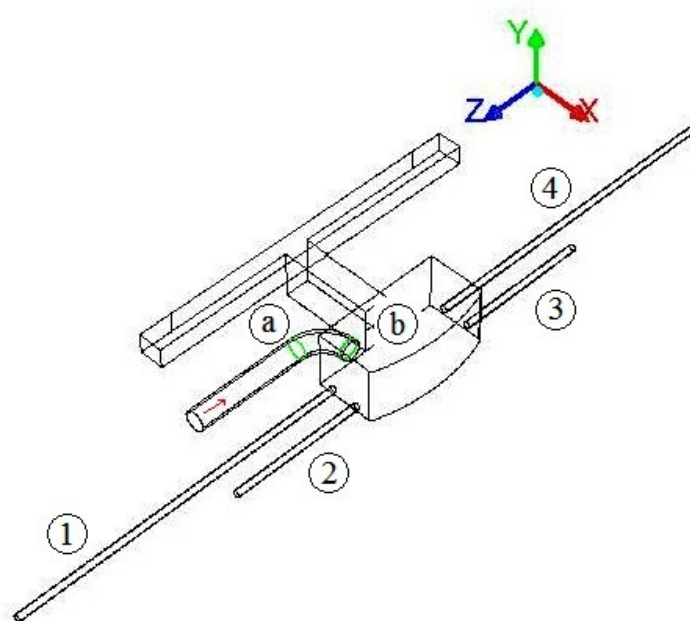


Figure 15. The positions where the secondary flows are observed. a) before the bend b) after the bend

In Figures 16 and 17, the directions of secondary flows generated by centripetal forces in the vicinity of the pipe bend are marked with arrows. Likewise in the study of Jayanti et al. [85], in a 90-degree bend a relatively weak, double-vortex secondary flow is formed, and it grows stronger as the bend angle increases. The flow directs from the inner side to the outer side of the bend in major part of the core, and reverses direction close to the wall. The effect of the secondary flows on particles is studied in Chapter 6.3.

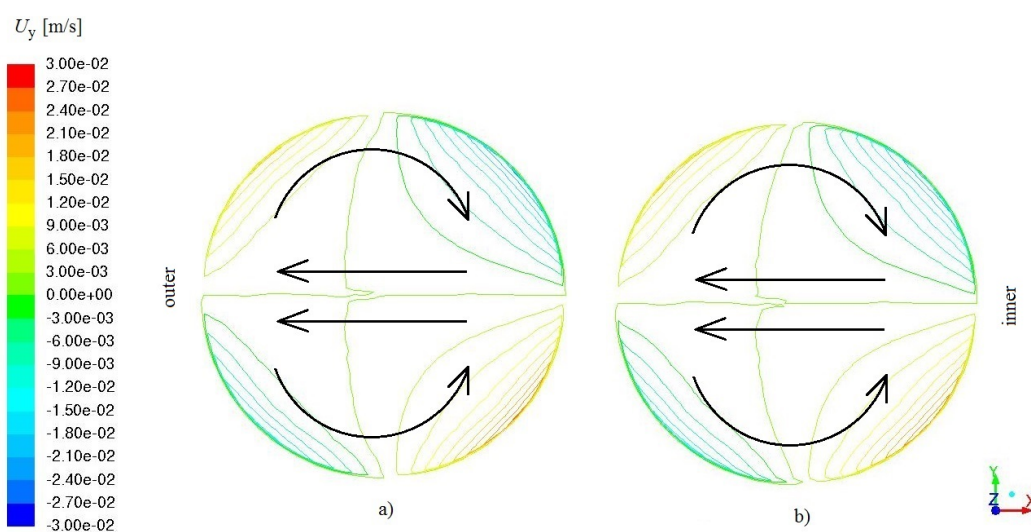


Figure 16. Secondary flow in the cross-section of the by-pass pipe before the bend. a) Realizable $k - \varepsilon$ b) RSM

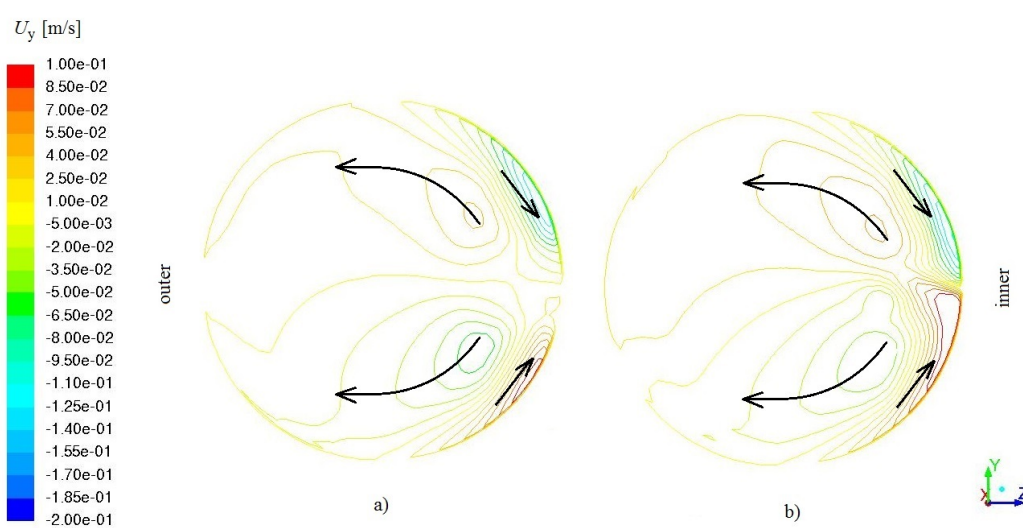


Figure 17. Secondary flow in the cross-section of the by-pass pipe after the bend. a) Realizable $k - \varepsilon$ b) RSM

6.1.2 Boundary Layer Separation

In addition to secondary flows, boundary layer separation has also an influence on particle trajectories. The reattachment length in the case of recirculating region is used here to compare the turbulence models. In the studied geometry, recirculating regions are located for example after the inlets of the duct, after the elbow in the

by-pass pipe, before the opening into the mixing tank, and inside the mixing tank. Generally, recirculating regions are located where the direction of the main flow changes.

The reattachment length can be found by plotting the values of wall shear stress, τ_w . The values of wall shear stress are observed along the front wall of the duct, which leads wastewater from the primary settling tank to the mixing tank. The values calculated by six turbulence models are shown in Figure 18. The separation occurs where the wall shear stress gets the first nonzero value at the edge of the inlet. The reattachment occurs when the wall shear stress gets the value of zero.

The separation region can be seen in Figures 19 and 20, where the contours of velocity in the direction of the z coordinate are shown in the left hand side and in the right hand side of the duct, respectively. In Figure 19, the influent flows to the positive direction of the z coordinate. The separation region is the blue region where the direction of the flow is to the negative direction of the z coordinate. On the contrary, in Figure 20 the influent flows to the negative direction of the z coordinate and thus the values of velocity are negative. Now, the separation region is the red region where the direction of the flow is to the positive direction of the z coordinate. In both figures, the edge of the inlet where the separation occurs, is marked with black line.

In the case of slurries, it is important that the turbulence is modeled in the most accurate way, because the particles tend to get caught up into the turbulent eddies and recirculating regions. Also the influence of the particles on the flow field should be taken properly into account. Figure 21 shows that all studied turbulence models predict that particles attenuate turbulence, when the particle size is 3.75 mm and particle density 1075 kg/m^3 . The grey, vertical lines in figure show the values for the dispersed phase volume fraction, which are $1 \cdot 10^{-4}$ for wastewater from the primary settling tanks and $3 \cdot 10^{-4}$ for overflow wastewater.

However, as discussed in Chapter 4.8, there is no generally accepted model to take

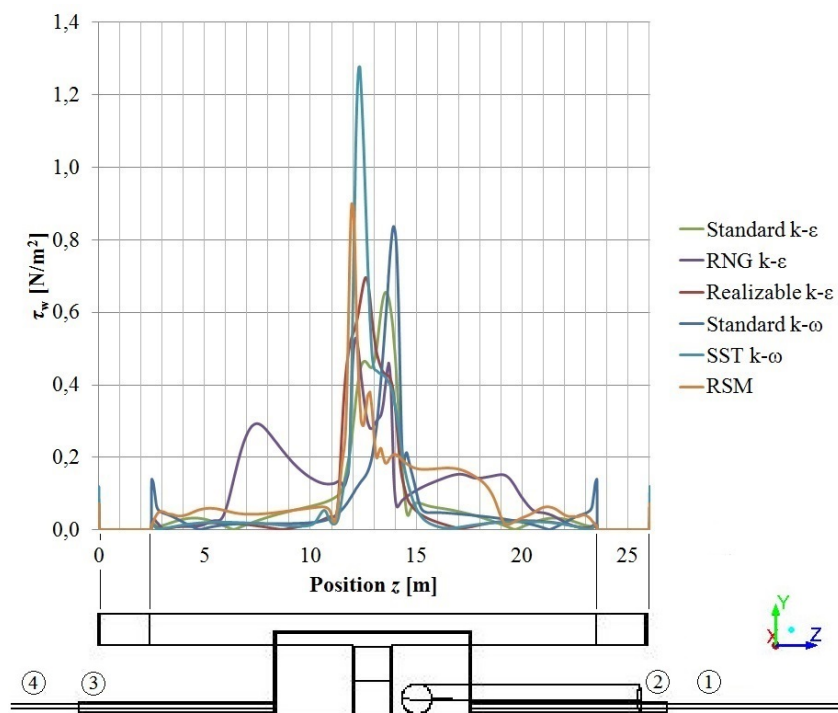


Figure 18. The values of wall shear stress along the front wall of the duct from the primary settling tank calculated by different turbulence models.

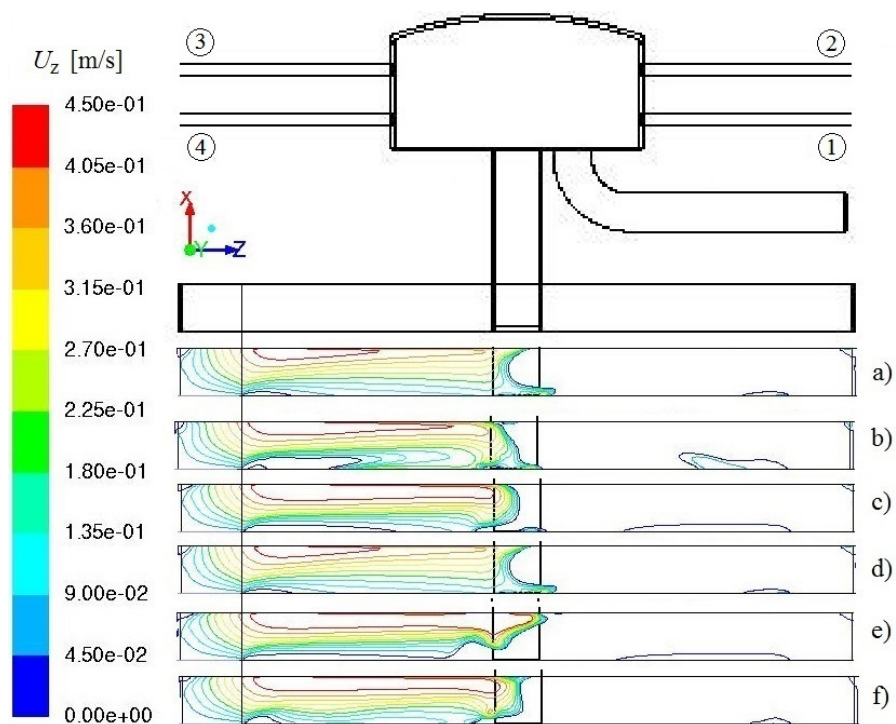


Figure 19. The contour plots of velocity in the left hand side of the duct. a) Standard $k - \epsilon$ b) RNG $k - \epsilon$ c) Realizable $k - \epsilon$ d) Standard $k - \omega$ e) SST $k - \omega$ f) RSM

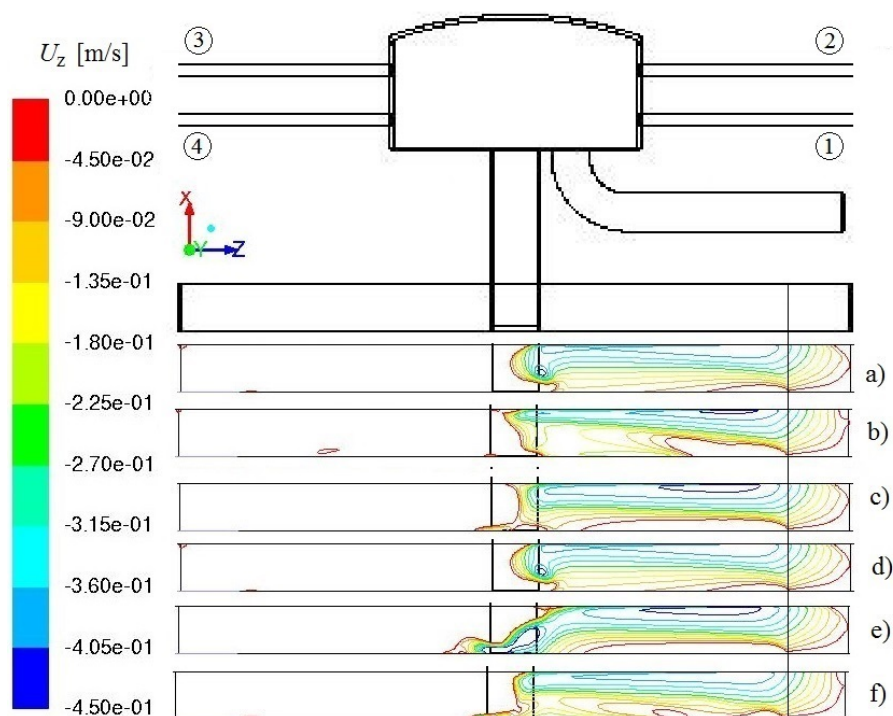


Figure 20. The contour plots of velocity in the right hand side of the duct. a) Standard $k - \varepsilon$ b) RNG $k - \varepsilon$ c) Realizable $k - \varepsilon$ d) Standard $k - \omega$ e) SST $k - \omega$ f) RSM

the effect of particles on the continuous phase turbulence into account. In ANSYS Fluent, the effect of particles on the continuous phase turbulence can only be taken into account in the discrete phase model. Thus, the attenuation of turbulence by particles cannot be validated in this thesis by studying turbulence modulation with all multiphase models.

It should be noted that Kolmogorov time scale is inversely proportional to turbulence dissipation rate. Thus, near the walls where turbulence dissipation rate gets larger values, Kolmogorov time scale gets smaller values and if the ratio between particle response time and Kolmogorov time scale gets a value greater than 100, the particles augment turbulence. On the contrary, far from the walls where turbulence dissipation rate gets smaller values, Kolmogorov time scale gets larger values and if the ratio between particle response time and Kolmogorov time scale gets a value smaller than 100, the particles attenuate turbulence. The influence of the particles on turbulence is thus dependent on the location with respect to the wall surface. However, when the particles are small enough, they may get trapped in the

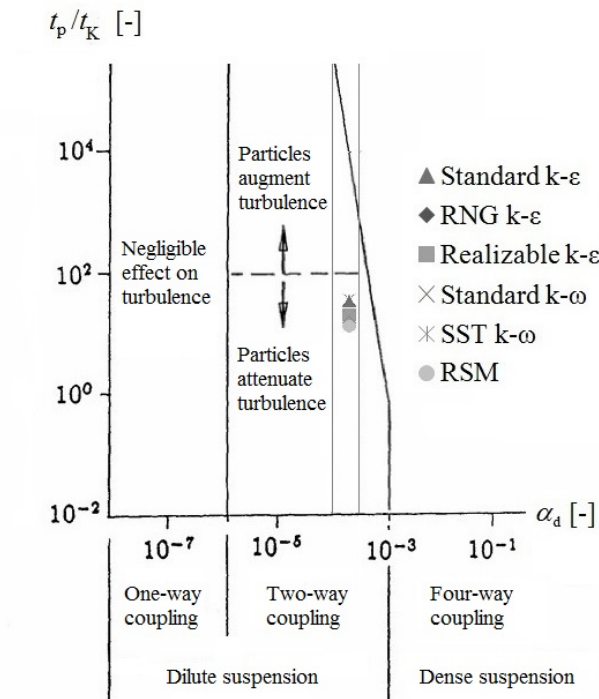


Figure 21. The map of regimes of interaction between particles and turbulence. Modified from [54].

viscous sublayer, where the turbulent eddies are not able to pick them to the main stream [56].

In this thesis, there is no experimental data available for comparison. According to literature review, the realizable $k - \varepsilon$ and SST $k - \omega$ models should the most accurately predict the flow with adverse pressure gradients and separation. Results represented in Figures 18-20 show that those models give approximately equal results for the reattachment length. The results given by the RNG $k - \varepsilon$ model differ from the results of other turbulence models. It also slightly underestimates turbulence kinetic energy and turbulence dissipation rate in the mixing tank. Because of the results and the knowledge that the RNG $k - \varepsilon$ model is more appropriate for swirling flows, it is left outside of the following simulation cases. Also the standard $k - \varepsilon$, standard $k - \omega$, and Reynolds Stress model underestimate the reattachment length compared to the realizable $k - \varepsilon$ and SST $k - \omega$ models. The standard $k - \varepsilon$ and standard $k - \omega$ models overestimate turbulence kinetic energy in pipe entrance regions compared to other models as the contour plots of turbulence kinetic energy

in Figure 22 show, but overall there is no significant discrepancies between studied turbulence models.

The realizable $k - \varepsilon$ model is preferred to instead of the SST $k - \omega$ model because the computational time of the SST $k - \omega$ model is 1.2 times the computational time used by the realizable $k - \varepsilon$ model and the realizable $k - \varepsilon$ model also enhances numerical stability. The aim is to achieve converged solution and the available time for simulations is limited. Since there is no experimental data available for comparison, the realizable $k - \varepsilon$ model is chosen for following simulations because it neither overestimates nor underestimates the observed turbulence quantities compared to other models.

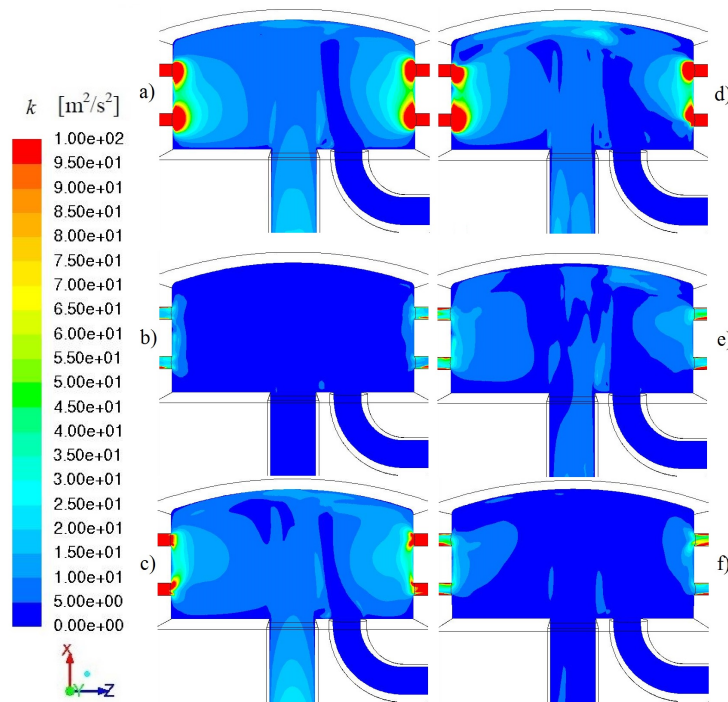


Figure 22. The contours of turbulence kinetic energy. a) Standard $k - \varepsilon$ b) RNG $k - \varepsilon$ c) Realizable $k - \varepsilon$ d) Standard $k - \omega$ e) SST $k - \omega$ f) RSM

6.2 Effect of Boundary Conditions

In ANSYS Fluent, the discrete phase model allows to choose between three boundary conditions. Those are escape, reflect, and trap, as represented in Chapter 5.3.

The "escape" boundary condition is used at the outlets, but the effect of "reflect" and "trap" boundary conditions on results needs to be studied.

Firstly, the case 1 (in Table 7) with the value of 1075 kg/m^3 of particle density is studied. When two-phase flow is modeled using the discrete phase model and the reflect boundary condition is applied for every wall, almost every tracked particle is reported as "incomplete". It means that the trajectory calculation is abandoned because the maximum number of iteration steps is exceeded. The particle may have been caught in a recirculating region of the continuous phase flow field.

In the case of particles having the value of density of 1075 kg/m^3 , the large number of "incomplete" particle trajectories does not mean that the maximum number of iteration steps is too low, but it means that reflect boundary condition is not appropriate in the case where the particles tend to settle on the floor. This was found when the trap boundary condition was applied on the floors of the duct and mixing tank, and also on the bottom of the pipes. After the trap boundary condition was applied, the number of incomplete particle trajectories reduces to value of zero and every tracked particle is reported being trapped.

There is one drawback when using the trap boundary condition. Because trap boundary condition terminates the trajectory calculation when the particle reaches the boundary, the saltation or moving bed regimes cannot be modeled with boundary conditions available in ANSYS Fluent. Also the trap boundary condition applied on the bottom of the effluent pipes causes that none of the tracked particles escapes from the outlets even when the particle density gets lower values.

After simulations done using the values of 999.7, 1005, 1017, and 1075 kg/m^3 for particle density and varying boundary conditions between reflect and trap, the results show that in the case where the particles tend to deposit, the use of trap boundary condition is crucial. In the cases, where the particle density gets values above the critical value (the value of particle density above which the deposition occurs), the reflect boundary condition is recommended in the effluent pipes, because

in there the values of velocity are above the deposition velocity, and if particles are being trapped because of the trap boundary condition, none of the tracked particles escapes from the outlets.

A conclusion about the effect of boundary conditions is that the boundary condition is dependent on the physics of the flow and there is no boundary condition which can be applied in every case. The deposition velocity of particles can be estimated by Equation (1) and if the free stream velocity of the case exceeds the deposition velocity, the reflect boundary condition should give reliable results.

In the case where deposition velocity approaches free stream velocity, it is recommended to simulate the problem using both the reflect and trap boundary conditions [23]. If sedimentation does not occur, the results should be almost equal.

6.3 Effect of Particle Density

From Equation (1), the deposition velocity can be estimated when the particle density, diameter, and dispersed phase volume fraction are known. Settling particles tend to migrate into the regions where flow velocity is low [56]. When the dispersed phase volume fraction, particle diameter, and free stream velocity are known, the particle density can be estimated so that the deposition velocity will be smaller than the free stream velocity and particles should stay in suspension.

Table 12 shows that when particle density is 1075 kg/m^3 , the deposition velocity exceeds the free stream velocity, which means that sedimentation occurs. Table also shows the limits for dispersed phase volume fraction and particle density. When the values are smaller than the limits, particles should stay in suspension with the given free stream velocity. If the value of free stream velocity decreases, sedimentation may occur. Thus, deposition of particles may begin in the regions of the mixing tank, where velocity has lower values.

Table 12. The effects of particle density and volume fraction on sedimentation. In the duct, particles should stay in suspension if the value of volume fraction were smaller than $3.6 \cdot 10^{-9}$ or if the value of particle density were smaller than 1005.5 kg/m^3 . In the by-pass pipe, particles should stay in suspension if the values were smaller than $1.0 \cdot 10^{-6}$ or 1017.8 kg/m^3 , respectively.

	Density [kg/m^3]	Volume fraction [-]	Deposition velocity [m/s]	Velocity [m/s]
Duct from the primary settling tank	1075.0	$1.0 \cdot 10^{-4}$	0.6803	0.1907
	1075.0	$\leq 3.6 \cdot 10^{-9}$	0.1906	0.1907
	≤ 1005.5	$1.0 \cdot 10^{-4}$	0.1904	0.1907
By-pass pipe	1075.0	$2.9 \cdot 10^{-4}$	0.7001	0.3458
	1075.0	$\leq 1.0 \cdot 10^{-6}$	0.3452	0.3458
	≤ 1017.8	$2.9 \cdot 10^{-4}$	0.3456	0.3458

The effect of particle density is observed in the duct from the primary settling tank, in the by-pass pipe, and in the mixing tank. Figures 23 and 24 show the contour plots of volume fraction in the duct and in the by-pass pipe, respectively. Red color refers to dispersed phase and blue color to continuous phase. Figure 25 shows the particle trajectories when the value of particle density varies in the range of 950 kg/m^3 and 1075 kg/m^3 . The results are calculated with the discrete phase model.

According to Table 12, the particles should settle on the bottom of the by-pass pipe and on the floor of the duct, when the particle density is 1075 kg/m^3 . This can be seen in all three Figures 23 a), 24 a), and 25 a).

When the value of the particle density is 1017 kg/m^3 , deposition should occur in the duct, but not in the pipe, where velocity is higher. Figures 23 b), 24 b), and 25 b) show that in both duct and pipe deposition occurs, but the phenomenon is not as strong as in the previous case. However, the most of the particles settle on the floor of the mixing tank. Deposition of particles occurs because the difference between the deposition and free stream velocity is only 0.1 %, there is numerical uncertainty, and the equation of the deposition velocity includes experimental constant values. Thus, the values in Table 12 are only rough estimations. Despite the uncertainty of

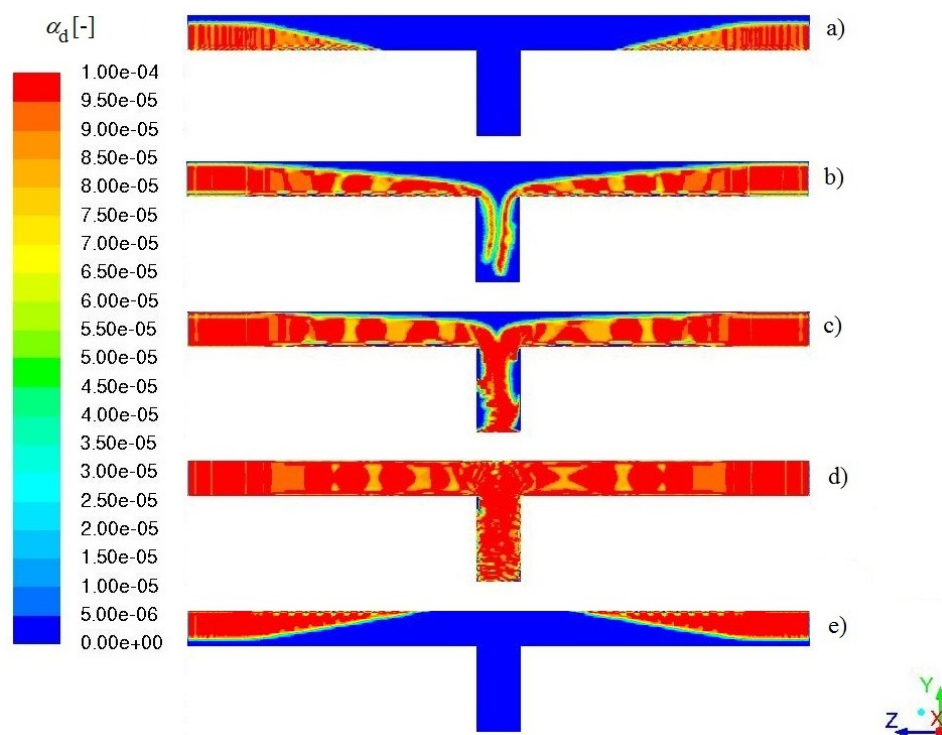


Figure 23. The effect of particle density on volume fraction in the duct from the primary settling tank. a) 1075 kg/m³ b) 1017 kg/m³ c) 1005 kg/m³ d) 999.7 kg/m³ e) 950 kg/m³

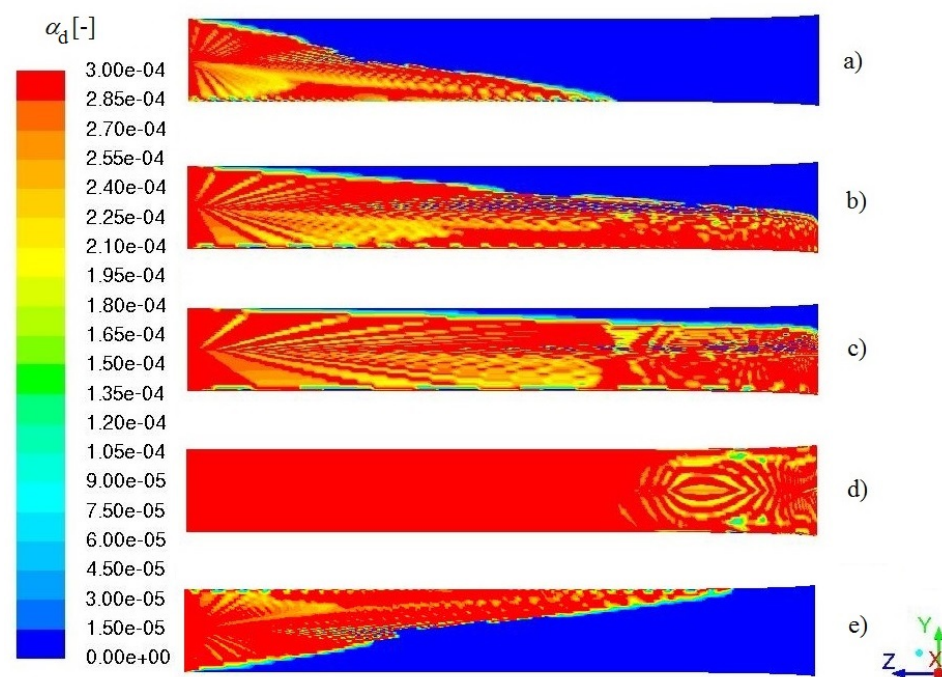


Figure 24. The effect of particle density on volume fraction in the by-pass pipe. a) 1075 kg/m³ b) 1017 kg/m³ c) 1005 kg/m³ d) 999.7 kg/m³ e) 950 kg/m³

the estimated deposition velocity, the results correlate with the theory.

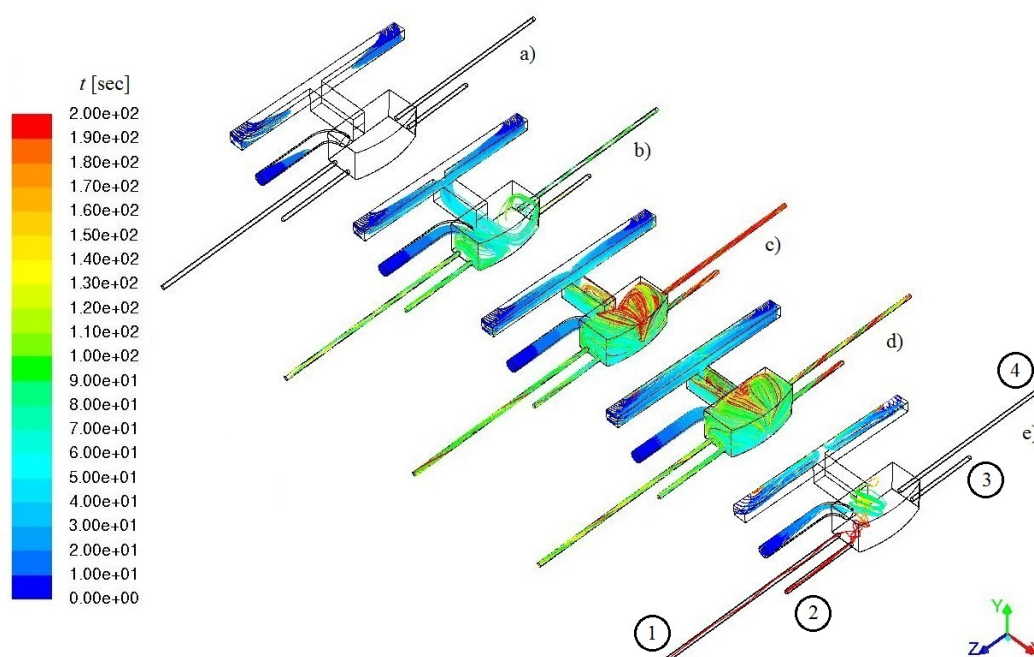


Figure 25. The effect of particle density on particle trajectories, which are colored by particle residence time. a) 1075 kg/m³ b) 1017 kg/m³ c) 1005 kg/m³ d) 999.7 kg/m³ e) 950 kg/m³

If the value of the particle density is decreased even more to the value of 1005 kg/m³, the particles stay better in suspension. The particles even rise near the ceiling of the mixing tank along water, as shown in Figure 25 c). Figures 23 d), 24 d), and 25 d) show the situation in the case where the value of the particle density equals to that of water. Particles do not deposit, but they follow the continuous phase flow field and suspension is homogeneous.

When the value of the density of water exceeds that of the particles, particles float above the water surface as shown in Figures 23 e) and 24 e). From Figure 25 e) can be seen that the particles from the primary settling tank do not flow along the continuous phase into the mixing tank, but they float in the upper part of the duct and the part of them gets caught up in the recirculating regions. In the by-pass pipe, particles rise to the upper part of the pipe and immediately when the particles flow into the mixing tank, they rise to the upper part of the tank. Figure 25 e) shows that some of the particles get caught up in the turbulent eddies and flow into the effluent pipes 1 and 2.

Another index for the estimation of settling tendencies of the particles is the pipe Froude number defined in Equation (103). It is shown in Figure 26 with respect to the material density ratio. The value of the pipe Froude number approaches infinity when the material density ratio approaches unity. When the value of material density ratio is smaller than 1 (that is $\rho_d < \rho_c$), the pipe Froude number gets negative values. Figure indicates that the particles tend to settle in the duct, where the velocity is lower than in the by-pass pipe. In the by-pass pipe, when the material density ratio is 1.005, the inertial forces exceed the gravitational forces and particles stay in suspension. The values of the pipe Froude number below 1 indicate that gravitational forces exceed the inertial forces and particles tend to settle.

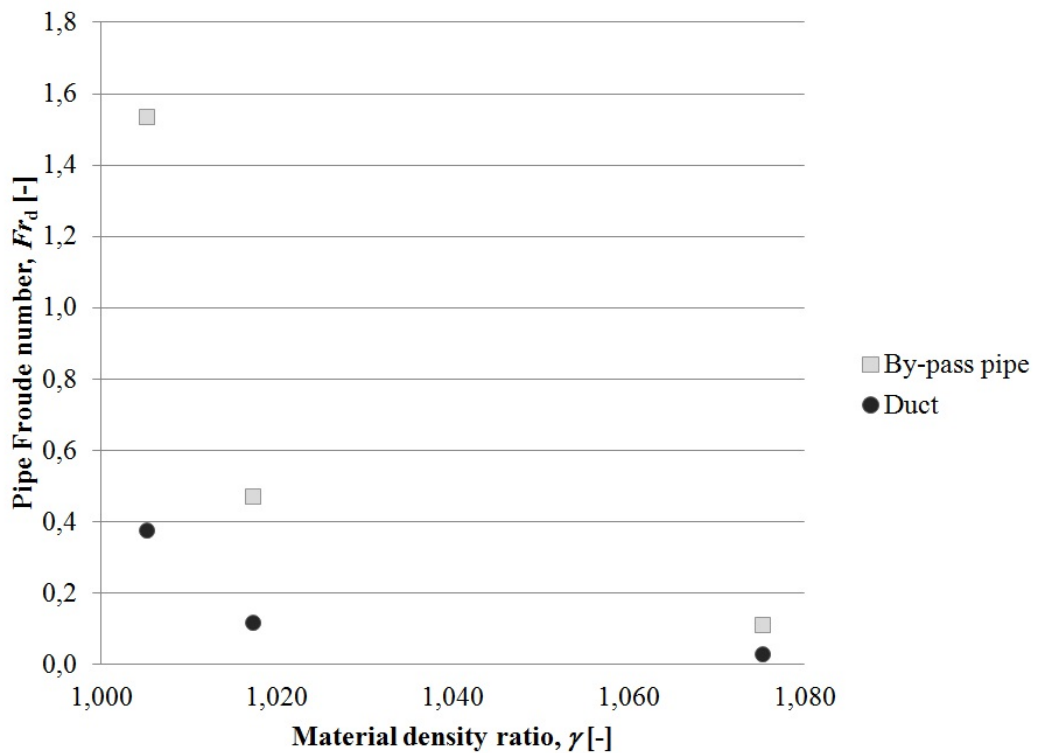


Figure 26. The pipe Froude number with respect to material density ratio.

6.3.1 How Do Secondary Flows Affect Dispersed Phase?

According to Hossain et al. [86], around the pipe bend the maximum deposition of particles does not occur at the bottom of the pipe, but it occurs at 60° skewed to the inner pipe wall because of the centripetal forces in the pipe bend. The skewness

angle depends on the distance from the bend. According to Hossain et al., their numerical investigation showed reasonably qualitative agreement with the experimental results. The similar flow phenomenon is also found in this thesis, when the particle density is 1075 kg/m^3 , as shown in Figure 27.

In Figure 27, the contour plots of volume fraction calculated by the mixture model, which takes slip velocity between the phases into account, are shown in the planes perpendicular to the flow direction. The positions of the planes are shown in Figure 15 by green circles. Before the bend, particles are deposited on the bottom of the pipe, whereas after the bend the maximum deposition of particles occurs on the inner pipe wall. The comparison between Figures 16 a), 17 a) and 27 shows that secondary flows generated by centripetal forces lift particles in the pipe bend from the bottom of the pipe on the inner pipe wall. Compared to the CFD study of Hossain et al. [86], the maximum deposition of particles occurs at 30° rather than 60° skewed to the inner pipe wall.

The difference may result from the studied particle sizes, particle density, position where the values of volume fraction are observed, the curvature ratio of the pipe bend, or turbulence model, which effects on the modeling of the separation region. The particle size studied by Hossain et al. ranges from 2 to $20 \mu\text{m}$ and the particle density is 1640 kg/m^3 . In the present work, the values of volume fraction are observed at the same position as in the cited article. The turbulence model used by Hossain et al. is the Spalart-Allmaras model, which is compared to the SST $k - \omega$ model in the accuracy of prediction of separated flows [87].

Figure 28 shows the contours of dispersed phase volume fraction in the by-pass pipe, which are calculated by the Eulerian model. The Eulerian model predicts that the tendency for particles to settle is stronger than what the drift-flux model predicts in Figure 27 a). The drift-flux model uses mixture properties to solve the continuity and momentum equations. Now, the mixture density almost equals to that of the continuous phase because the dispersed phase volume fraction is relatively low. Thus, the drift-flux model underestimates the particle density, whereas the

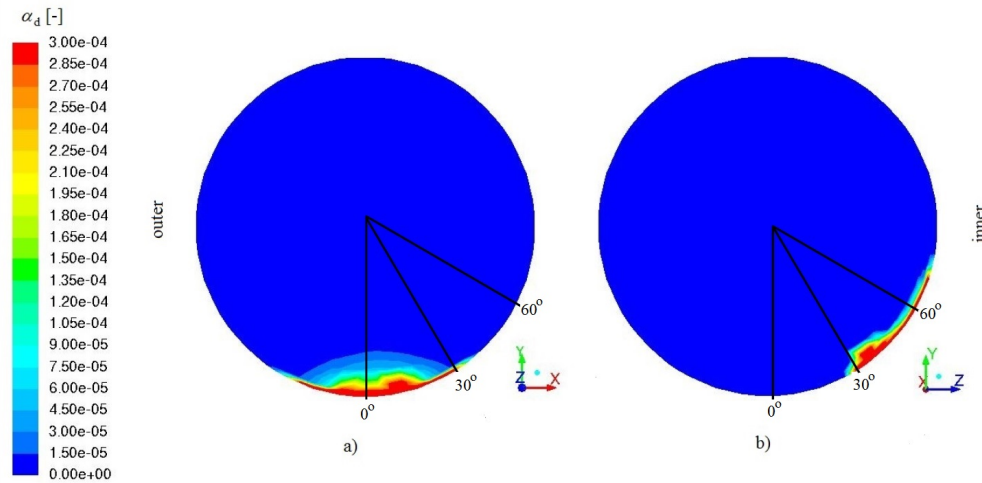


Figure 27. The contours of volume fraction in the by-pass pipe calculated by the drift-flux model.
a) Before the bend b) After the bend

Eulerian model solves the Navier-Stokes equations for both phases and no mixture properties are required. The drift-flux model predicts that the height of the bed of particles is 13 percent of the pipe diameter, whereas the Eulerian model predicts that the height is 11 %. The difference between results is 18 %, but because both models predict that the height of the bed of particles is less than the boundary layer thickness (16 percent of the pipe diameter), secondary flow has similar effect on particles according to both models.

In Figure 27, the results are shown when the particle density is 1075 kg/m^3 and the thickness of the bed of particles is 81 % of the thickness of the boundary layer. In that case, the secondary flow moves from the outer wall towards the inner wall near the bottom of the pipe shifting the bed of particles on the inner wall in the pipe bend. According to the results represented in Figure 49 in Appendix I, when the thickness of the bed of particles is larger than the thickness of the boundary layer, the secondary flow moving from the inner wall towards the outer wall in the major part of the pipe core shifts particles towards the outer wall in the pipe bend. This happens when the particle density gets the value of 999.7, 1005, or 1017 kg/m^3 . However, the secondary flow to reverse direction in the bottom of the pipe shifts particles in the boundary layer towards the inner wall regardless of the particle

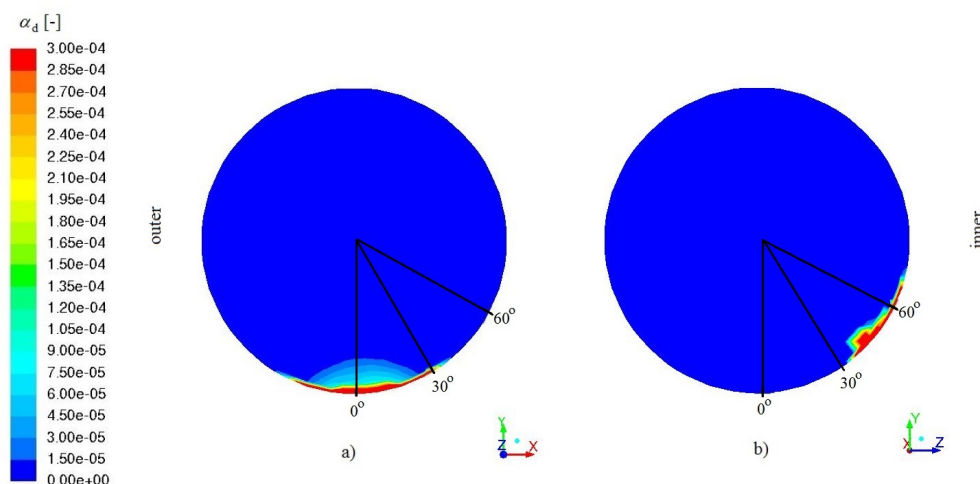


Figure 28. The contours of volume fraction in the by-pass pipe calculated by the Eulerian model.
a) Before the bend b) After the bend

density (Figure 49 in Appendix I).

Figure 49 in Appendix I shows the effect of the secondary flow on particles in the boundary layer and in the middle of the pipe. Because the results are calculated using the discrete phase model, all the particles are trapped on the bottom of the pipe before the pipe bend when the particle density is 1075 kg/m^3 . Thus, in Figure 49 a) there are no particles. Notice, that in Figure 49 e) the secondary flow moving from the outer wall towards the inner wall near the top of the pipe shifts particles towards the inner wall, because the density of the dispersed phase is smaller than that of the continuous phase and the particles are located inside the boundary layer.

6.3.2 How Do Particles Affect Continuous Phase?

The comparison between continuous phase and dispersed phase velocities shows that there is no slip velocity between the phases in the flow direction. Thus, the particles move at the same velocity as the continuous phase. However, in y direction there is a velocity difference between the phases, because gravity has a stronger effect on the dispersed phase. The particles form a moving bed on the bottom of the

pipe, and in the pipe bend the highest concentration of particles is located on the inner pipe wall because of the pressure difference generated by centripetal forces (Figure 29). The direction of centripetal force is marked with an arrow in Figure 29 b). As shown in Figure 30, the maximum value of dispersed phase volume fraction is located where the static pressure is the lowest.

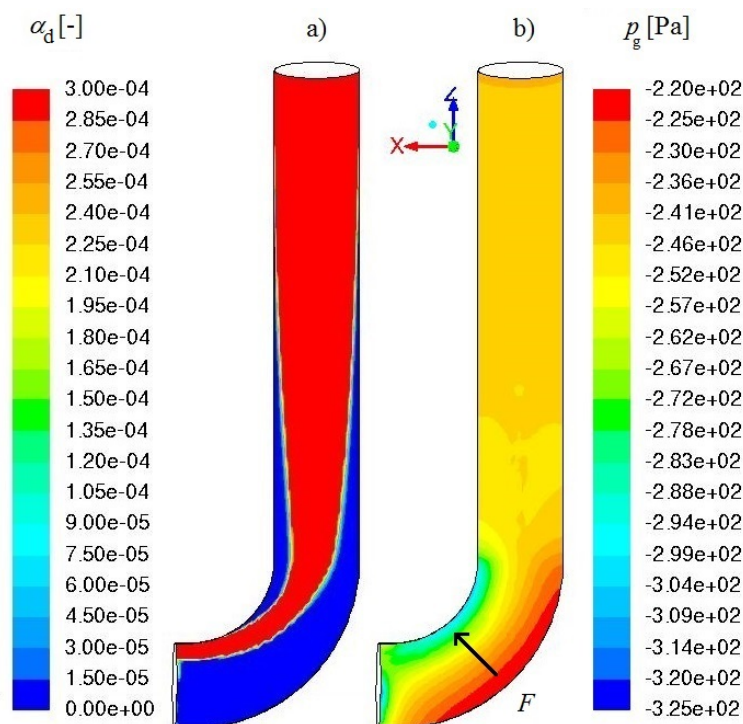


Figure 29. The bottom of the by-pass pipe. a) The contours of volume fraction b) The contours of static pressure

The bed of particles on the bottom of the pipe acts like an increase in surface roughness. The presence of particles increase the value of wall shear stress, which increases drag force and reduces velocity as shown in Figure 31, where the contour plots of velocity are shown for single-phase flow (a) and for two-phase flow (b and c) before the bend of the by-pass pipe. The wall shear stress on the bottom of the pipe is 2.4 times larger in the case of two-phase flow than in the case of single-phase flow. The results in Figure 31 b) are calculated by the drift-flux model and results in Figure 31 c) by the Eulerian model. Figures 31 b) and c) can be compared to Figures 27 a) and 28 a) to see the location of the particles.

The height of the particle bed is 13 percent of the pipe diameter according to the

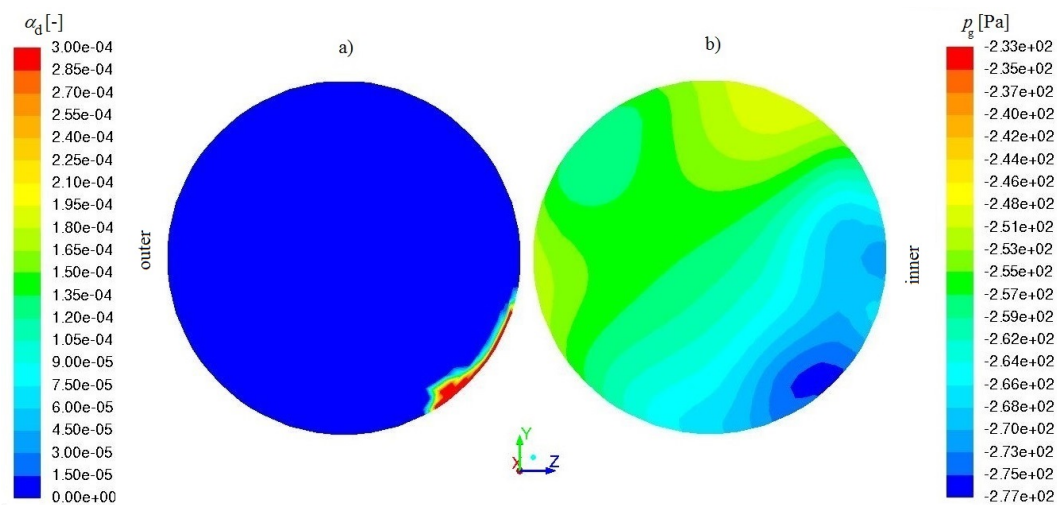


Figure 30. The vertical plane in the by-pass pipe after the bend. a) The contours of volume fraction
b) The contours of static pressure

drift-flux model and 11 percent according to the Eulerian model. Also the velocity profiles of single-phase and two-phase flows before the bend (in Figure 32) show the decrease in velocity because of the particles located on the bottom of the pipe. The drift-flux model predicts that the bed of particles reduces velocity 12 % on average, whereas the Eulerian model predicts that velocity is reduced 30 % on average. The Eulerian model predicts greater reduction in velocity because the drift-flux model underestimates the tendency for particles to settle. The dots in Figure 32 represent the boundary layer thicknesses. The bed of particles increases the boundary layer thickness 23 % from the value of $0.13y/d$ to $0.16y/d$.

The results of Figures 31 b) and c) are calculated by the drift-flux and Eulerian models, respectively. However, the discrete phase model does not show velocity decrease on the bottom of the pipe due to the bed of particles. In the present work, it was noticed that the source terms (calculated from Equation (22)), which take into account two-way coupling between the phases, are so small (of the order of $10^{-11} \dots 10^{-6}$ N) that they have no effect on the velocity field of the continuous phase. According to ANSYS, Inc. [88], the versions older than Fluent 15.0 underestimate two-way turbulence coupling source terms in the discrete phase model by several orders of magnitude. The new version of Fluent software (Release 15.0), released in the end of the year 2013 by ANSYS, Inc., includes a correction to the

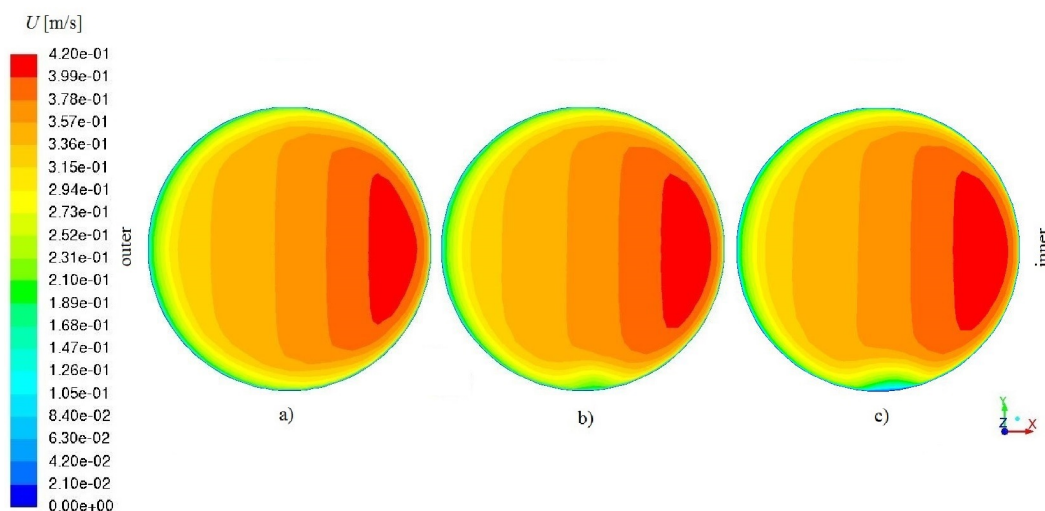


Figure 31. The vertical plane in the by-pass pipe before the bend. a) Single-phase flow b) Two-phase flow (Drift-flux model) c) Two-phase flow (Eulerian model)

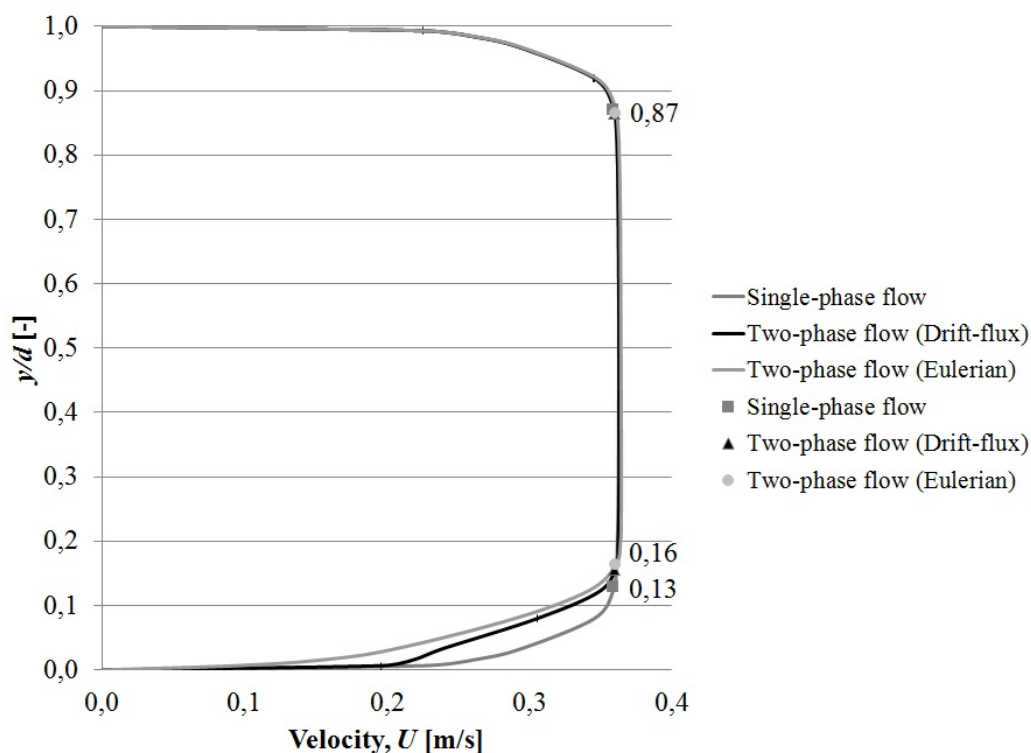


Figure 32. The velocity profile before the bend of the by-pass pipe.

calculation of two-way turbulence coupling source terms [88]. Despite the correction, no decrease in velocity because of the bed of particles on the bottom of the pipe could be observed. This may imply that the coupling between phases is inadequate in the discrete phase model.

The differences between multiphase models are studied more closely in Chapter 6.5.

6.3.3 How Does the Change in Particle Density Affect Erosion?

Erosion can harm pipelines and cause problems in wastewater treatment plants. Especially the pipe bends are exposed to erosion, because in the bends the flow tries to remain its direction, which has an impact on the outer wall of the pipe bend. The results of the present work show that if the suspension of water and particles is either heterogeneous or homogeneous, particles strengthen erosion on the outer wall of the pipe bend. On the contrary, if the particles form a moving bed or saltation regime on the bottom of the pipe such that the thickness of the bed of particles is smaller than the thickness of the boundary layer, particles do not be in touch with the outer wall but with the inner wall of the pipe bend. This is caused by secondary flows generated by centripetal forces in the pipe bends.

If flow rates are remarkably changed in the wastewater treatment process, the flow regime will vary between homogeneous, heterogeneous, saltation, moving bed and even stationary bed regime. Also the position of the most intense erosion is shifted with respect to flow regime. However, the most efficient way to transport slurry is homogeneous or heterogeneous flow. Other flow regimes, where particles deposit on the bottom of the ducts and pipes increase wall shear stress, which increases drag force and pressure drop, and therefore the efficiency of the process is reduced.

6.4 Effect of Particle Size

The regimes of flow can be estimated according to procedure introduced in *Introduction to Practical Fluid Flow* [12]. As represented in Chapter 2, the flow regimes are homogeneous suspension, heterogeneous suspension, saltation, moving bed, and stationary bed. In Figures 33 and 34, the flow regimes are represented

for flow in the duct from the primary settling tank and for flow in the by-pass pipe. The figures differ slightly from each other because the edges of the regimes are dependent on the values of dispersed phase volume fraction and particle density. Now, the particle density is 1075 kg/m^3 in both figures, but the value of volume fraction is $1 \cdot 10^{-4}$ (100 ppm) in the duct and $3 \cdot 10^{-4}$ (300 ppm) in the by-pass pipe.

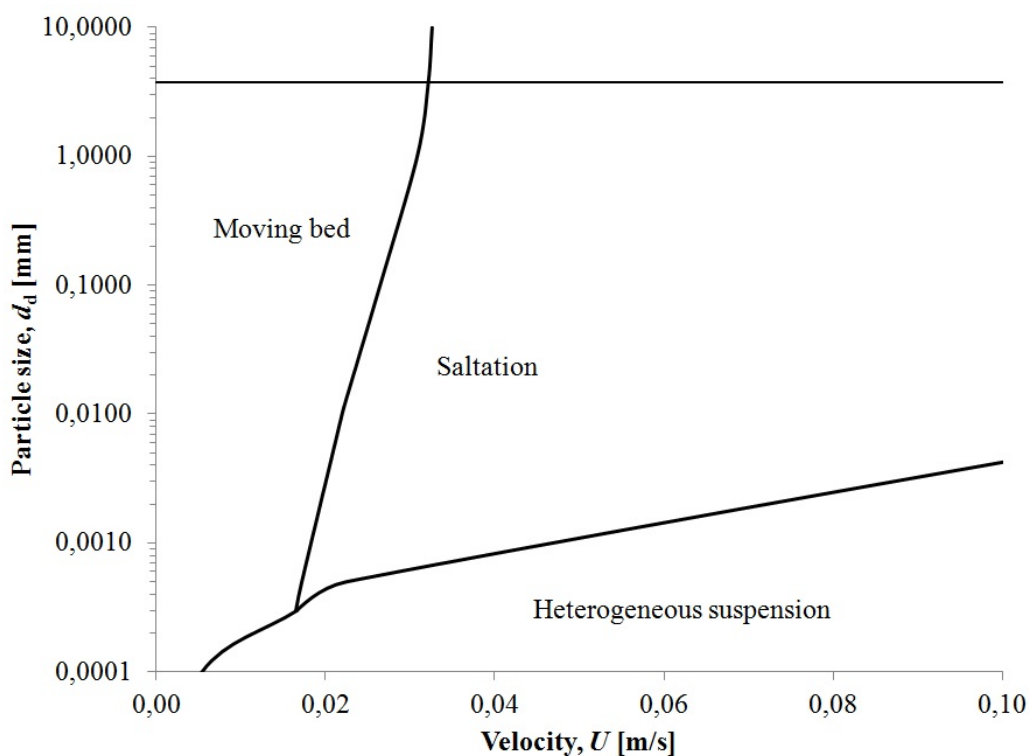


Figure 33. The flow regimes, when the dispersed phase volume fraction is $1 \cdot 10^{-4}$ and particle density is 1075 kg/m^3 .

This kind of figures give a good estimation about the flow regime. The figures show that when the particle size is 3.75 mm (horizontal line in both figures), the flow is in the saltation regime in both the duct and by-pass pipe, because the values of velocity are 0.19 and 0.35 m/s, respectively. This means that the particles settle on the bottom of the duct and pipe, but they are being continually picked up by turbulent eddies and dropped back on the floor in the downstream. This has already been showed in previous chapters. Flow would become heterogeneous in the duct if velocity exceeded the value of 2.1 m/s and in the by-pass pipe if velocity exceeded the value of 2.4 m/s.

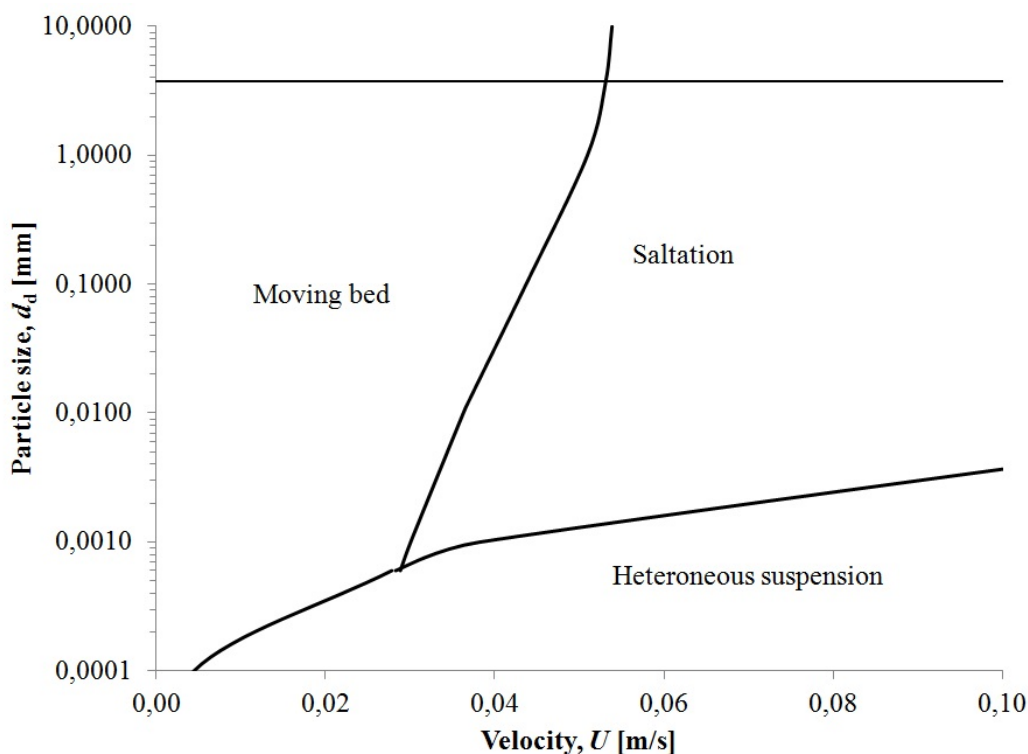


Figure 34. The flow regimes, when the dispersed phase volume fraction is $3 \cdot 10^{-4}$ and particle density is 1075 kg/m^3 .

In practice, it would be impractical to increase velocities to values represented above in the present geometry, because velocity would be almost 27 m/s in the effluent pipes. Therefore, the sizes of pipes and duct should be redesigned to achieve heterogeneous flow efficiently. However, the CFD simulation is performed by increasing the flow rates of influent. The results show that the flow regime approaches heterogeneous, but it is not completely heterogeneous. If velocities were increased even more, the flow would become completely heterogeneous. Now, the pipe Froude number is 5.7 in the by-pass pipe, so that the inertial forces exceed gravitational forces. Gravitational forces affect particles but not so strongly as in the case of lower velocities, when the pipe Froude number was 0.1.

Compared to the case of lower velocities when every incoming particle deposited on the bottom of the duct and pipe, when velocities are increased, 99 % of influent particles flow out of the effluent pipes.

As shown in previous chapter, the discrete phase model is not able to model a moving bed or saltation regime, because the particle trajectory calculation is terminated when the particle reaches the boundary with "trap" boundary condition and thus the dispersed phase cannot form a moving bed or saltation regime. The validity of the discrete phase model depends on the particle density, size, and volume fraction. For particle density of 1075 kg/m^3 , diameter of 3.75 mm, and volume fraction $< 10^{-3}$ (two-way coupling of the phases), the discrete phase model becomes valid when the pipe Froude number $Fr_d \geq 1.0$. This can be seen in Figure 35, where the percentage of the incomplete particle trajectories with respect to the pipe Froude number is shown.

When the value of the pipe Froude number exceeds 1.0, the percentage of incomplete particle trajectories approaches zero. This means that when inertial forces exceed gravitational forces and flow regime changes from the saltation regime to the heterogeneous flow, reflect boundary condition can be used instead of trap, and the discrete phase model is valid. It should be noticed that with particle density of 1075 kg/m^3 and Reynolds number of 400 000 the discrete phase model fails to predict the saltation regime and every incoming particle is incomplete if the trap boundary condition is not used, but when the Reynolds number is increased to value of 3 200 000, flow becomes heterogeneous and the number of incomplete particles approaches zero. Thus, the validity of the discrete phase model depends also on Reynolds number, which determines flow regime. The validity of other multiphase models in the modeling of the saltation regime is studied in the following chapter.

6.5 Difference Between Multiphase Models

The contours of volume fraction in the by-pass pipe calculated by different models are shown in Figure 36. The discrete phase model of ANSYS Fluent is not able to model the saltation and moving bed flow regimes, because the particle trajectory calculation is terminated when the particle reaches the boundary with "trap" boundary condition and thus the dispersed phase cannot form a saltation or moving bed

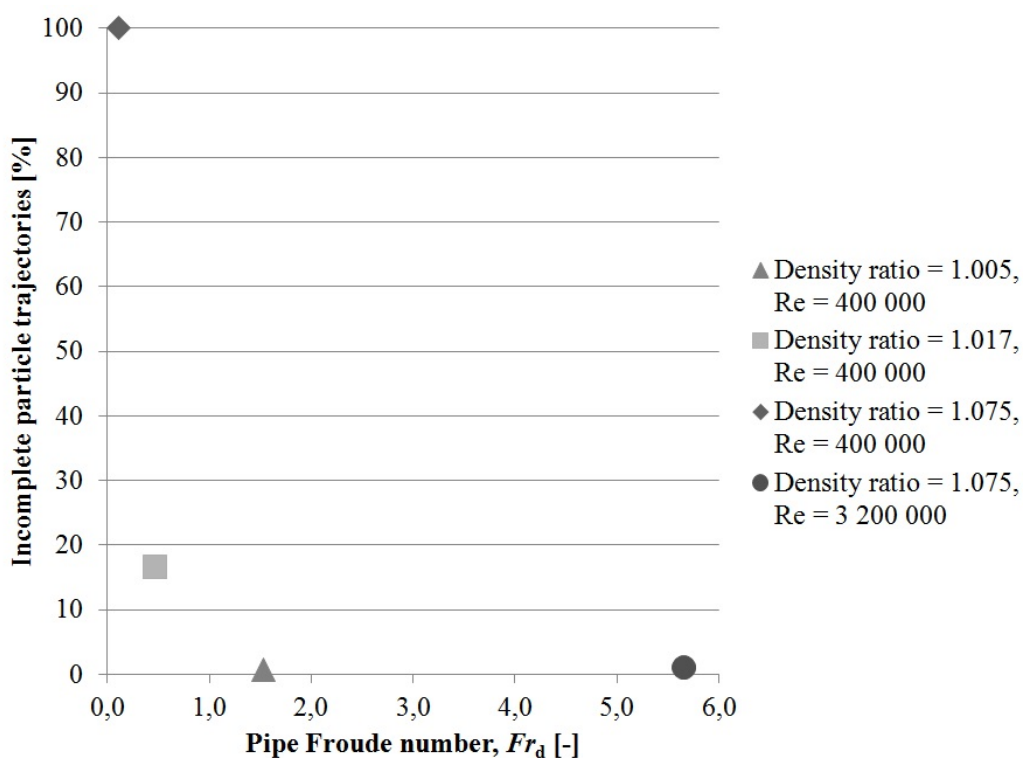


Figure 35. The percentage of the incomplete particle trajectories with respect to the pipe Froude number.

regime. Despite this weakness of the discrete phase model, the contour plots of dispersed phase volume fraction in the duct and by-pass pipe where deposition occurs are identical between the discrete phase, drift-flux, and Eulerian models. It is also found by Zhang and Chen [28] that the Eulerian-Lagrangian and Eulerian-Eulerian approaches have similar accuracy on predicting the particle volume fraction distributions.

In the case of saltation regime, the homogeneous multiphase model is not applicable either. The homogeneous multiphase model is only valid when the mixture can be assumed to be homogeneous, otherwise it gives unrealistic results. Due to the neglect of the slip velocity between the phases, the additional term representing the effect of velocity differences between the phases is neglected in the momentum equation. Therefore, the stratification of the phases cannot be modeled.

When the dispersed phase density is 1075 kg/m^3 and the particle diameter is 3.75

mm, the discrete phase model predicts that every incoming particle deposit on the floors of the duct, by-pass pipe and mixing tank. On the contrary, the homogeneous multiphase model predicts that every particle flows out of the effluent pipes. The drift-flux model, which takes into account the slip velocity between the phases and is able to model the saltation regime, predicts that 11 % of the incoming particles deposit and 89 % flow out of the effluent pipes. The corresponding values for the Eulerian model are 23 % and 77 %. In the Eulerian model, turbulence is modeled by per-phase turbulence model, which solves turbulence equations for both phases. The results are shown in Table 13. In the end of this chapter, it is studied how the dispersed and mixture turbulence models affect the results of the Eulerian model.

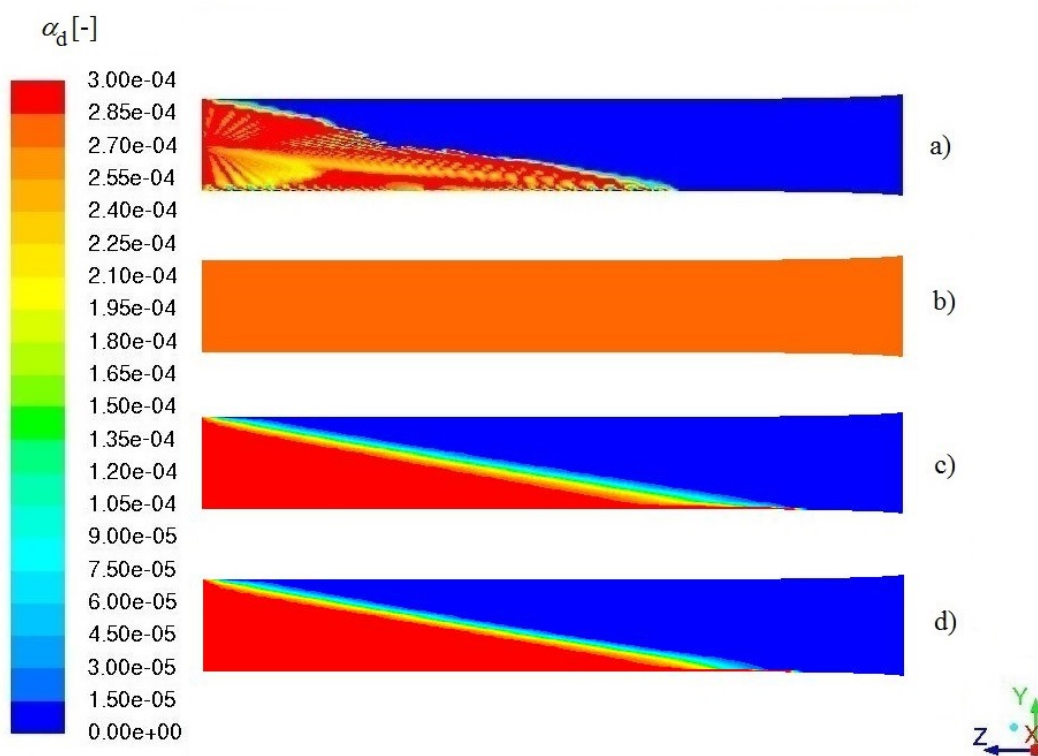


Figure 36. The contours of volume fraction in the by-pass pipe calculated by different models. a) DPM b) Homogeneous multiphase model c) Drift-flux model d) Eulerian model

Although the drift-flux model is able to model the saltation and moving bed regimes, it cannot model the stationary bed regime. This is because the mixture model cannot change its available flow area when the particles deposited on the bottom of the pipe reduce the flow area in practice. [34]

Table 13. The prediction of sedimentation by different models.

Fraction of the incoming particles	DPM	Mixture		Eulerian
		Homogeneous	Drift-flux	
Effluent	0 %	100 %	89 %	77 %
Deposit	100 %	0 %	11 %	23 %

It depends on the particle density and flow regime how the dispersed phase mass flow rate entering the mixing tank is divided between the effluent pipes. The greater the material density ratio, the smaller the pipe Froude number. The pipe Froude number smaller than unity indicates that the flow regime turns from homogeneous or heterogeneous to saltation or moving bed regime. In the present work, the fluid entering the mixing tank from the by-pass pipe "collides" with the fluid from the duct. This is due to the secondary flow in the by-pass pipe as described in Chapter 6.1.1. The position of the maximum axial flow velocity is shifted towards the outer wall of the pipe from the pipe centerline. Because flow is not fully developed before it enters the mixing tank from the by-pass pipe, the fluid does not flow straight from the by-pass pipe towards the back wall of the mixing tank, but it flows slightly towards the left hand side of the mixing tank "colliding" with the fluid from the duct. This is shown in Figure 37, where the contour plots of velocity field are shown and the flow directions are marked by arrows.

The fluid from the duct has greater velocity than the fluid from the by-pass pipe and it starts to lift towards the ceiling of the mixing tank when it encounters the back wall of the mixing tank. There is a decrease in the wall shear stress where the fluid starts to lift upwards. Due to the decrease in wall shear stress, when particle density is 1075 kg/m^3 , particles form a saltation regime on the floor of the mixing tank, and they are able to flow "under" the fluid from the duct to the left hand side of the mixing tank as shown by arrows in Figure 38. Figure represents the contour plots of volume fraction on the floor of the mixing tank and velocity vectors in the middle of the tank. The results are calculated by the drift-flux model.

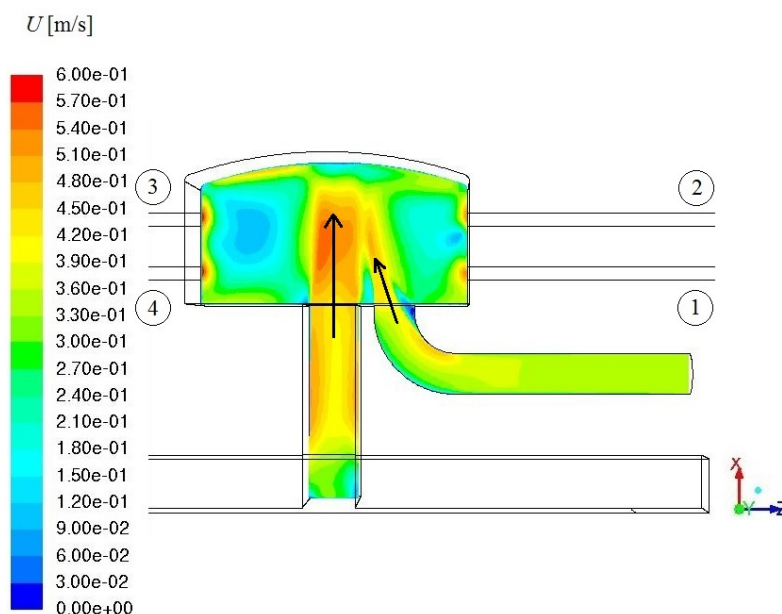


Figure 37. The contours of velocity in the mixing tank.

The most part of the incoming particles is carried to the third effluent pipe on the left hand side of the tank, when flow regime is moving bed or saltation. The values of wall shear stress and volume fraction on the floor and in the middle of the mixing tank are shown in Figure 39. As a conclusion, the smaller the wall shear stress, the more particles are able to flow from the right hand side of the mixing tank to the left hand side.

In the case of homogeneous flow regime, particles are not gathered on the floor of the mixing tank and the most of them are not able to flow from the right hand side of the mixing tank to the left hand side where the wall shear stress gets small values. Now, the fluid from the duct forms a "wall" in the middle of the mixing tank and makes the homogeneous suspension from the by-pass pipe to turn towards the effluent pipes 1 and 2 on the right hand side of the mixing tank as shown in Figure 40, which represents the trajectories for the particles from the by-pass pipe. The trajectories are colored by the dispersed phase volume fraction, α_d . Because of the homogeneous flow regime, the concentration of solid suspension is equal between the pipes 1 and 2 as shown in Table 14.

In Table 14, the results of the Eulerian model are calculated using the per-phase

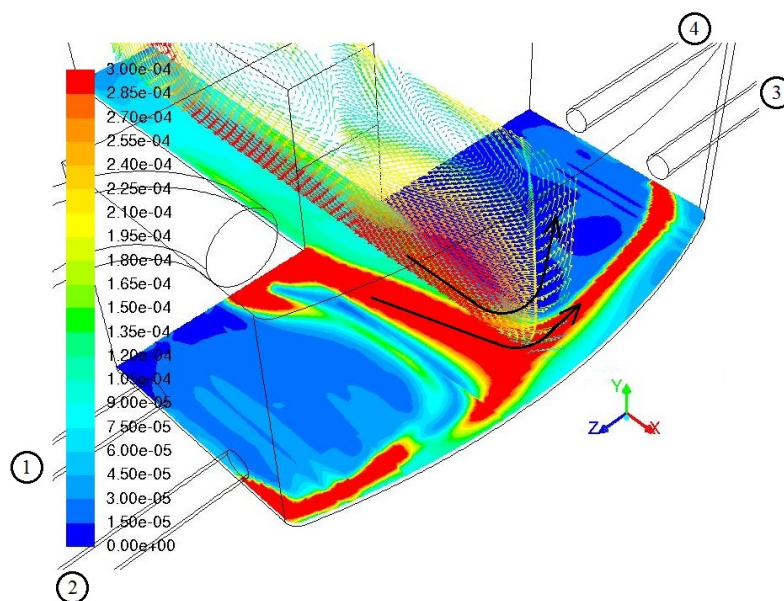


Figure 38. The contours of volume fraction on the floor and velocity vectors in the middle of the mixing tank.

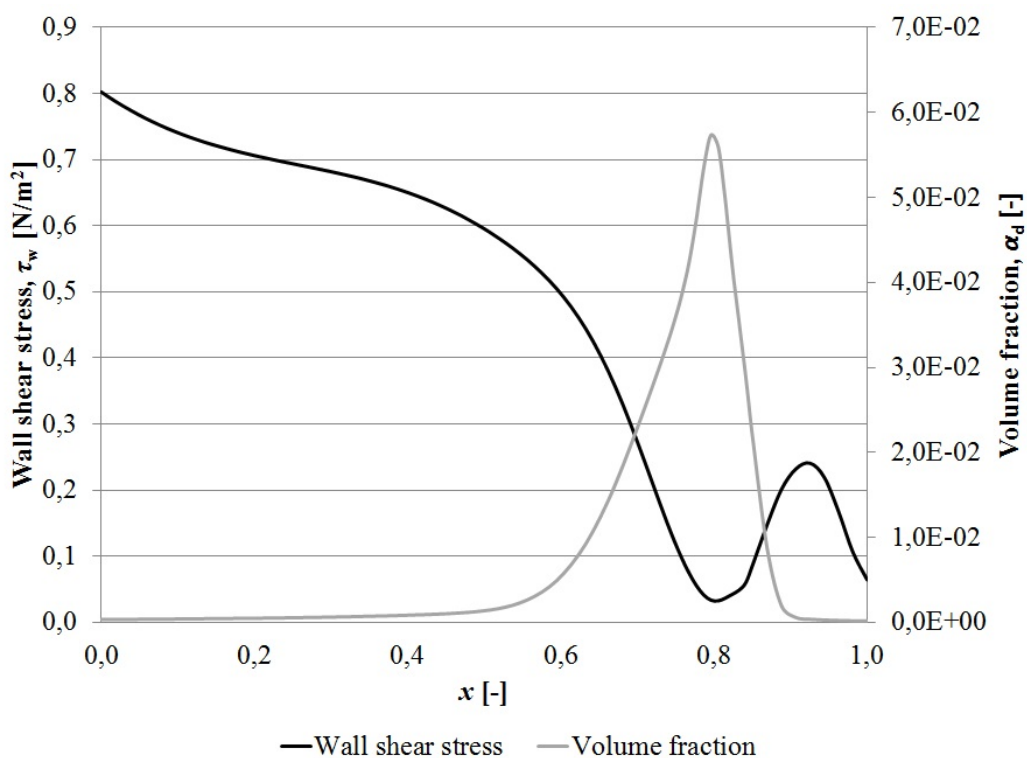


Figure 39. Wall shear stress and volume fraction on the floor, in the middle of the mixing tank.

turbulence model, which solves turbulence equations for both phases. The results show that the drift-flux model underestimates the amount of solid phase in the ef-

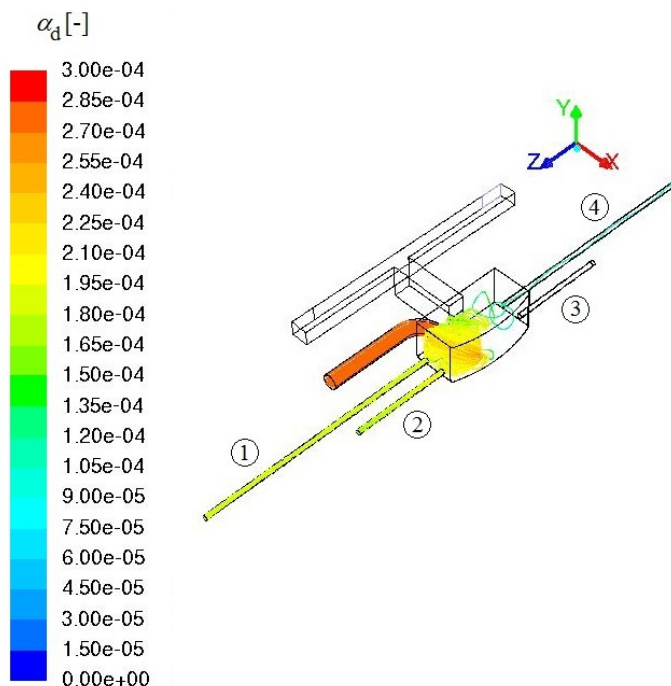


Figure 40. The trajectories of the particles from the by-pass pipe colored by the dispersed phase volume fraction.

fluent pipes 1 and 4, while it overestimates it in the effluent pipe 3 compared to the Eulerian model. Because the Eulerian model solves separate Navier-Stokes equations for continuous and dispersed phases, it gives more realistic results than the drift-flux model, which uses mixture properties to solve the continuity and momentum equations. Now, the mixture density almost equals to that of the continuous phase because the dispersed phase volume fraction is relatively low. The mixture density affects in the Navier-Stokes equations so that the mixture model underestimates sedimentation of particles and 12 percentage points more particles flow out of the mixing tank compared to the Eulerian model as shown in Table 13. Compared to the drift-flux model, the Eulerian model predicts that particles are divided more uniformly between the effluent pipes.

The results of the drift-flux model would be more accurate and the difference between the results of the drift-flux and Eulerian models would be smaller, if mixture density were closer to the value of the particle density or if the material density ratio were closer to the value of 1. Mixture density would approach particle density if

Table 14. The percentage of dispersed phase mass flow rate between effluent pipes predicted by different models.

Model	Fraction of the effluent particles			
	Pipe 1	Pipe 2	Pipe 3	Pipe 4
	[%]	[%]	[%]	[%]
DPM	0	0	0	0
Homogeneous	33	31	18	18
Drift-flux	5	21	71	3
Eulerian	10	21	59	11

the dispersed phase volume fraction, α_d , was increased, because now it is relatively low. The change in mixture density would prevent the drift-flux model from underestimating sedimentation of particles. On the other hand, when the density of the dispersed phase approaches that of the continuous phase, the material density ratio approaches unity and the pipe Froude number (Equation (103)) approaches infinity. In that case, the mixture approaches homogeneous and the results of the drift-flux model should not differ from those of the Eulerian model. As a conclusion, the drift-flux model is appropriate to model problem, where the properties of phases approach each other, that is the material density ratio is in the vicinity of 1.

In any case, the particles are not equally distributed to the effluent pipes 1–4 without better configuration of the mixing tank, guide vane or mixer. With the present configuration of the mixing tank, the best situation from the aeration tanks' point of view is the one with homogeneous flow regime.

In addition to the per-phase turbulence model, transport equations of turbulence quantities can be solved using either the dispersed or mixture turbulence model in ANSYS Fluent software, when multiphase flow is modeled using the Eulerian model and turbulence is modeled using $k - \varepsilon$ model. As described in Chapter 3.3.1, the mixture turbulence model uses mixture properties and velocities to estimate the values of turbulence quantities, the dispersed turbulence model derives the turbulence of dilute dispersed phase from the turbulence of the continuous phase, and

the per-phase turbulence model solves a set of k and ε transport equations for each phase. [50]

These three turbulence models of the Eulerian model are compared to each other and the results are shown in Tables 15 and 16, and in Figures 41 and 42. As Table 15 shows, the amount of effluent dispersed phase estimated by the dispersed turbulence model equals to that estimated by the most accurate per-phase turbulence model. The same results are shown in Figure 41, too. The discrepancy of the mixture turbulence model is a consequence of mixture properties and velocities used to estimate the turbulence quantities. Although the mixture turbulence model underestimates the amount of effluent particles, Table 16 and Figure 42 show that the percentage of dispersed phase mass flow rate between effluent pipes estimated by the mixture turbulence model equals to those of the dispersed and per-phase turbulence models.

Table 15. The prediction of sedimentation by different turbulence models of the Eulerian model.

Fraction of the incoming particles	Turbulence model		
	Dispersed	Mixture	Per-phase
Effluent	76 %	68 %	77%
Deposit	24 %	32 %	23 %

The standard deviation of the results represented in Table 15 is 4.6 % and the standard deviation of the results represented in Table 16 is 1.5 % at the maximum (effluent pipe 3) and 0.8 % on average. It can be concluded that all turbulence models used in conjunction with the Eulerian model give equal results, but the mixture turbulence model would be more appropriate in the cases where the dynamics of two phases are closely coupled.

A conclusion about the spreading of the particles in the mixing tank is that when the flow regime approaches homogeneous suspension, the most of the particles from the by-pass pipe are carried to the effluent pipes 1 and 2 on the right hand side of the mixing tank. On the other hand, when the particles form a moving bed or saltation

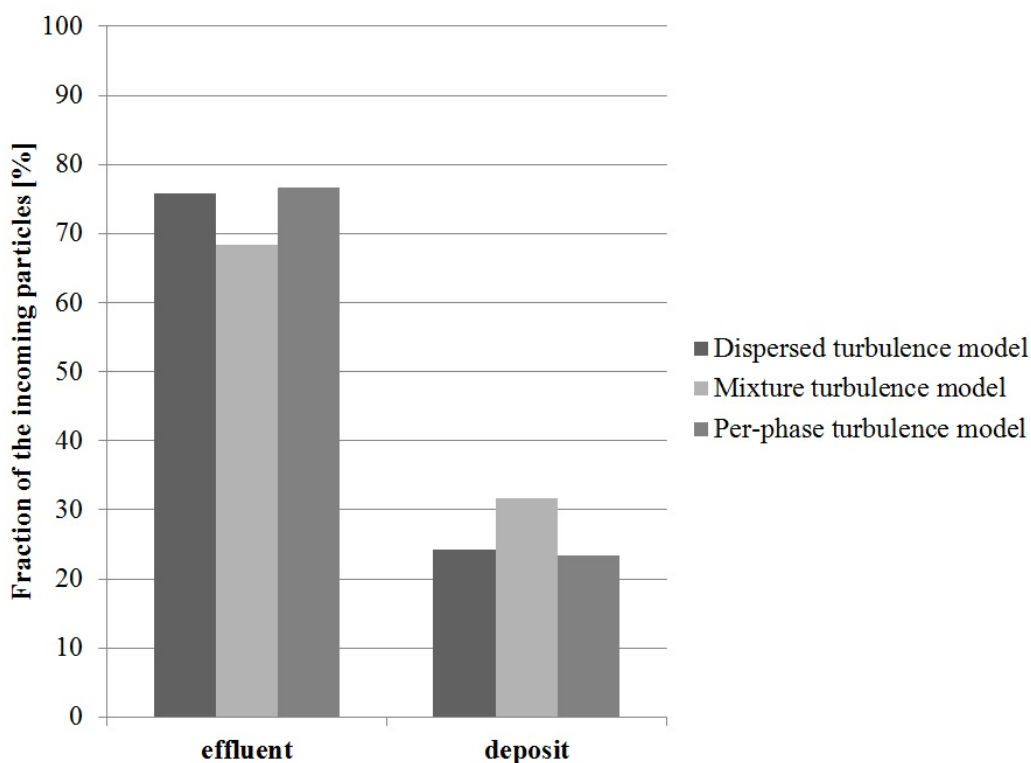


Figure 41. The fraction of the incoming particles predicted by different turbulence models of the Eulerian model.

Table 16. The percentage of dispersed phase mass flow rate between effluent pipes predicted by different turbulence models of the Eulerian model.

Turbulence model	Fraction of the effluent particles			
	Pipe 1 [%]	Pipe 2 [%]	Pipe 3 [%]	Pipe 4 [%]
Dispersed	11	21	57	12
Mixture	11	21	56	12
Per-phase	10	21	59	11

regime, the most of the particles from the by-pass pipe are carried to the effluent pipe 3 on the left hand side of the mixing tank. This is predicted by both the drift-flux and Eulerian models. Because the drift-flux model uses the mixture properties to solve the continuity and momentum equations, it predicts that more particles flow out of the mixing tank than the Eulerian model, which solves the continuity and momentum equations for both phases. Because of this simplification, the effect

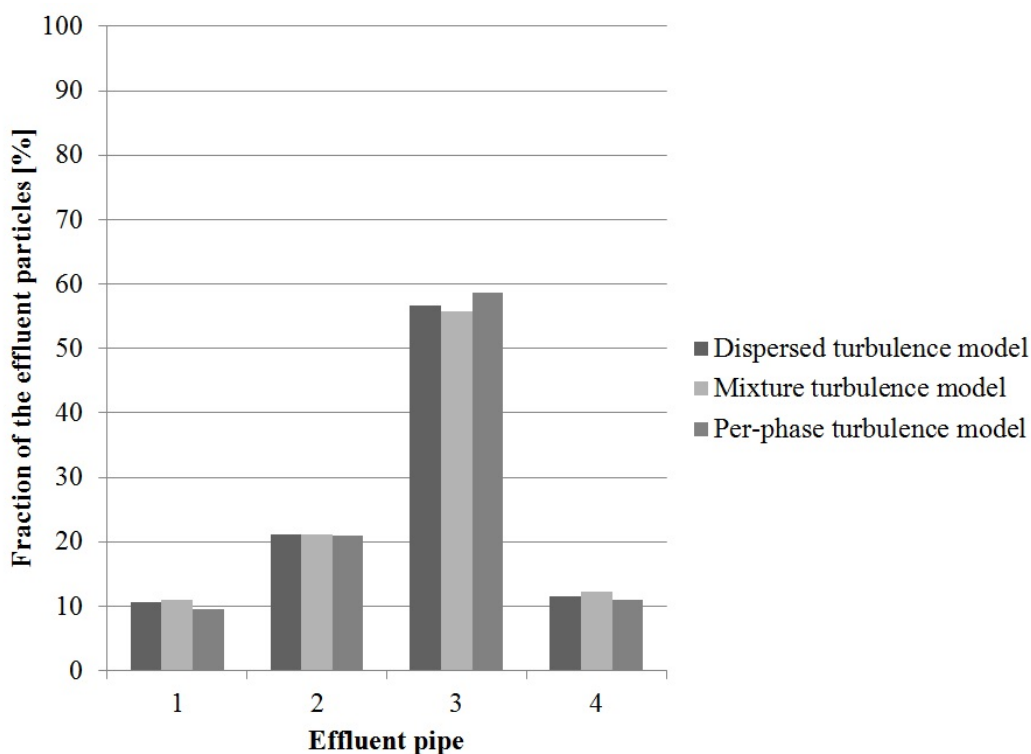


Figure 42. The fraction of the effluent particles predicted by different turbulence models of the Eulerian model.

of gravitational forces on particles is underestimated by the drift-flux model.

There are no significant discrepancies between the results calculated by different turbulence models of the Eulerian model. In the case of dilute two-phase flow as in the present work, the dispersed and per-phase turbulence models give equal results. As discussed in Chapter 5.6, the Eulerian model is the most time consuming multi-phase model, and if the Eulerian model is chosen for simulation purposes, the most accurate per-phase turbulence model is worth for choosing in the case of two-phase flow, because the computational time required by the per-phase model does not differ from time required by other models. If one can assume that both phases share the same turbulence field, the mixture turbulence model is recommended [19].

6.6 Modeling of Turbulent Dispersion

In ANSYS Fluent software, the discrete phase model and the Eulerian model are capable of modeling turbulent dispersion. It is the effect of continuous phase velocity fluctuations on the particle trajectories. The effects of the stochastic tracking model and the cloud tracking model in the Eulerian-Lagrangian approach, and the effect of the model of Burns et al. in the Eulerian-Eulerian approach on spreading of the particles are compared to the situation where turbulent dispersion is neglected.

Zhang and Chen [28] studied particle concentration distributions in ventilated enclosed spaces using the stochastic tracking model and according to them the number of particles should be larger than the number of mesh elements to ensure a statistical stability. Firstly, the number of tracked particles was 4324 in the present work. Then the number of particles was increased to 1 961 320, then to 3 891 600, and finally to 9 469 560. The results show that the increase in the number of tracked particles has no influence on results (difference is less than 3 %). The only difference is that the dispersed phase volume fraction field looks less scattered when the number of particles is increased.

The effect of turbulent dispersion on particles is shown in Figures 43 and 44. In the former one, the contour plots of dispersed phase volume fraction on the bottom of the by-pass pipe are shown. The latter one shows the contour plots of dispersed phase volume fraction in the by-pass pipe in vertical direction. The grey lines in figure represent the locations where the values of volume fraction in y direction are observed before the bend and compared to the case without turbulent dispersion model. Because the Eulerian model is able to predict saltation and moving bed regimes unlike the discrete phase model, Figures 43 d) and 44 d) are not comparable to others in streamwise direction. However, as can be seen in Figure 44, there is no difference between models in vertical direction.

The stochastic tracking (discrete random walk) model predicts that particles flow 24 % further downstream in streamwise direction in the by-pass pipe and duct

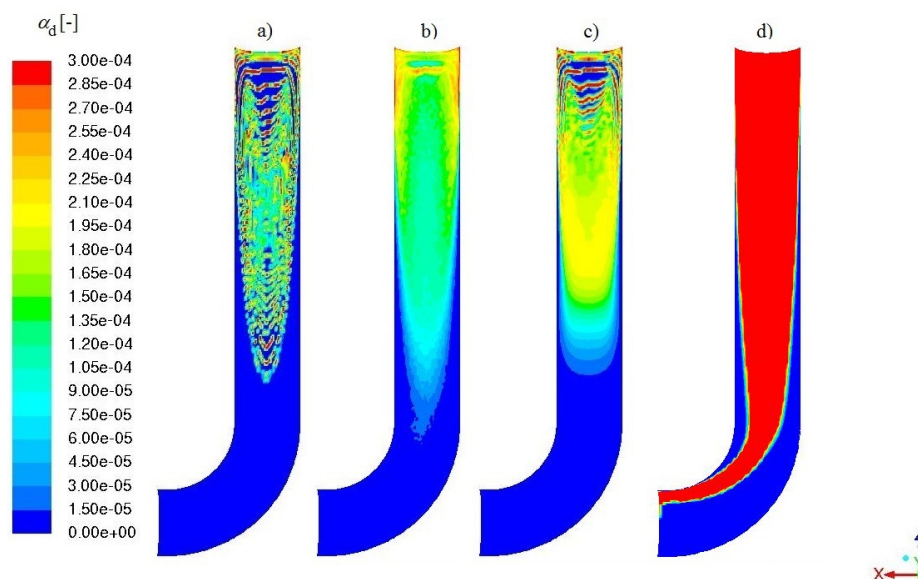


Figure 43. The contours of volume fraction on the bottom of the by-pass pipe calculated by different turbulent dispersion models. a) Turbulent dispersion neglected b) Stochastic tracking c) Cloud tracking d) Burns et al.

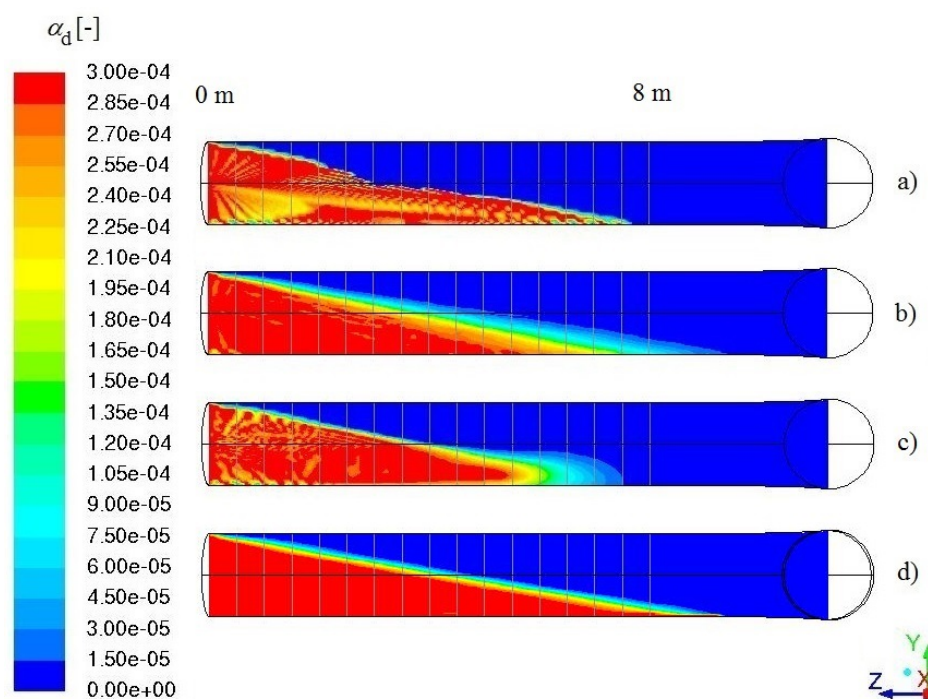


Figure 44. The contours of volume fraction in the by-pass pipe calculated by different turbulent dispersion models. a) Turbulent dispersion neglected b) Stochastic tracking c) Cloud tracking d) Burns et al.

compared to the case without turbulent dispersion model, while the cloud tracking model predicts that particles flow as far downstream in streamwise direction as in the case without turbulent dispersion (Figure 44). The studied particle density is 1075 kg/m^3 . The effect of turbulent fluctuations on particles starts approximately 2.5 meters from the inlet of the by-pass pipe. The lifting effect of turbulent fluctuations on particles increases in streamwise direction.

The results represented in Figures 43 d) and 44 d) are calculated using the per-phase turbulence model of the Eulerian model, which solves the transport equations of turbulence quantities for both phases. The effect of turbulent dispersion is studied also in the case of the dispersed and mixture turbulence models. The results are shown in Tables 17 and 18, and in Figures 45 and 46. Table 17 and Figure 45 represent how the models estimate the fraction of particles, which either flow out of the mixing tank or deposit on the floor of the tank, when turbulent dispersion is taken into account. The standard deviation of the results represented in Table 17 is 4.9 %.

Table 18 and Figure 46 represent how the dispersed phase mass flow rate is divided between the effluent pipes predicted by different models when turbulent dispersion is taken into account. The standard deviation of the results represented in Table 18 is 2.9 % at the maximum (effluent pipe 3) and 1.8 % on average.

Table 17. The prediction of sedimentation by different turbulence models of the Eulerian model when the effect of the turbulent dispersion model (Burns et al.) is considered.

Turbulence model	Effluent [%]	Deposit [%]
Dispersed + Burns et al.	89	11
Mixture + Burns et al.	88	12
Per-phase + Burns et al.	80	20

The conclusion is that the importance of modeling of turbulent dispersion depends on the size of the studied geometry, particle size, and material density ratio. If only the by-pass pipe or the duct were observed, it would be important to take the influ-

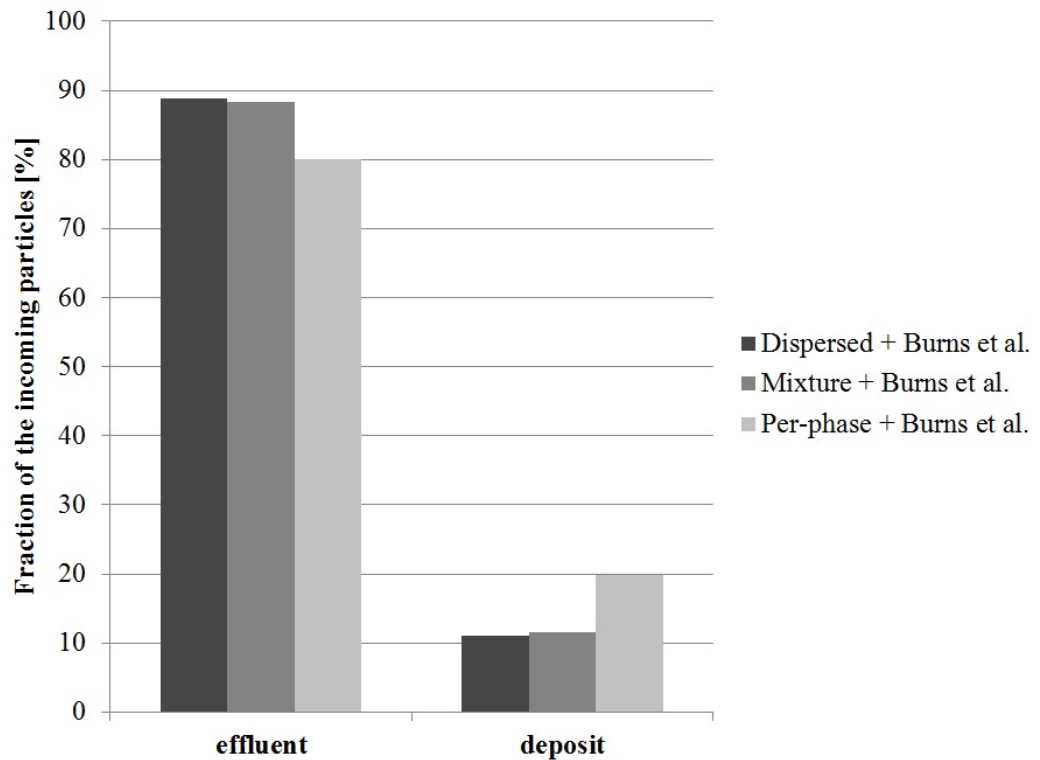


Figure 45. The fraction of the incoming particles predicted by different turbulence models of the Eulerian model when the effect of the turbulent dispersion model (Burns et al.) is considered.

Table 18. The percentage of the effluent dispersed phase mass flow rate between the pipes predicted by different turbulence models of the Eulerian model when the effect of the turbulent dispersion model (Burns et al.) is considered.

Turbulence model	Pipe 1 [%]	Pipe 2 [%]	Pipe 3 [%]	Pipe 4 [%]
Dispersed + Burns et al.	8	28	58	7
Mixture + Burns et al.	9	29	54	9
Per-phase + Burns et al.	8	33	53	7

ence of turbulent dispersion on particles into account. In larger scale, the discrete phase model predicts that all incoming particles deposit on the bottom of the bypass pipe and duct although turbulent dispersion is taken into account. Therefore, turbulent dispersion does not make the particles to flow into the mixing tank and out of the effluent pipes in the case of the discrete phase model. However, in the case of lighter particles, the mixing would be more efficient and more realistic if

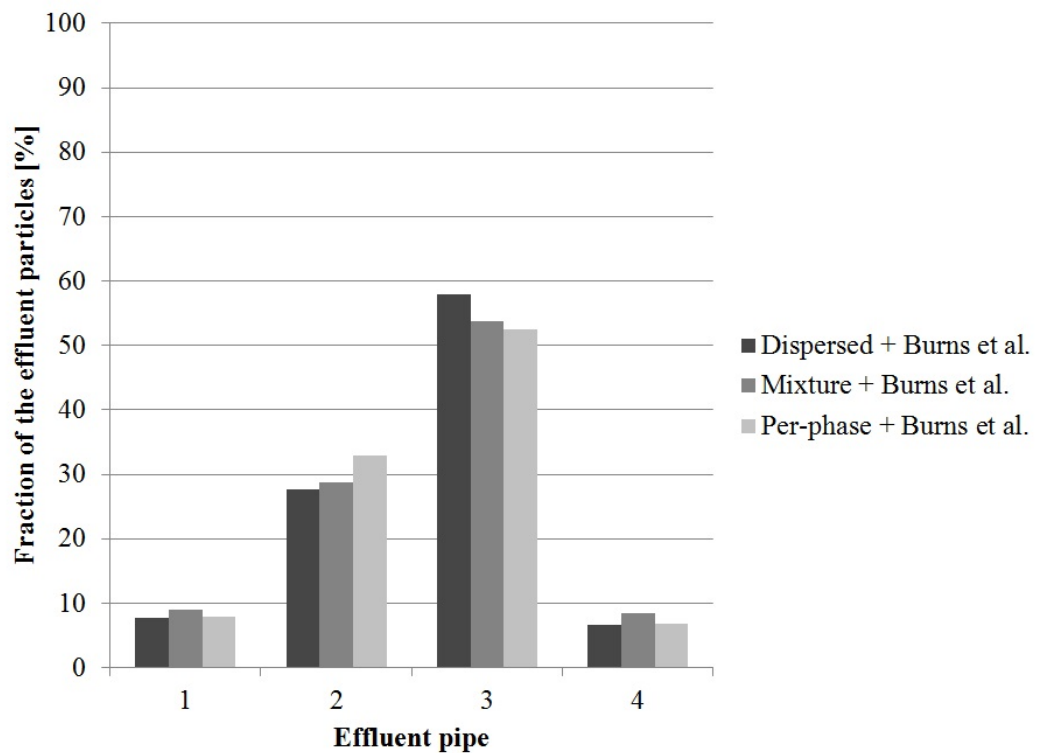


Figure 46. The fraction of the effluent particles predicted by different turbulence models of the Eulerian model when the effect of the turbulent dispersion model (Burns et al.) is considered.

the influence of turbulent dispersion on particles were taken into account with the discrete phase model.

In the case of the Eulerian model, there is an increase in the amount of effluent solid phase when turbulent dispersion is taken into account. The increase is greater in the case of the dispersed and mixture turbulence models than in the case of the per-phase turbulence model. In the by-pass pipe before the bend, the height of the bed of particles increases only 9 % from the value of $0.11 y/d$ to $0.12 y/d$ because of turbulent dispersion. The influence of turbulent fluctuations on particles is more significant in the mixing tank than in the by-pass pipe or duct (Figure 47).

The influence of turbulent dispersion is the most significant when the mixture turbulence model is used in conjunction with the Eulerian model. The influence of the continuous phase turbulent fluctuations on particles can be seen in Figure 47, where the isosurfaces of dispersed phase volume fraction are shown, when the value of

the volume fraction equals to 0.0003 (the volume fraction of the by-pass pipe influent). Figure 47 a) represents the isosurfaces when turbulent dispersion is neglected and Figure 47 b) represents the isosurfaces when turbulent dispersion is taken into account. Figures indicate that turbulent fluctuations of the continuous phase affect particle trajectories and therefore in Figure 47 b) more particles are able to flow to the effluent pipe 2 than in Figure 47 a). More efficient mixing of the phases due to turbulent dispersion causes that more particles flow out of the tank to the effluent pipes.

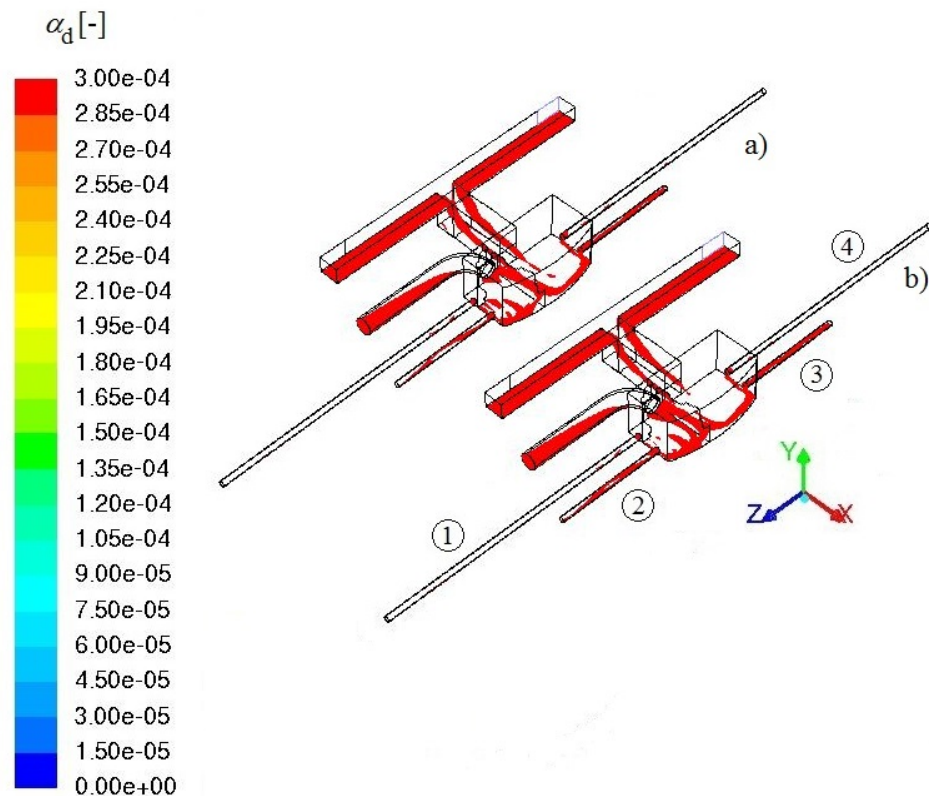


Figure 47. The isosurfaces of dispersed phase volume fraction. a) Turbulent dispersion neglected
b) Burns et al. model

Similarly as the drift-flux model underestimates sedimentation of particles, also the dispersed and mixture turbulence models in conjunction with the Eulerian model may underestimate sedimentation of particles when turbulent dispersion is taken into account. Because the dispersed turbulence model derives the turbulence of the dispersed phase from the turbulence of the continuous phase, and the mixture turbulence model uses mixture properties and velocities to estimate the turbulence

quantities, they may overestimate the effect of turbulence fluctuations on particles, when the material density ratio of the phases is 1.075. Because the per-phase turbulence model solves the transport equations of turbulence quantities for both phases, it is assumed that the per-phase turbulence model gives the most accurate results. And as Table 17 and Figure 45 show, the consideration of turbulent dispersion does not significantly affect the results, when the per-phase turbulence model is used. When turbulent dispersion is taken into account, the most remarkable change can be seen in the amount of the effluent solid phase of the pipe 2, but all the models are able to show similar increase.

Bearing in mind that there is no experimental data available in the present work, the comparison of the results is done between other CFD results. Despite the lack of experimental data, the standard deviation in the CFD results is only 4.9 %, when different turbulence models of the Eulerian model are compared.

However, it is unclear whether the consideration of turbulent dispersion gives more or less realistic results than the simulation without consideration of turbulent dispersion, because of the lack of experimental data. In reality, the turbulent fluctuations of the continuous phase affect particles, but in future it would be interesting to study whether the effect is as strong as the CFD results show, if turbulence modulation was taken into account, too.

6.7 Pressure Losses in Two-Phase Flow

Pressure losses are important to be estimated when wastewater treatment plant is designed and they are important to be observed when the wastewater treatment process is in progress. In the present work, pressure losses are observed in the by-pass pipe with 90-degree bend and in straight effluent pipes with different lengths. The pressure loss can be estimated from

$$\Delta p_{\text{loss}} = \left(f \frac{l}{d} + \sum K \right) \frac{1}{2} \rho_m u^2, \quad (145)$$

where f is the friction coefficient, l pipe length, d pipe diameter, K loss coefficient, ρ_m mixture density, and u velocity. The friction coefficient based on Reynolds number and relative surface roughness can be found in the Moody chart or the Colebrook formula

$$\frac{1}{\sqrt{f}} = -2 \log \left(\frac{k_s/d}{3.7} + \frac{2.51}{Re\sqrt{f}} \right) \quad (146)$$

which is valid for the turbulent portion of the Moody chart [52]. The term k_s refers to surface roughness.

Because of the large pipe diameter and low velocity in the by-pass pipe, both Equation (145) and CFD simulation predict that pressure loss is only 1 Pa/m in the by-pass pipe. The 90-degree bend has no significant influence on the pressure loss.

The smaller pipe diameter and higher velocity in the effluent pipes increase the pressure loss due to friction. Pressure losses in the effluent pipes from CFD simulation calculated using ANSYS Fluent 14.5 and from estimation based on friction coefficient from the Colebrook formula are shown in Figure 48. In figure, the error bars due to numerical uncertainty are shown. The pressure loss from CFD simulation almost equals to that from Equation (145). The difference between results is only 2 % and if the discretization error is taken into account, the estimated value is in the range of the CFD solution.

It can be concluded that the results from Equation (145) and CFD simulation equal to each other.

6.8 Development of the Computational Tool

According to Chapter 1, one aim of this thesis is to develop unequivocal computational tool, which helps to analyze the two-phase flow problem before CFD modeling, set correct initial values, choose the most suitable multiphase model, and compare the CFD results with theory. This tool is developed using Microsoft Excel spreadsheet software. It includes all parameters and dimensionless groups impor-

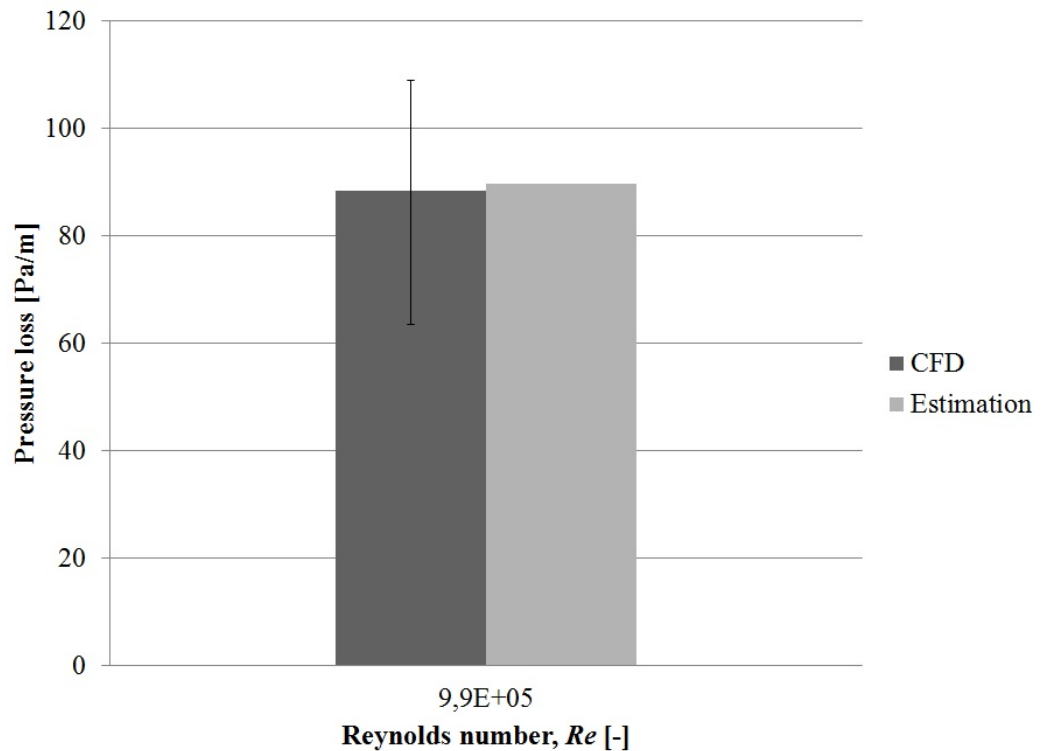


Figure 48. Pressure losses calculated using Fluent and estimated based on friction coefficient from the Moody chart.

tant for two-phase flow, which are introduced in this thesis.

The user needs only to enter material properties, flow rates, and dimensions of the geometry specific for the studied problem, and the tool solves the unknown values which the CFD software requires to be specified. The tool also solves important dimensionless groups and tells the user conclusions about them. For example, the tool tells whether the coupling of the phases is one-way, two-way, or four-way. It gives information about the flow regime and recommends which ones of the interfacial surface forces can be neglected. Also the calculation procedure for the discretization error is included in the tool.

7 CONCLUSIONS AND RECOMMENDATIONS

In literature, there are few studies on liquid-solid flow in industrial scale, but any information about this particular case cannot be found. More research is done on sedimentation or mixing in stirred tanks in laboratory scale. Also simpler geometries are studied than the one in the present work. By taking advantage of the shapes of cube and cylinder, the high quality hexahedral mesh can be applied to complex large-scale geometry instead of poor quality tetrahedral mesh.

In the present work, the part of the wastewater treatment process referred to as the mixing tank, is studied. In the mixing tank, wastewater from the primary settling tanks is mixed with overflow wastewater before the mixture flows to the aeration tanks. For high process performance in the aeration tanks, the organic material should be well mixed in the mixing tank and equally distributed to the aeration tanks. The results show that the spreading of particles is dependent on material density ratio. Despite the flow regime, mixing of flows is inefficient without better configuration of the mixing tank, guide vane or mixer. The best situation from the aeration tanks' point of view is the one with homogeneous flow regime.

One way to achieve more efficient mixing is to increase turbulence intensity, because then the velocity fluctuations cause turbulent dispersion of particles. In the case of the discrete phase model, neither the stochastic nor cloud tracking model is able to overcome the weakness of the discrete phase model, which is that it cannot model the saltation or moving bed flow regime. The results show that turbulent dispersion enhance mixing of the phases and thus more particles flow out of the mixing tank when turbulent dispersion is considered. However, it is unclear whether the consideration of turbulent dispersion gives more or less realistic results, because of the lack of experimental data.

Particles can also affect turbulence of the continuous phase. Depending on the properties of the particles and the location with respect to the wall, they can either augment or attenuate turbulence. However, models of today only predict either

dissipation or production of turbulence, or they are not generally accepted. One challenging task in the future would be to find a generally accepted way to take turbulence modulation into account. In future, it would be interesting to study whether the effect of continuous phase turbulent fluctuations on particles is as strong as the CFD results show, if turbulence modulation was taken into account, too.

In addition to inefficient mixing, erosion can cause problems in wastewater treatment plants. Especially the pipe bends are exposed to erosion. The results, which include the boundary-layer characteristics, show that the location of the most intense erosion is shifted with respect to flow regime because of secondary flows, which are perpendicular to the main flow. The deposition of particles on the floors increases wall shear stress, which increases drag force and pressure drop, and therefore the efficiency of the process is reduced. Thus, homogeneous or heterogeneous flow regime should be preferred over saltation and moving bed regimes. In this thesis, flow is referred to as homogeneous if the variation in the particle concentration from the top to the bottom of the pipe is less than 20 %.

Besides the difficulties in wastewater treatment process, there are difficulties also in the modeling of multiphase flows. The literature review showed that the coupling of the dispersed and continuous phases is complicated. Thus, the flow regime needs to be known carefully before the CFD simulation. By calculating the deposition velocity of particles and the pipe Froude number, and estimating the flow regime, the physics of the flow can be estimated and correct settings for the multiphase model can be chosen. In the present work, the computational tool is developed for this purpose.

It should be noticed that correlations including experimental constants are only rough estimations and in some cases it is recommended to compare results calculated by different settings. At least the mesh independence test is recommended, because it gives results for the estimation of numerical uncertainty due to the discretization error. When there is no experimental data available, the analysis of discretization error gives an estimation of the uncertainty in results.

The comparison between multiphase models shows that the discrete phase model is valid for flows with the pipe Froude number greater than 1.0. In that case, the flow is heterogeneous or homogeneous, and the reflect boundary condition can be applied instead of the trap boundary condition. The homogeneous multiphase model is valid only for homogeneous suspension, whereas the drift-flux and Eulerian models are able to predict also flow regimes, where particles tend to settle.

When the pipe Froude number is smaller than unity, there are discrepancies between the results calculated by the drift-flux and Eulerian models, because the Eulerian model solves separate Navier-Stokes equations for continuous and dispersed phases and the drift-flux model uses mixture properties to solve the continuity and momentum equations. In the present work, the mixture density almost equals to that of the continuous phase because the dispersed phase volume fraction is relatively low. The mixture density affects in the Navier-Stokes equations so that it underestimates the tendency for particles to settle. Thus, the drift-flux model would be more appropriate to model problem, where the material density ratio is in the vicinity of 1. The same applies to the usage of the mixture turbulence model in conjunction with the Eulerian model. If the most time consuming Eulerian model is chosen for simulation purposes, the most accurate per-phase turbulence model is worth for choosing, because the computational time required by it does not differ from the time required by the dispersed or mixture turbulence models.

The results indicate that the two-phase flows are more complicated to be modeled than the single-phase flows. The studied multiphase models predict the most accurate results when the mixture can be assumed to be homogeneous and thus the Navier-Stokes equations can be applied without complex interfacial coupling terms. Mixture of liquid and solid phases is homogeneous, when the material density ratio is 1 and the pipe Froude number approaches infinity. In that case, all the studied multiphase models should give equal results. With increasing material density ratio and decreasing pipe Froude number, the Eulerian model in conjunction with the per-phase turbulence model gives the most accurate results, because it does not include simplifications in Navier-Stokes equations like the other models.

REFERENCES

- [1] Helsinki Region Environmental Services Authority (HSY). Viikinmäki Wastewater Treatment Plant. [In HSY www-pages]. Updated: August 2, 2010. [retrieved July 16, 2013]. From: www.hsy.fi/en/waterservices/wastewater_treatment/Pages/viikinmaki.aspx.
- [2] Water UK. Wastewater Treatment and Recycling. [www-document]. Updated: November 5, 2006. [retrieved July 16, 2013]. From: www.water.org.uk/home/news/press-releases/wastewater-pamphlet/wastewater-web--2-.pdf.
- [3] Environmental Protection Agency of United States. Screening and Grit Removal. [e-document]. 2003. [retrieved September 5, 2013]. Wastewater Technology Fact Sheet. From: <http://water.epa.gov/scitech/wastetech/mtbfact.cfm>.
- [4] New York City Department of Environmental Protection (NYC DEP). New York City's Wastewater Treatment System. [www-document]. [retrieved July 16, 2013]. From: www.nyc.gov/html/dep/pdf/wssystem.pdf.
- [5] Environmental Protection Agency of Ireland. *Wastewater Treatment Manuals: Primary, Secondary and Tertiary Treatment*. Environmental Protection Agency, Ireland, 1997. p. 131. ISBN 1-899965-46-7.
- [6] J. Bridgeman, B. Jefferson, and S.A. Parsons. Computational Fluid Dynamics Modelling of Flocculation in Water Treatment: A Review. *Engineering Applications of Computational Fluid Mechanics*, 3(2):220–241, 2009.
- [7] K. Hiltunen. *Multiphase Flow Dynamics*. Espoo: Technical Research Centre of Finland (VTT). Publications 722, 2009. p. 113. ISBN 978-951-38-7365-3.
- [8] H. Enwald, E. Peirano, and A.-E. Almstedt. Eulerian Two-Phase Flow Theory Applied To Fluidization. *International Journal of Multiphase Flow*, 22:21–66, 1996.

- [9] C. Crowe, M. Sommerfeld, and Y. Tsuji. *Multiphase Flows with Droplets and Particles*. Boca Raton (FL): CRC Press cop., 1998. p. 471. ISBN 0-8493-9469-4.
- [10] M. Ishii and T. Hibiki. *Thermo-Fluid Dynamics of Two-Phase Flow*. New York: Springer New York, 2nd edition, 2011. p. 473. ISBN 978-1-4419-7985-8.
- [11] A.H. Azimi, D.Z. Zhu, and N. Rajaratnam. Effect of Particle Size on the Characteristics of Sand Jets in Water. *Journal of Engineering Mechanics*, ASCE 137:822–834, 2011.
- [12] R.P. King. *Introduction to Practical Fluid Flow*. Oxford: Butterworth-Heinemann, 2002. p. 198. ISBN 0-7506-4885-6.
- [13] B. Abulnaga. *Slurry Systems Handbook*. United States: McGraw-Hill, 2002. p. 629. ISBN 978-0-07-137508-5.
- [14] P. Doron and D. Barnea. Flow Pattern Maps for Solid-Liquid Flow in Pipes. *International Journal of Multiphase Flow*, 22(2):273–283, 1996.
- [15] S. Fokeer, S. Kingman, I. Lowndes, and A. Reynolds. Characterisation of the Cross Sectional Particle Concentration Distribution in Horizontal Dilute Flow Conveying - a Review. *Chemical Engineering and Processing: Process Intensification*, 43(6):677–691, 2004.
- [16] D.C. Wilcox. *Turbulence Modeling for CFD*. California: La Cañada, 1994. p. 460. ISBN 0-9636051-0-0.
- [17] G.N. Patel. CFD Simulation of Two-Phase and Three-Phase Flows in Internal-Loop Airlift Reactors. Master's thesis, Lappeenranta: Lappeenranta University of Technology, 2010. p. 73.
- [18] S.A. Morsi and A.J. Alexander. An Investigation of Particle Trajectories in Two-Phase Flow Systems. *Journal of Fluid Mechanics*, 55:193–208, 1972.
- [19] ANSYS, Inc. *ANSYS FLUENT Theory Guide*, 2012. Release 14.5. p. 754.

- [20] S. Subramaniam. Lagrangian-Eulerian Methods for Multiphase Flows. *Progress in Energy and Combustion Science*, 39(2-3):215–245, 2013.
- [21] J. Capecelatro and O. Desjardins. Eulerian-Lagrangian Modeling of Turbulent Liquid-Solid Slurries in Horizontal Pipes. *International Journal of Multiphase Flow*, 55(3):64–79, 2013.
- [22] C. He, J. Marsalek, and Q. Rochfort. Numerical Modelling of Enhancing Suspended Solids Removal in a CSO Facility. *Water Quality Research Journal of Canada*, 39(4):457–465, 2004.
- [23] M. Dufresne, J. Vazquez, A. Terfous, A. Ghenaim, and J.-B. Poulet. CFD Modeling of Solid Separation in Three Combined Sewer Overflow Chambers. *Journal of Environmental Engineering*, 135(9):776–787, 2009.
- [24] S.-S. Pathapati and J.J. Sansalone. CFD Modeling of a Storm-Water Hydrodynamic Separator. *Journal of Environmental Engineering*, 135(4):191–202, 2009.
- [25] R. Tarpagkou and A. Pantokratoras. CFD Methodology for Sedimentation Tanks: The Effect of Secondary Phase on Fluid Phase Using DPM Coupled Calculations. *Applied Mathematical Modelling*, 37(5):3478–3494, 2013.
- [26] G. Ying, J. Sansalone, S. Pathapati, G. Garofalo, M. Maglionico, A. Bolognesi, and A. Artina. Stormwater Treatment: Examples of Computational Fluid Dynamics Modeling. *Frontiers of Environmental Science & Engineering*, 6(5):638–648, 2012.
- [27] A.M. Goula, M. Kostoglou, T.D. Karapantsios, and A.I. Zouboulis. A CFD Methodology for the Design of Sedimentation Tanks in Potable Water Treatment: Case Study: The Influence of a Feed Flow Control Baffle. *Chemical Engineering Journal*, 140(1-3):110–121, 2008.
- [28] Z. Zhang and Q. Chen. Comparison of the Eulerian and Lagrangian Methods for Predicting Particle Transport in Enclosed Spaces. *Atmospheric Environment*, 41(25):5236–5248, 2007.

- [29] C.W. Hirt and B.D. Nichols. Volume of Fluid (VOF) Method for the Dynamics of Free Boundaries. *Journal of Computational Physics*, 39:201–225, 1981.
- [30] V.R. Gopala and B.G.M. van Wachem. Volume of Fluid Methods for Immiscible-Fluid and Free-Surface Flows. *Chemical Engineering Journal*, 141:204–221, 2008.
- [31] C. He and J. Marsalek. Hydraulic Optimization of a Combined Sewer Overflow (CSO) Storage Facility Using Numerical and Physical Modeling. *Canadian Journal of Civil Engineering*, 36(2):363–373, 2009.
- [32] A.A. Nadooshan. Simulation of Interfacial Flow with Volume-of-Fluid Method. *International Journal of Engineering and Applied Sciences*, 5(7):415–418, 2009.
- [33] M. Manninen, V. Taivassalo, and S. Kallio. *On The Mixture Model for Multiphase Flow*. Espoo: Technical Research Centre of Finland (VTT), 1996. p. 67. ISBN 951-38-4946-5.
- [34] J. Ling, P.V. Skudarnov, C.X. Lin, and M.A. Ebadian. Numerical Investigations of Liquid-Solid Slurry Flows in a Fully Developed Turbulent Flow Region. *International Journal of Heat and Fluid Flow*, 24(3):389–398, 2003.
- [35] M. Kostoglou, T.D. Karapantsios, and K.A. Matis. CFD Model for the Design of Large Scale Flotation Tanks for Water and Wastewater Treatment. *Industrial & Engineering Chemistry Research*, 46(20):6590–6599, 2007.
- [36] S.T. Johansen. *On the Modelling of Disperse Two-Phase Flows*. PhD thesis, Trondheim: Norwegian Institute of Technology, 1990. p. 280.
- [37] A. Halabia. Drag Force and Frictional Resistances in Vertically Vibrated Dense Granular Media. Master's thesis, Lappeenranta: Lappeenranta University of Technology, 2006. p. 101.
- [38] J. Wang, S. Wang, T. Zhang, and Y. Liang. Numerical Investigation of Ice Slurry Isothermal Flow in Various Pipes. *International Journal of Refrigeration*, 36(1):70–80, 2013.

- [39] S.K. Lahiri. Computational Fluid Dynamics Simulation of the Solid Liquid Slurry Flow in a Pipeline. In *Chemcon 2008 proceedings*, 2008. Rome, Italy, June 9-13, 2008.
- [40] S.K. Lahiri and K.C. Ghanta. Slurry Flow Modelling by CFD. *Chemical Industry & Chemical Engineering Quarterly*, 16(4):295–308, 2010.
- [41] D.R. Kaushal, T. Thiglas, Y. Tomita, S. Kuchii, and H. Tsukamoto. CFD Modeling for Pipeline Flow of Fine Particles at High Concentration. *International Journal of Multiphase Flow*, 43:85–100, 2012.
- [42] D.R. Kaushal, A. Kumar, Y. Tomita, S. Kuchii, and H. Tsukamoto. Flow of Mono-Dispersed Particles Through Horizontal Bend. *International Journal of Multiphase Flow*, 52:71–91, 2013.
- [43] O.A. Marzouk and E.D. Huckaby. Simulation of a Swirling Gas-Particle Flow Using Different k-epsilon Models and Particle-Particle Relationships. *Engineering Letters*, 18(1):56–67, 2010.
- [44] V. Yakhot, S.A. Orszag, S. Thangam, T.B. Gatski, and C.G. Speziale. Development of Turbulence Models for Shear Flows by a Double Expansion Technique. *Physics of Fluids A*, 4(7):1510–1520, 1992.
- [45] T.-H. Shih, W.W. Liou, A. Shabbir, Z. Yang, and J. Zhu. A New k- ϵ Eddy Viscosity Model for High Reynolds Number Turbulent Flows. *Computers & Fluids*, 24(3):227–238, 1995.
- [46] F.R. Menter. Two-Equation Eddy-Viscosity Turbulence Models for Engineering Applications. *AIAA Journal*, 32(8):1598–1605, 1994.
- [47] F.R. Menter, M. Kuntz, and R. Langtry. Ten Years of Industrial Experience with the SST Turbulence Model. In K. Hanjalic, Y.Nagano, and M.Tummers, editors, *Turbulence, Heat and Mass Transfer IV*, pages 625 – 632. Begell House, Inc., 2003. ISBN: 1-56700-196-3.
- [48] A. Dehbi. A CFD Model for Particle Dispersion in Turbulent Boundary Layer Flows. *Nuclear Engineering and Design*, 238:707–715, 2008.

- [49] A.H. Azimi, D.Z. Zhu, and N. Rajaratnam. Computational Investigation of Vertical Slurry Jets in Water. *International Journal of Multiphase Flow*, 47:94–114, 2012.
- [50] T. Virdung and A. Rasmuson. Hydrodynamic Properties of a Turbulent Confined Solid-Liquid Jet Evaluated Using PIV and CFD. *Chemical Engineering Science*, 62(21):5963–5978, 2007.
- [51] M. Alletto and M. Breuer. One-Way, Two-Way and Four-Way Coupled LES Predictions of a Particle-Laden Turbulent Flow at High Mass Loading Downstream of a Confined Bluff Body. *International Journal of Multiphase Flow*, 45:70–90, 2012.
- [52] B.R. Munson, D.F. Young, and T.H. Okiishi. *Fundamentals of Fluid Mechanics*. New York: John Wiley & Sons, Inc., 4th edition, 2002. p. 840. ISBN 0-471-44250-X.
- [53] J. Bredberg. On the Wall Boundary Condition for Turbulence Models. Technical report, Gothenburg: Chalmers University of Technology, 2000. p. 21.
- [54] S. Elghobashi. On Predicting Particle-Laden Turbulent Flows. *Applied Scientific Research*, 52(4):309–329, 1994.
- [55] B. Mols and R.V.A. Oliemans. A Turbulent Diffusion Model for Particle Dispersion and Deposition in Horizontal Tube Flow. *International Journal of Multiphase Flow*, 24(1):55–75, 1998.
- [56] D. Kaftori, G. Hetsroni, and S. Banerjee. The Effect of Particles on Wall Turbulence. *International Journal of Multiphase Flow*, 24(3):359–386, 1998.
- [57] ANSYS, Inc. *ANSYS FLUENT User's Guide*, 2012. Release 14.5. p. 2546.
- [58] A. Prosperetti and G. Tryggvason. *Computational Methods for Multiphase Flow*. Cambridge: Cambridge University Press, 2007. p. 470. ISBN 978-0-521-84764-3.

- [59] M. Mandø, M.F. Lightstone, L. Rosendahl, C. Yin, and H. Sørensen. Turbulence Modulation in Dilute Particle-Laden Flow. *International Journal of Heat and Fluid Flow*, 30(2):331–338, 2009.
- [60] C.T. Crowe. On Models for Turbulence Modulation in Fluid-Particle Flows. *International Journal of Multiphase Flow*, 26(5):719–727, 2000.
- [61] S. Lain and M. Sommerfeld. Turbulence Modulation in Dispersed Two-Phase Flow Laden with Solids from a Lagrangian Perspective. *International Journal of Heat and Fluid Flow*, 24(4):616–625, 2003.
- [62] A.A. Troshko and Y.A. Hassan. A Two-Equation Turbulence Model of Turbulent Bubbly Flows. *International Journal of Multiphase Flow*, 27(11):1965–2000, 2001.
- [63] Y. Sato, M. Sadatomi, and K. Sekoguchi. Momentum and Heat Transfer in Two-Phase Bubble Flow - I. Theory. *International Journal of Multiphase Flow*, 7(2):167–177, 1981.
- [64] O. Simonin and P.L. Violette. Predictions of an Oxygen Droplet Pulverization in a Compressible Subsonic Coflowing Hydrogen Flow. In *Numerical Methods for Multiphase Flows*, pages 65 – 82, 1990. Spring Meeting of the Fluids Engineering Division. Toronto, Canada, June 4 -7, 1990.
- [65] A.D. Burns, T. Frank, I. Hamill, and J.-M. Shi. The Favre Averaged Drag Model for Turbulent Dispersion in Eulerian Multi-Phase Flows. 2004. 5th International Conference on Multiphase Flow, ICMF'04. Paper No. 392. Yokohama, Japan, May 30 - June 4, 2004.
- [66] D. Lucas, E. Krepper, and H.-M. Prasser. Use of Models for Lift, Wall and Turbulent Dispersion Forces Acting on Bubbles for Poly-Disperse Flows. *Chemical Engineering Science*, 62(15):4146–4157, 2007.
- [67] P. Zhang, R.M. Roberts, and A. Benard. Computational Guidelines and an Empirical Model for Particle Deposition in Curved Pipes Using an Eulerian-Lagrangian Approach. *Journal of Aerosol Science*, 53:1–20, 2012.

- [68] Z.A. Majid, R. Mohsin, and M.Z. Yusof. Experimental and Computational Failure Analysis of Natural Gas Pipe. *Engineering Failure Analysis*, 19:32–42, 2012.
- [69] A. Tam, D. Ait-Ali-Yahia, M.P. Robichaud, M. Moore, V. Kozel, and W.G. Habashi. Anisotropic Mesh Adaptation for 3D Flows on Structured and Unstructured Grids. *Computer Methods in Applied Mechanics and Engineering*, 189(4):1205–1230, 2000.
- [70] J. Chawner. Accuracy, Convergence and Mesh Quality, 2012. The Connector. [e-journal]. Issue May/June. [retrieved August 29, 2013]. Pointwise’s customer journal. From: www.pointwise.com/theconnector/May-2012/Mesh-Quality.shtml.
- [71] C.J. Freitas. The Issue of Numerical Uncertainty. *Applied Mathematical Modelling*, 26(2):237–248, 2002.
- [72] P.J. Roache. Quantification of Uncertainty in Computational Fluid Dynamics. *Annual Review of Fluid Mechanics*, 29(1):123–160, 1997.
- [73] I.B. Celik, U. Ghia, P.J. Roache, C.J. Freitas, H. Coleman, and P.E. Raad. Procedure for Estimation and Reporting of Uncertainty Due to Discretization in CFD Applications. *Journal of Fluids Engineering*, 130(7):078001–078001–4, 2008.
- [74] B.B. Wilhelmsen. Numerical Modelling of Separation Efficiency of Sediment in a Combined Sewer Overflow (CSO). Master’s thesis, Trondheim: Norwegian University of Science and Technology, 2012. p. 58.
- [75] R. Field and T.P. O’Connor. Swirl Technology: Enhancement of Design, Evaluation, and Application. *Journal of Environmental Engineering*, 122(8):741–748, 1996.
- [76] Environmental Protection Agency of Ireland. *Wastewater Treatment Manuals: Preliminary Treatment*. Environmental Protection Agency, Ireland, 1995. p. 111. ISBN 1-899965-22-X.

- [77] Puhdistamoiden kuormitus ja puhdistustulos. In Finnish. [In Ymparisto.fi www-pages]. Updated: October 9, 2013. [retrieved October 22, 2013]. From: http://www.ymparisto.fi/fi-FI/Kartat_ja_tilastot/Jateveden_puhdistamojen_tilastot.
- [78] P. Rantanen, M. Valve, and L. Etelämäki. Jätevesien lämpötilat Suomessa. In Finnish. *Vesitalous*, XLIV(4):17–22, 2003.
- [79] C.G. Speziale, R.M.C. So, and B.A. Younis. On the Prediction of Turbulent Secondary Flows. Technical report, NASA Langley Research Center: Institute for Computer Applications in Science and Engineering, 1992. ICASE Report No. 92-57. p. 19.
- [80] H.G. Cuming. The Secondary Flow in Curved Pipes. Technical report, Aeronautical Research Council, 1955. Reports and Memoranda No. 2880. p. 17.
- [81] S. Dey. Secondary Boundary Layer and Wall Shear for Fully Developed Flow in Curved Pipes. *Proceedings of the Royal Society of London A.*, 458:283–298, 2002.
- [82] R.J. Belt, A.C.L.M. Daalman, and L.M. Portela. Experimental Study of Particle-Driven Secondary Flow in Turbulent Pipe Flows. *Journal of Fluid Mechanics*, 709:1–36, 2012.
- [83] T.M. Peters and D. Leith. Particle Deposition in Industrial Duct Bends. *Annals of Occupational Hygiene*, 48(5):483–490, 2004.
- [84] M. Breuer, H.T. Baytekin, and E.A. Matida. Prediction of Aerosol Deposition in 90° Bends Using LES and an Efficient Lagrangian Tracking Method. *Journal of Aerosol Science*, 37(11):1407–1428, 2006.
- [85] S. Jayanti, M.J. Mohideen, M.J. Wang, and F. Mayinger. Gas-Particle Flow Through Bends. In *Engineering Applications of Computational Fluid Dynamics*, number 5 in Proceedings IMechE 1993. London: Institution of Mechanical Engineers (IMechE), 1993. ISBN 0-85298-856-7.

- [86] A. Hossain, J. Naser, and M.A. Imteaz. CFD Investigation of Particle Deposition in a Horizontal Looped Turbulent Pipe Flow. *Environmental Modeling & Assessment*, 16(4):359–367, 2011.
- [87] J.E. Bardina, P.G. Huang, and T.J. Coakley. Turbulence Modeling Validation, Testing, and Development. Technical report, NASA Ames Research Center, 1997. Report No. A-376276. p. 98.
- [88] ANSYS, Inc. *ANSYS Release Notes*, 2013. Release 15.0. p. 168.

Appendix I

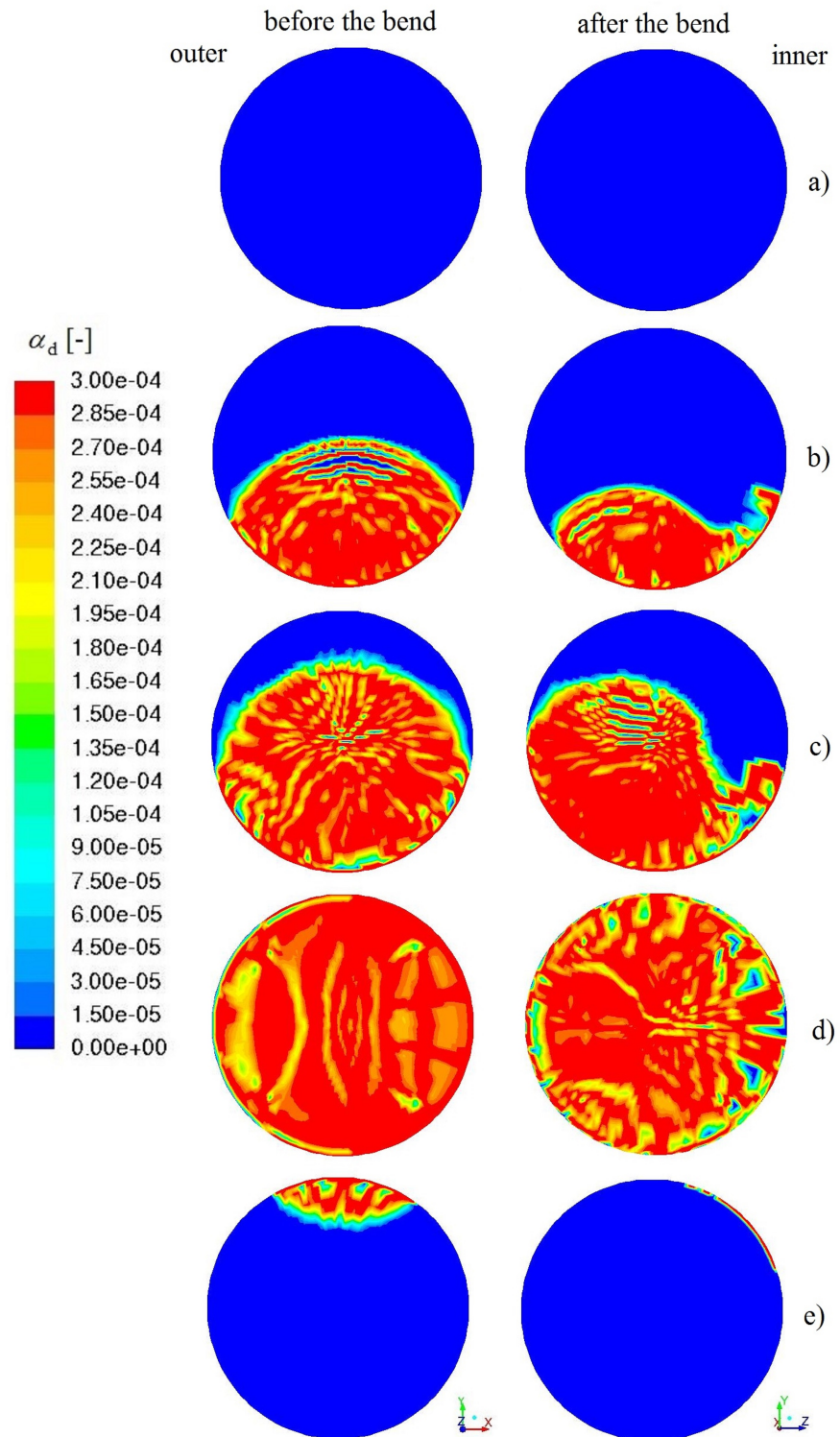


Figure 49. The contours of volume fraction in the by-pass pipe. a) 1075 kg/m³ b) 1017 kg/m³ c) 1005 kg/m³ d) 999.7 kg/m³ e) 950 kg/m³